Chapter 3

Optimization of Levitation System in RT-1

3.1 Levitation System in RT-1

Levitation technique is very important for dipole plasma confinement, because the particle loss to the parallel direction to the magnetic field often degrades the plasma confinement. To achieve a levitated dipole plasma, we must stably levitate the superconducting magnet for enough long time. Not only ensuring the stability of the F-coil, we must suppress a feedback noise or an accuracy of the coil position. The feedback noise is resulted from the voltage of the L-coil and influences the magnetic measurement such as a flux loop measurement. The noise can be decreased by setting the feedback gain lower, but on the other the stability of the system and the position accuracy of the F-coil degrades. We therefore meet the various requirement of the plasma experiment. For example, one day we need to decrease the feedback noise in relatively low or zero beta plasma experiment and the other day we need to levitate the F-coil with sufficient high feedback gains in high beta plasma experiment.

In this section the levitation study in the RT-1 levitation system is mentioned, including the analyses of the feedback system, optimization method and cancellation of the error field, etc.

3.1.1 Feedback Control of the Vertical Position of the F-Coil

Theoretical Model of Levitation

Several plasma devices with the same concept, which levitate the current ring in a vacuum chamber, have been constructed and the stability of the ring motion has been considered in the past. The motion of the floating magnet has generally six degrees of freedom consisting of position (x, y, z), tilt (θ_x, θ_y) and rotation θ_z. Stabilities of these motions depend on a levitation method. When a ring magnet is hung by a lifting coil located above the chamber, which we call the attaractive method, the motion of the ring is usually unstable to the vertical direction. And the stability of the tilting motion depends on the arrangement of the coils. Because the tilting motion is stable in the RT-1 configuration, only the vertical motion is considered from here.

Here we formulate the dynamics of the levitation system. The F-coil and the L-coil are facing coaxially; the model is shown in Fig. 3.1. The L-coil is fixed and produces a levitation field to the F-coil. We denote the current in the L-coil by I_L. The F-coil is levitated against gravity force by the magnetic force produced by the L-coil. We denote the mass, the current, the self inductance and the total number of turns of the F-coil by m, I_F, L_F and N_F, respectively. Because I_F changes in response to I_L in order to conserve the magnetic flux inside of the super-conductor, we denote the value of I_F when $I_L = 0$ by I_{F0}.

The vertical motion of the F-coil is governed by

$$m\frac{d^2z}{dt^2} = 2\pi R N_F I_F B_r - mg. \tag{3.1}$$

Here we introduce a coefficient k which divides the radial magnetic field B_r and the L-coil current I_L as $B_r = k \cdot I_L$. The coefficient k is determined by the geometry of two coils and is a function of z in this model. Then the force balance equation is given by

$$2\pi R N_F k I_F I_L - mg = 0. \tag{3.2}$$

The flux conservation law of the superconductor of the F-coil is given by

$$L_F I_{F0} = L_F I_F + M I_L, \tag{3.3}$$

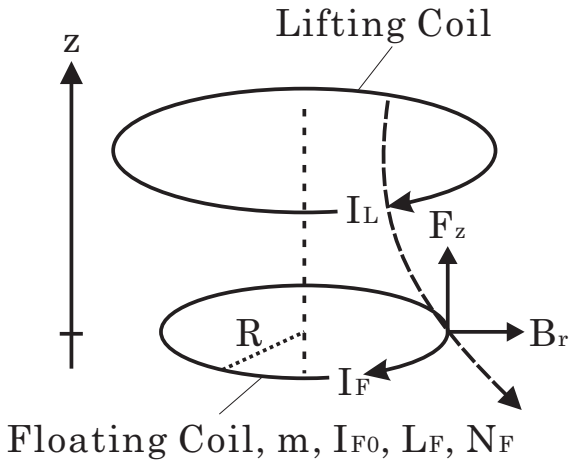

Figure 3.1: Levitation model.

where M is the mutual inductance between two coils. Combining (3.2) and (3.3), we obtain

$$I_F^2 - I_{F0} I_F + \frac{mgM}{2\pi R N_F k L_F} = 0.$$

This equation yields

$$I_F = \frac{I_{F0} \pm \sqrt{A}}{2} \qquad (A = I_{F0}^2 - \frac{2mgM}{\pi R N_F k L_F}). \tag{3.4}$$

Plugging (3.4) into (3.3), we find

$$I_L = \frac{L_F}{M} \frac{I_{F0} \mp \sqrt{A}}{2}. \tag{3.5}$$

If the determinant A is positive, two equilibrium solutions exist; the smaller one is unstable, while the larger one is stable. The unstable smaller-current equilibrium is chosen in the practical RT-1 levitation (to be explained later).

Next we calculate the growth rate α of the vertical motion. The magnetic force (the first term on the right-hand side of (3.1)) read as

$$\begin{aligned} F_z &= 2\pi R N_F I_F B_r \\ &= 2\pi R N_F (I_{F0} - \tfrac{M}{L_F} I_L) k I_L. \end{aligned} \tag{3.6}$$

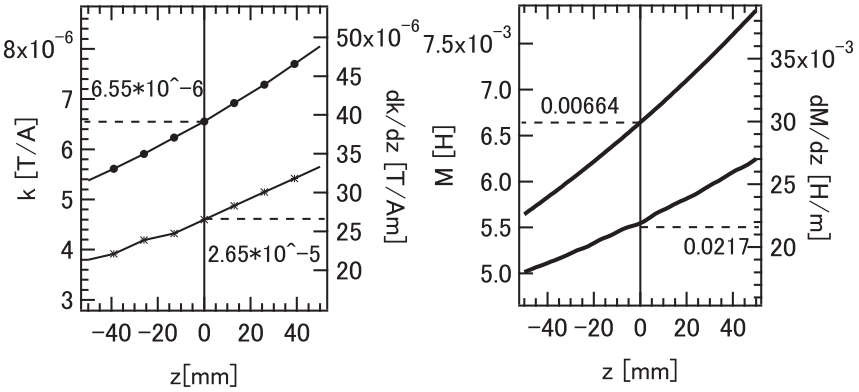

Figure 3.2: Calculated k, $\frac{dk}{dz}$, M and $\frac{dM}{dz}$ as a function of z in the RT-1 configuration.

The growth rate of the coil motion is given by

$$\begin{aligned} \alpha = \frac{dF_z}{dz}/F_z &= \frac{d(k(I_{F0} - \frac{M}{L_F}I_L))}{dz}/(k(I_{F0} - \frac{M}{L_F}I_L)) \\ &= \frac{dk}{dz}/k - \frac{dM}{dz}/(\frac{I_{F0}}{I_L}L_F - M). \end{aligned} \tag{3.7}$$

If the L-coil is located above the F-coil the first term on the right-hand side of (3.7) is positive, which is instability generally recognized in the attractive levitation. The second term represents the effect of flux conservation of superconductor, which tends to stabilize the motion. Thus the stability of the F-coil motion depends on the balance of two terms.

Parameters

Now we calculate the L-coil current I_L and the growth rate α by using the actual parameters of RT-1 (see Table 2.1 and Fig. 2.8). The parameters $k, dk/dz, M$ and dM/dz are given in Fig. 3.2.

We can calculate I_F and I_L by (3.4) and (3.5). Figure 3.3 shows I_F and I_L as functions of the levitation level z. Here we used two values of the F-coil current, $I_{F0} = 115.5$ A as the initial value of the excited current and 114.5 A as a decayed current after 5 hours. As shown in (3.4) and (3.5), there are two solutions of the equilibrium currents. The results shown in Fig. 3.3(a) and (c) are calculated by choosing the upper signs of double-sign in (3.4) and (3.5), and the results shown in

Fig. 3.3(b) and (c) by the lower signs. In Fig. 3.3(a) I_F and I_L are 114.63 A and 431.1 A respectively and these results are not so different from $I_L = 427.9$ A and $I_F = 115.5$ A, which are the calculation results of the case if we ignore the effect of the flux conservation. In Fig. 3.3(b) I_F and I_L are 0.867 A and 57.0 kA respectively and you can find these results are very different from the others. In Fig. 3.3(b) almost all of the current of I_F is decreased by the enormous flux produced by the L-coil current and, of course, an extremely high lifting-coil current is needed and this type of levitation is not possible in RT-1. In Fig. 3.3(c) and (d), the same calculation results of the case when the I_{F0} is decayed are shown to consider at the end of the experiment.

Next the growth rate α of the vertical motion of the F-coil is derived from (3.7). Here we used I_F and I_L calculated in Fig. 3.3 (a), (b), (c) and (d) and then α also has two solutions for each I_{F0}. The calculation results of α are shown in Fig. 3.4. Figure 3.4(a) corresponds to Fig. 3.3(a). Figures 3.4(b), (c) and (d) also correspond to Fig. 3.3 (b), (c) and (d). In the levitation in which I_F is not much affected by the flux of I_L ((a) and (c) cases), the motion of the F-coil is spontaneously unstable to the vertical direction and we need to control it in some way.

On the other hand, in the levitation in which I_F is markedly affected ((b) and (d) cases), the motion of the F-coil becomes very stable, in other words it's fixed without any control. As mentioned above, this type of levitation is impossible in the RT-1 device but this no-control levitation was actually observed in the levitation mock-up device FB-RT.

Feedback Control System

Because RT-1's F-coil is naturally unstable to the vertical direction, we apply a negative-PID feedback control. The flowchart of the RT-1 feedback system is shown in Fig. 3.5. The system consists of the PID controller, the L-coil current, an eddy current of the chamber, the F-coil motion and position detectors of the F-coil. The detected position of the F-coil is feed-backed to the L-coil current by the PID controller and the F-coil feels the controlled field which is delayed by the eddy

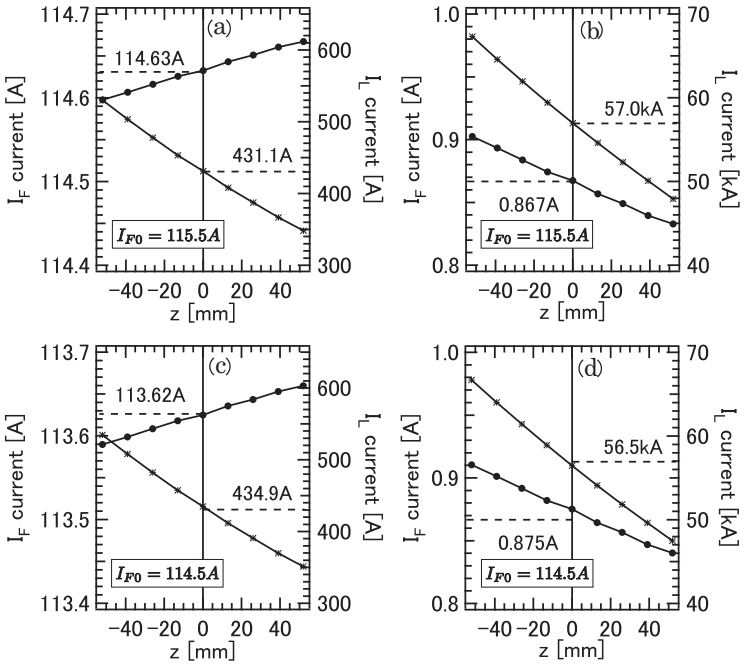

Figure 3.3: Calculation results of I_F and I_L as a function of z.

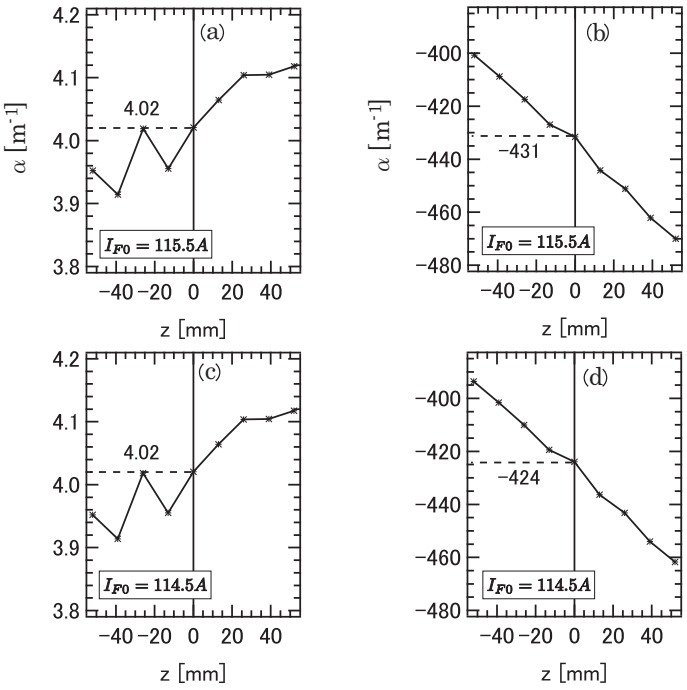

Figure 3.4: Calculation results of the growth rate α as a function of z. If α is positive, the motion of the coil is unstable.

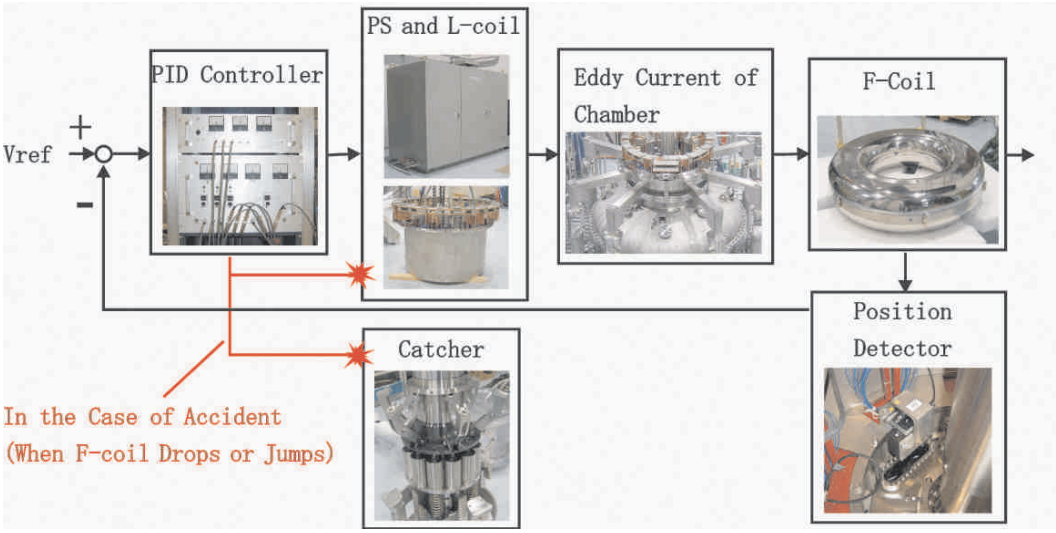

Figure 3.5: Flowchart of the RT-1 feedback system.

current. We evaluated each element of the system and a whole combined system by using a transfer function.

In the PID controller, 3 outputs of the position detectors are averaged and compared with a reference signal and then feedback-controlled with a PID analog circuit. All PID parameters, that is feedback gains, are controllable and adjusted by variable resistors. Gain of an integral parameter is usually kept much less than other gains in RT-1. Then the transfer function of the PID controller is expressed by

$$G_{PID} = P + Ds = P(1 + (D/P)s).$$

We succeeded to stabilize the system for all feedback gains which are thought to be stable enough. Stability boundary and optimization concept of the gains are mentioned at the last section.

Position Detector In RT-1, the position is detected by 3-cord laser sensors located on the top of the vacuum chamber at azimuthal intervals of 120 degrees, see Fig. 2.8. Because the F-coil may often tilt by an error field and mass imbalance during levitation, the z position of the F-coil is obtained by averaging over 3 outputs of the sensors. The sensors can detect the position with 0.05 mm/ 1 mV of accuracy

with enough frequency more than 1 kHz. Then the transfer function of the position detector, G_{PD}, is expressed by

$$G_{PD} = 20 \quad [\mathrm{V/m}].$$

The attitude of the F-coil is calculated by analyzing the vertical gaps among 3 points. RT-1's F-coil is tilted about 1.4 degrees by the geomagnetic field and we succeeded to reduce it down to 0.05 degrees by the correction coils, which is explained later.

Power Supply and the L-Coil Current Because the L-coil has finite resistance and inductance, 28 mΩ and 4.6 mH respectively, the response speed of the L-coil current was tested. A frequency response of the L-coil is obtained from 0.2 Hz to 100 Hz. The L-coil current can be approximated to a first order lag element whose cutoff is 25 Hz. The output current of the L-coil is 150 A for 1 V of an input voltage of the PID controller. Then the transfer function of the lifting current is expressed by

$$G_{I_L} = 150\frac{1}{1 + s/154} \quad [\mathrm{A/V}].$$

Eddy Current of the Chamber Because we put levitation field from the L-coil located at the outside of the chamber there is a possibility that an eddy current of the vacuum chamber become a difficult problem in the levitation. The growth time of the vertical motion is about 1 Hz ($\tau = 1/\sqrt{g\alpha}$). So the structure of the roof of the vacuum chamber has been designed to decrease the eddy current. Then we practically measured the frequency response of the eddy current of the chamber by using a Hall sensor in order to confirm that the delay time of the chamber is much faster than the growth time. The eddy current can be also approximated to a first order lag element, whose cutoff is 15 Hz, by

$$G_{EC} = \frac{1}{1 + s/93.4}.$$

The frequency responses of the delays of the L-coil current and vacuum chamber which were tested actually are shown in Fig. 3.6.

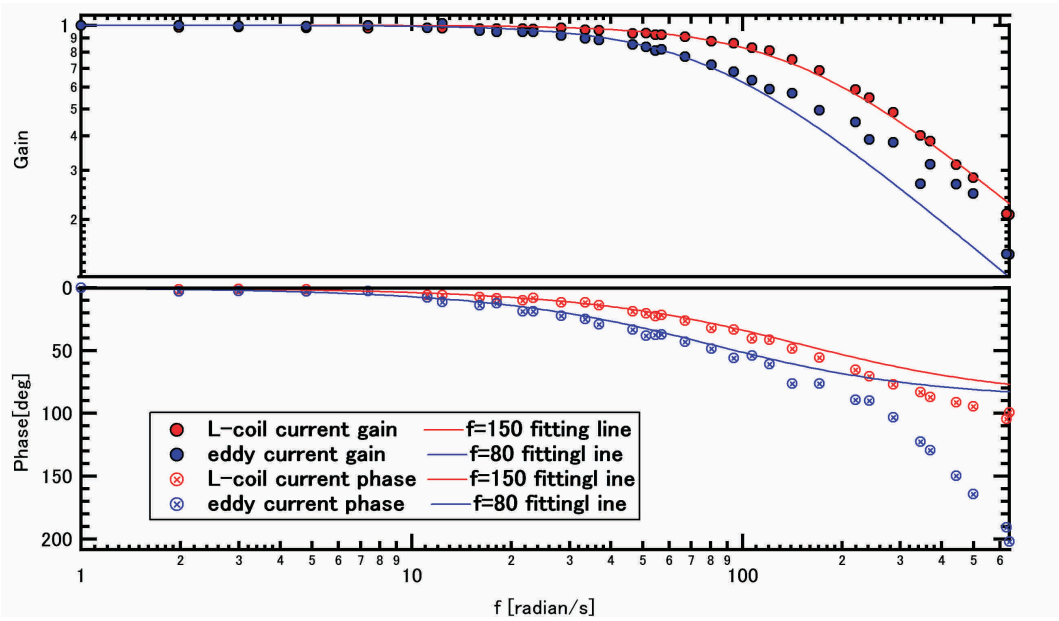

Figure 3.6: Frequency responses of the L-coil current and the effect of the eddy current on the chamber.

Motion of the F-Coil Transfer function of the motion of the F-coil is calculated from a motion equation of the F-coil, eq. (3.1). Here we assume that the F-coil current I_F is a constant and the L-coil current I_L and the coefficient k are linearized, $I_L = I_{L0}(1+y)$ and $k = k_0(1+\alpha z)$. We also assume that an initial magnetic force is equal to a gravity force of the coil, $2\pi R I_F k_0 I_{L0} - mg = 0$. Then a motion equation of the F-coil becomes

$$\begin{aligned} m\frac{d^2z}{dt^2} &= mg(y + \alpha z + \alpha yz) \\ &\quad mg(y + \alpha z). \end{aligned} \tag{3.8}$$

Equation (3.8) is Laplace-transformed and the transfer function of the coil motion becomes

$$\begin{aligned} s^2 Z(s) &= g(Y(s) + \alpha Z(s)) \\ G_{FC} &\equiv \frac{Z(s)}{Y(s)} = \frac{1}{I_{L0}} \frac{1}{g^{-1}s^2 - \alpha} \quad [\mathrm{m/A}] \\ &= \frac{1}{1733} \frac{1}{s^2/39.4 - 1} \quad [\mathrm{m/A}], \end{aligned} \tag{3.9}$$

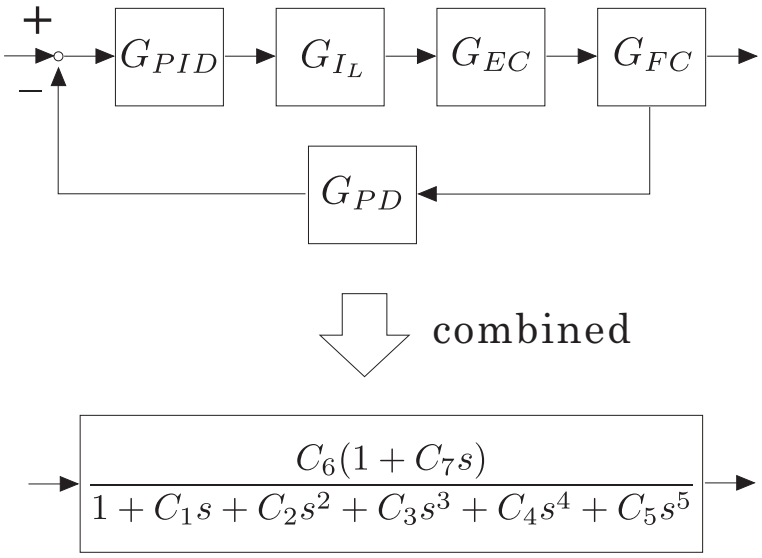

Figure 3.7: Block diagram of the RT-1 feedback loop and a transfer function as a whole.

where we substituted 431.1 A and 4.02 for I_{L0} and α, respectively, which are shown in Fig. 3.3 and Fig. 3.4. Clearly, the equation (3.9) has a positive pole and the coil motion itself is certainly unstable in the RT-1 configuration.

The transfer function of the feedback system An each element of the RT-1 feedback system is evaluated in the previous subsection, in this subsection we combine those elements as a whole. Block diagram of the system is shown in the top of Fig. 3.7. And a combined transfer function is expressed in a form using coefficients C_n $(n = 1, 2, \cdots, 7)$ as shown in the bottom of Fig. 3.7. In the RT-1 system the coefficients in the form are $C_n = (0.0685, 0.00315, 6.86 * 10^{-5}, 4.62 * 10^{-7}, 9.77 * 10^{-10}, 0.0563, 0.0633)$ where P = 5.0 and D = 0.3 are chosen. Then the poles of the system are $s = -207 \pm 37.8i, -39.8, -9.90 \pm 22.0i$. Real parts of all poles are negative and the F-coil motion is surely stabilized by PID negative feedback control.

3.2 Experimental Result

3.2.1 Ordinary Levitation Operation and the Steady-State Characteristics

Typical levitation signals of the RT-1 levitation experiment are shown in Fig. 3.8, the left axis is the z position of the F-coil and the right axis is the levitation current I_L. Figure 3.8 shows that the F-coil is stably levitated about more than 5 hrs. The F-coil usually periodically swings from side to side like a pendulum, which is resulted from a coupled effect of the nonuniformity of the F-coil's mass distribution and the error field. At the first 5 minutes of the levitation operation we suppress the rotation motion to a certain extent. After that we proceed to remove tha mechanical lifter off from the center of the chamber, in other words we proceed to the full levitation. In the full levitation the period of the pendulum-like motion is about 20 minutes and its rotation angle is about 30 degrees, which differ slightly from day to day. Figure 3.8 teaches us that the position signal and the current are fluctuating with noises resulted from the pendulum-like motion.

Because the F-coil is separated off from a power source, the current of the F-coil I_{F0} gradually decreases in time. We cannot measure directly I_{F0} during levitation but it is found that I_{F0} is about 114.5 A after the experiment. The L-coil current I_L gradually increases and the position of the coil z also decreases a little as the floating current I_{F0} decreases in Fig. 3.8. The L-coil current I_L is 432.4 A and its accuracy is ± 0.2 A at the first 1000 seconds. And then I_L increases to 435.5 A with ± 0.2 A of accuracy at the last 1000 seconds. Differences between these experimental results and calculated results shown in Fig. 3.3 are within 0.3 percent. We consider that the calculation results and the actual experimental results agreed fairly well because the difference between them is less than the accuracy of mass measurement of the F-coil, 1 percent. The position of the F-coil is -0.081 mm with ± 0.036 mm of accuracy at the beginning and the position decreases to -0.130 mm with ± 0.036 mm of accuracy at the end. Then we can conclude that the F-coil position is controlled with a dynamical accuracy of 0.05 mm and an overall accuracy of 0.125 mm which

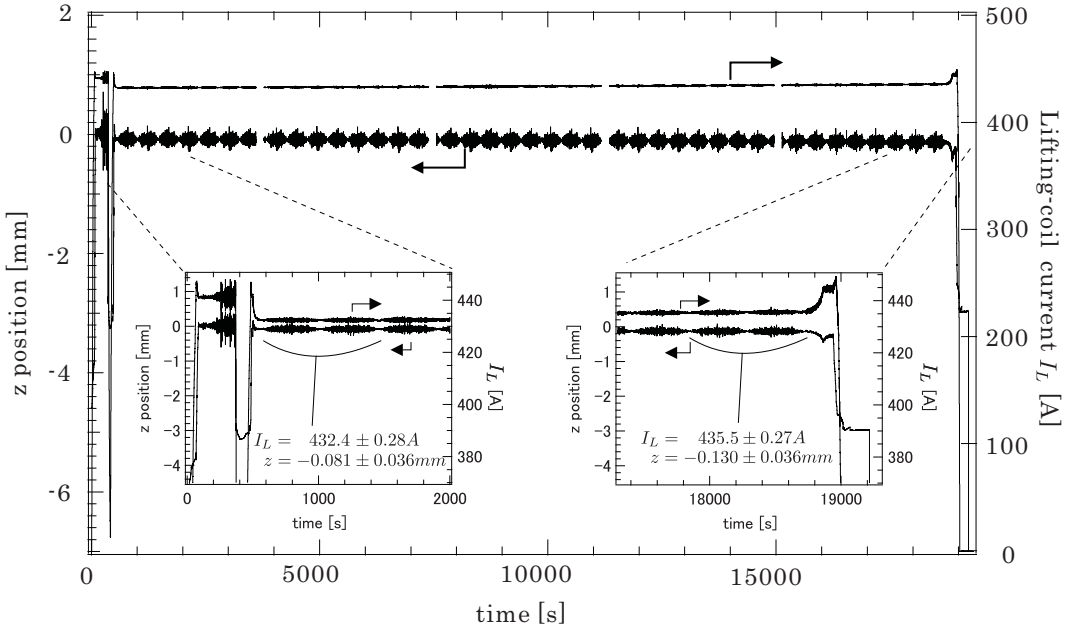

Figure 3.8: Typical levitation waveforms of the RT-1 levitation experiment. The F-coil is stably levitated about more than 5 hours and its position accuracy is within 0.125 mm. Four blackout regions mean the times to save the levitation waveforms. Feedback gains are (P,D) = (2.0, 0.2) in this levitation.

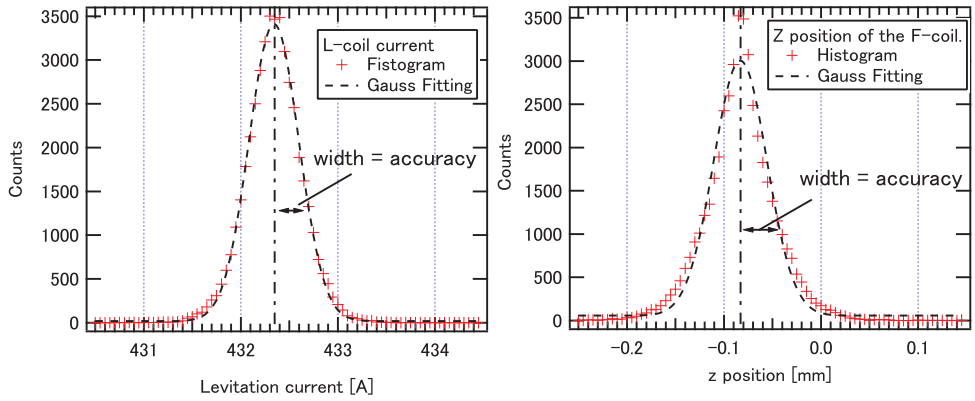

Figure 3.9: Example of the standard deviations of the signals. The histogram of the I_L is shown in left and one of the z position is shown in right.

are about twice as long as a resolution of the position detectors. These accuracies are evaluated by calculating the standard deviations of the signals. The histogram of the signals for first 1000 seconds is shown in Fig. 3.9.

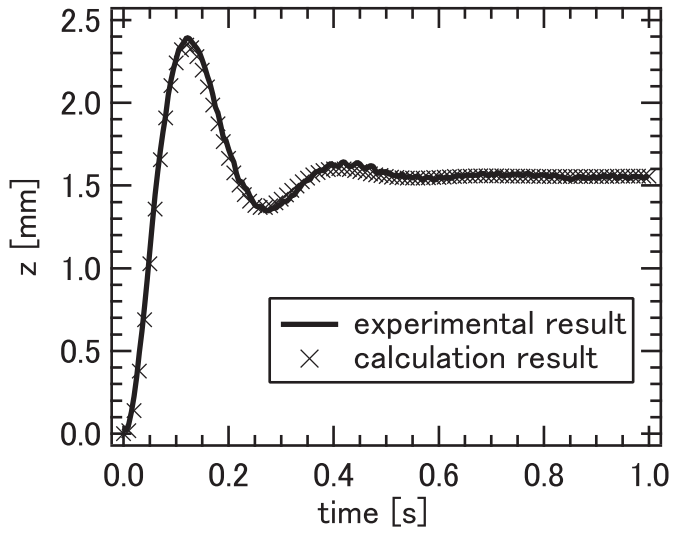

Figure 3.10: Step response of the RT-1 levitation system. Calculation result agrees fairly well with an actual experimental result.

3.2.2 Transient Response of the Levitation System

The step response experiment

To compare the theoretical model of the levitation system with the actual experiment, we tested a step response of the system. An experimental result of the step response is shown in Fig. 3.10. A solid line means an actual experimental signal and cross symbols represent the calculation results calculated from the transfer function obtained in the previous section. Differences between the actual experimental result and the calculation result are less than 0.05 mm in almost all period of time in Fig. 3.10.

Interaction between the levitation control and the high beta plasmas

We found an interesting interaction between the presence of high beta plasma and the levitation control. When we discharge a high beta plasma whose diamagnetic signal is considerably high the F-coil moves upward and the L-coil current unexpectedly decreases. A detailed mechanism of this phenomenon is not explained so far but the diamagnetic current is thought to play an important role by following

two reasons. If the PID feedback parameter is fixed, both a length of the position change and an amount of the decrease of the L-coil current are almost in proportion to a diamagnetic signal. And the amount of the decrease of the L-coil current is obviously larger than that estimated from a change of the F-coil position.

Typical waveform of the interaction is shown in Fig. 3.11. A plasma was discharged for a second from $t = 1.0$ s. Figure 3.11 shows the coil position signal in the upper window and the diamagnetic signal and the levitation current in the lower window. In Fig. 3.11, the diamagnetic signal of the plasma was about 2.7 mWb and the F-coil moved upward about 1 mm and I_L decreased about 20 A. (If the F-coil moves upward 1 mm, the L-coil current is expected to decrease only 1.75 A, see Fig. 3.3.) The rise time of the diamagnetic current is less than 50 ms. The broken line of the coil position signal means a calculation result which simulate the cases if the step signal whose rise time is 50 ms is added to the feedback system in Fig. 3.11. The calculation result also agrees well with the experimental result.

A rough estimate of the interaction is shown in Fig. 3.12. The plasma diamagnetic current I_p is roughly estimated by

$$\mathrm{I_{F-coil}} \cdot \mathrm{r}^2 : I_p \cdot R^2 \simeq 30\,\mathrm{mWb} : 2.7\,\mathrm{mWb}, \tag{3.10}$$

where $\mathrm{I_{F-coil}}$, r, R, 30 mWb and 2.7 mWb mean the F-coil current, the radius of $\mathrm{I_{F-coil}}$, the radius of I_p, the vacuum magnetic flux and the plasma magnetic flux. Then if we assume that the plasma current is distributed at R = 0.5 m, I_p is estimated about 6 kA. Because the levitation current decreased about 1.3 kA, the magnetic force between the F-coil and the L-coil decreased about 6 kgf. About 6 kA of the plasma diamagnetic current therefore partially hang up the F-coil about 6 kgf. In this rough estimate, decrease of the F-coil current resulted from the flux conservation is neglected because that is not effective from the equilibrium calculation which is mentioned later.

Optimization approach

The feedback noise is mainly resulted from fluctuations of a voltage of the L-coil. We want to suppress the noise because it mainly influences a magnetic measurement. It

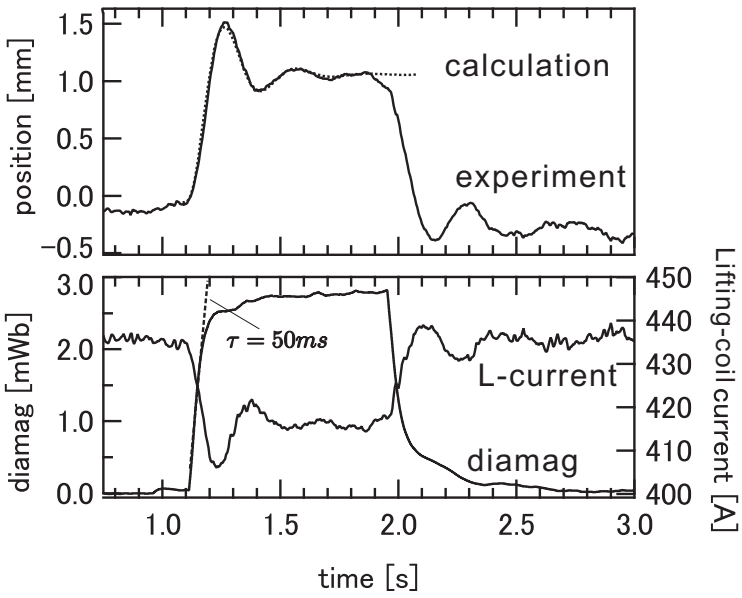

Figure 3.11: Response of the levitation system to a high beta plasma. The signal of the F-coil position is shown in the upper window and the signals of I_L and a diamagnetic current are shown in the lower window. A rise time of the diamagnetic signal is less than 50 ms in this discharge.

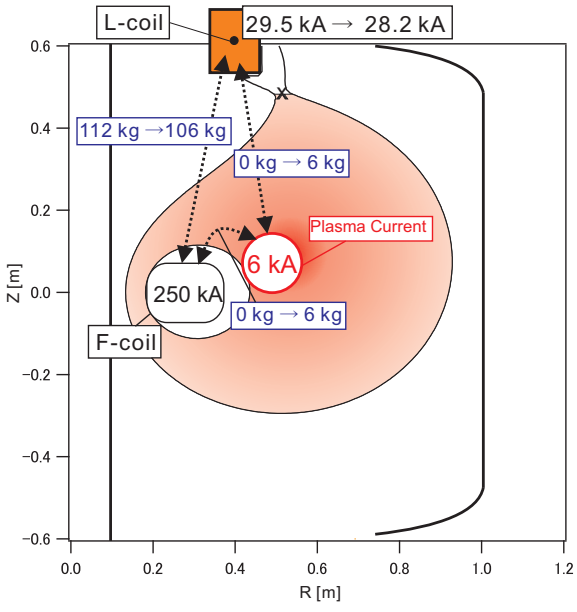

Figure 3.12: A rough model of the interaction between levitation and plasma diamagnetism in the case shown in Fig. 3.11.

is easy to decrease the noise by setting the feedback gains lower, but the accuracy of the position degrades. We measured the fluctuation levels of the levitation voltage and the F-coil position for the various feedback gains. Here the fluctuation of the levitation voltage corresponds to the feedback noise and the fluctuation of the position corresponds to the stability and the accuracy of the F-coil motion. The fluctuation levels are evaluated by calculating the standard deviations of the signals (shown in Fig. 3.9).

The results are shown in Fig. 3.13 and Fig. 3.14. A bottom axis and a left axis means P and D gains, respectively. A bold line divides a stable area and an unstable area which are theoretically estimated from the transfer function. The symbols in the stable area means pairs of P and D gains which we actually tested. We have made sure that the coil is stably levitated for all feedback gains which are estimated to be stable enough from the theoretical model. Figure 3.13 tells us that the fluctuation of the L-coil voltage clearly depends on D gain. The lower we set D gain, the lower the fluctuation level becomes. Figure 3.14 tells us that the fluctuation of the F-coil position, in other words the accuracy of the F-coil position, depends on both of the P and D gains. If we want to levitate the coil with sufficient accuracy we must set P and D gains sufficiently larger than the stability boundary.

Considering from these analyzes, we optimized the feedback gains to meet the requirement for the various plasma experiments. In low beta plasma experiments, the fluctuation noise of L-coil is a problem and there's no displacement effect resulted from the diamagnetic current. The feedback gains are adjusted to (P,D) = (2.0, 0.2) in low beta plasma experiments. D gain is set small to suppress the feedback noise and P gain is also optimized small to decrease a settling time of the system. In high beta plasma experiments, the feedback noise does not matter a lot because the feedback noise is small compared with the diamagnetic signal of high beta plasmas. On the other hand the displacement of the F-coil, such as Fig. 3.11 and Fig. 3.12, lifted by a high beta plasma becomes a problem instead. The larger the P gain is, the shorter the coil is displaced by the plasma diamagnetism. So P and D gains are adjusted to $(P,D) = (5.0, 0.25)$ in high beta plasma experiments.

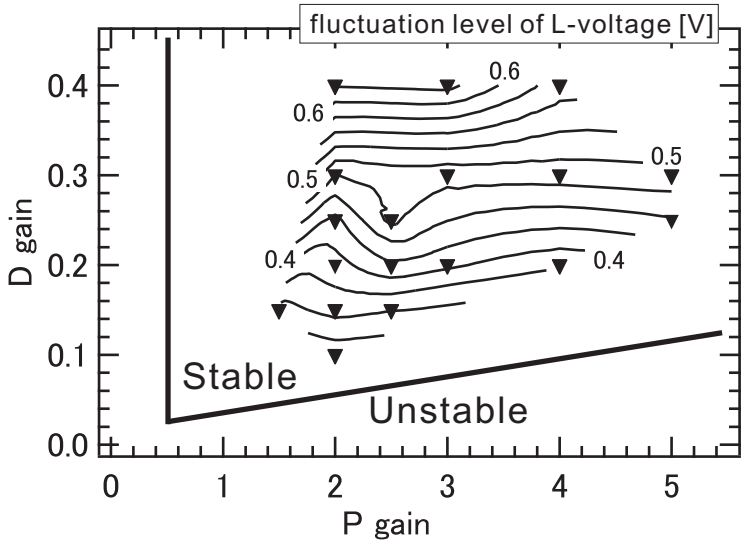

Figure 3.13: Contour map of the fluctuation noise of the levitation voltage for the various feedback gains. A bold line theoretically divides a safety area and an unstable area.

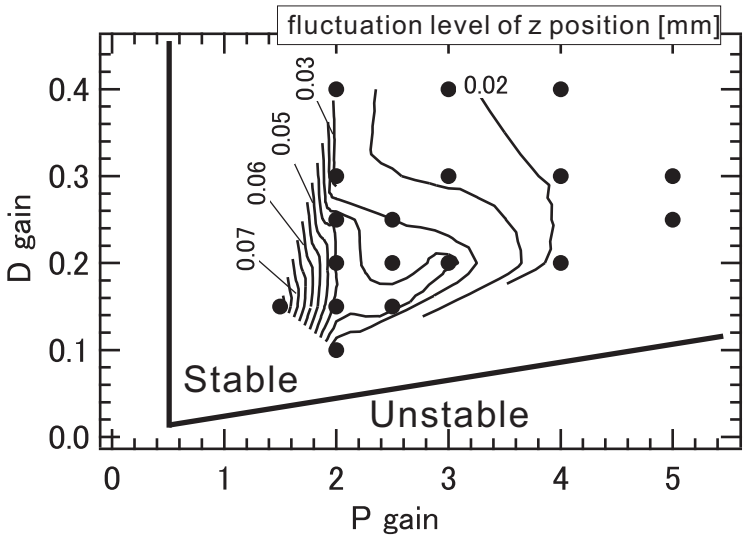

Figure 3.14: Contour map of the fluctuation levels of the F-coil position for the various feedback gains. The resolution of the position detectors is about 0.05mm.

Statistical relations between levitation and plasma in the interaction

In this paragraph, the statistical relations in the interaction which was previously mentioned are shown. Linear relations were found between the levitation signals and the plasma diamagnetism when we fixed the feedback gains. The relations between levitation and plasma diamagnetism are shown in Fig. 3.15, Fig. 3.16 and Fig. 3.17. In these figures the feedback gains were set to (P, Q) = (5.0, 0.25). In Fig. 3.15, the relation between displacement of the F-coil position, δ z, and plasma diamagnetic signal is shown. The fitting line is expressed by δ z = 447.62 diamag [mm/Wb]. In Fig. 3.16, the relation between decrease of the L-coil current, δ IL, and plasma diamagnetic signal is shown. The fitting line is expressed by δ IL = -7261.4 diamag [A/Wb]. In Fig. 3.17, the relation between displacement of the F-coil position and decrease of the L-coil current is shown. The fitting line is expressed by δ z = -0.06162 δ IL [mm/A]. These relations between levitation and diamagnetism are a clear evidence that the F-coil is hung up by the plasma diamagnetic current. The interaction is thought to be resulted from the vertically asymmetric configuration of the magnetic surfaces. The center of the plasma diamagnetic current is located above the midplane of the RT-1 device, see Fig. 3.12.

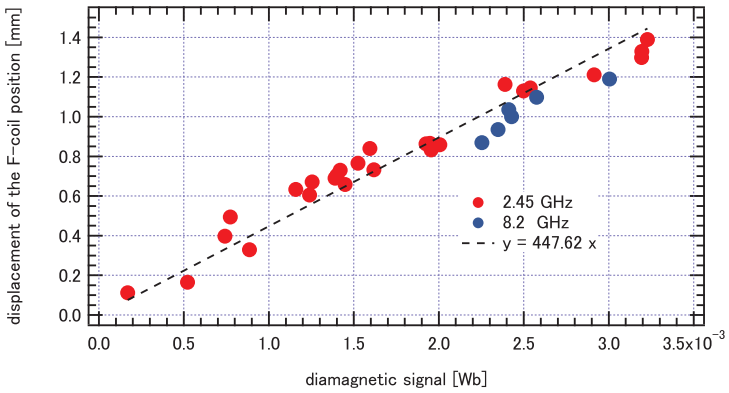

Figure 3.15: Displacement of the F-coil position as a function of diamagnetic current. Red markers show when we used 2.45 GHz ECH and blue markers show when we used 8.2 GHz.

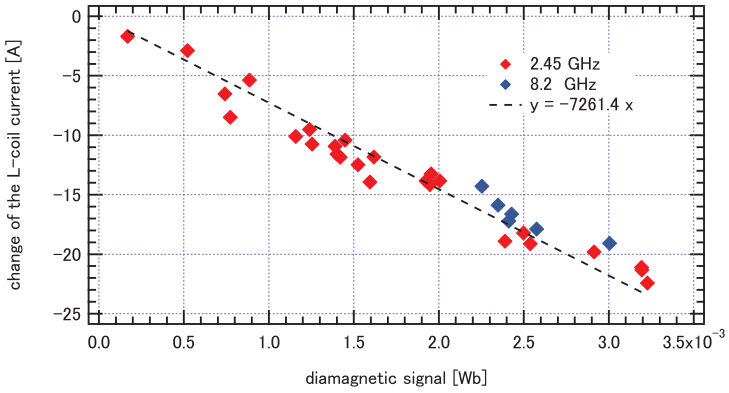

Figure 3.16: Decrease of the L-coil current as a function of diamagnetic current. Red markers show when we used 2.45 GHz ECH and blue markers show when we used 8.2 GHz.

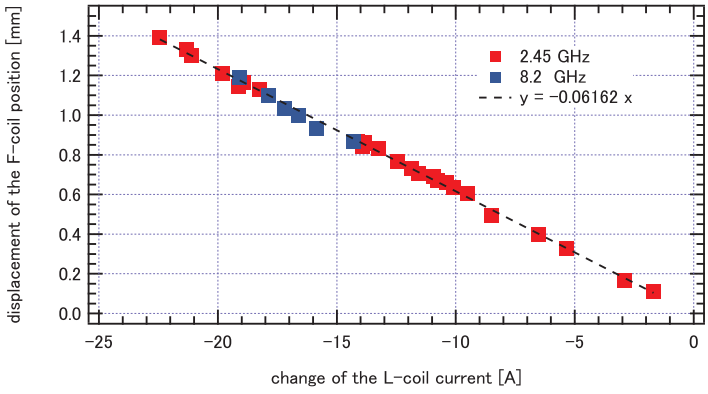

Figure 3.17: Displacement of the F-coil position as a function of decrease of the L-coil current. Red markers show when we used 2.45 GHz ECH and blue markers show when we used 8.2 GHz.

3.2.3 Improvement of the Field Accuracy

As mentioned above, the motion of the magnet has six degrees of freedom consisting of the position of the center of the mass (x, y, z), the attitude (θ_x, θ_y) and the rotation θ_z. The feedback control of the instability of vertical motion of the F-coil is focused in the previous section. Although the tilting motion is stable, small nonuniformity of the mass distribution of the ring magnet as well as the geomagnetic field yield a finite tilt and slow oscillations of the attitude. The tilt due to the mass imbalance is reduced to less than 0.05 degrees (from 0.88 degrees initially) by adjusting the mass distribution. The aim of this development is to minimize the attitude-angle of the floating magnet and improve the plasma confinement by canceling the geomagnetic field with a sufficiently small error field. The drawing of the simple model of what causes the tilting is shown in Fig. 3.18.

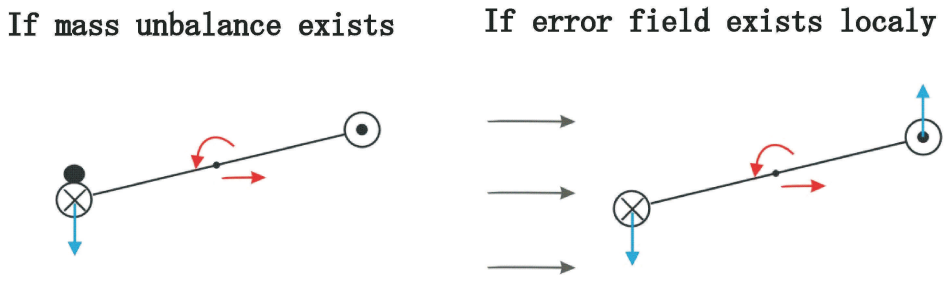

Figure 3.18: The drawing of the simple model of what causes the tilt. There're two main causes, horizontal error field and the mass imbalance.

The RT-1 experiment began the operation of the cancellation of the error field with smaller prototype correction coils that were installed near the chamber. Using these coils, we tested the attitude control and proved that the magnet can be made level when we apply a 0.3 Gauss of horizontal magnetic field, which just cancels the horizontal component of the geomagnetic field in Eastern Japan. The new and prototype correction coils are compared in Fig. 3.19 and Fig. 3.20. The correction coils are composed of two Helmholtz coils crossing at right angles. The prototype coils are located at r = 1.4 m from the center of the chamber (about 0.5 m from the edge of the plasma region) so the error field (multipole component produced by the correction coils) is considerably strong. The new system of correction coils

was designed to reduce the error field to less than 0.1 percent of the mean field at the edge region. Numerical estimates of the error fields of both correction coils are shown in Fig.3.22, where we assume a 0.3 Gauss of the geomagnetic field to the north; the correction coil current is set to make the average field at r = 0.25 m (radius of the F-coil current center) to cancel the geomagnetic field. The prototype coils produce a maximum error field of about 1.3 G, which is 2.6 percent of the ambient field at r = 1.0 m. In contrast, the new coils reduce the maximum error field to 0.05 G, which is 0.1 percent of the ambient field.

The new correction coils are designed and constructed by us for almost all processes. The photographs of the construction and the partials structures of the correction coils are shown in Fig. 3.21. The new correction coils are made of aluminum and the structure itself is designed to carry a electric current with a measurements of 4.5 m $\times$ 4.5 m $\times$ 4.0 m. In Fig. 3.21, partial structures of the downside (c) and the topside (d) corners are shown. The connecting lines to the power supply is connected at one of the downside corners. The topside corners are rigidly reinforced by the aluminum bars.

A typical experimental result for the attitude control is shown in Fig.3.23. The magnet rotates like a pendulum, because the heaviest point oscillates around the minimum potential of the error field (see Fig. 3.23). Without attitude control, three vertical positions (P1, P2, P3) of the magnet (measured by laser sensors) have appreciable differences, which correspond to about 1.4 degrees of tilt of the magnet. When we apply the correction field, the tilt is reduced to less than 0.05 degrees.

With the new correction coils, we have observed appreciable improvement of the plasma confinement. The diamagnetic signals have been increased more than 10% in comparison with the previous data with the old prototype correction coils. The improvement is more significant in operation with a lower RF power (see Fig.3.24). The diamagnetic signal is enhanced by a factor of 1.5 in plasma with 5kW RF power. This confinement improvement is not explained in detail but the improvement of the edge plasma confinement is thought to have a positive effect on the core plasma confinement as mentioned in section 2.3.1.

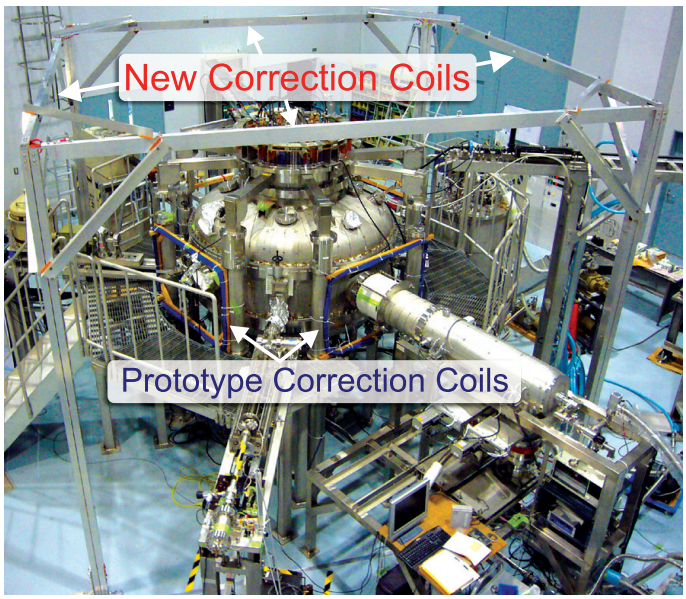

Figure 3.19: Photograph of the RT-1 device and the correction coils. The prototype coils have dimensions of 1.2 m ×0.8 m. The new correction coils are made of aluminum self-standing frames with a measurements of 4.5 m × 4.5 m × 4.0 m.

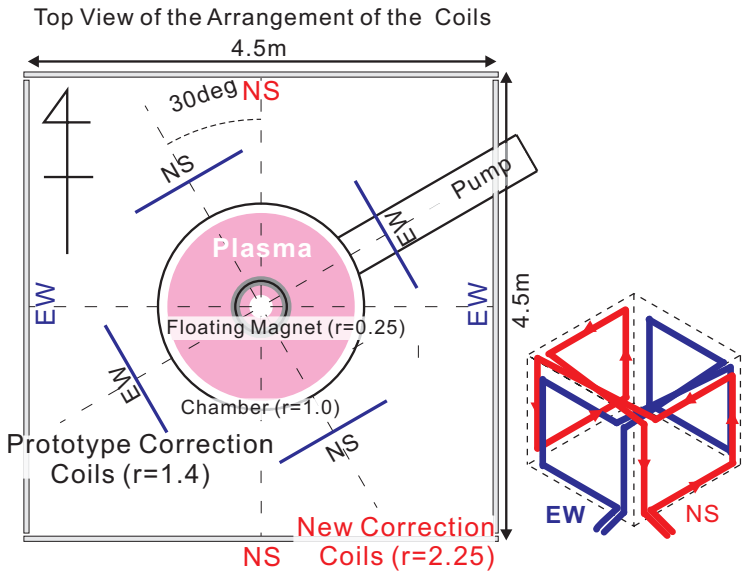

Figure 3.20: The arrangement of the RT-1 device and the correction coils. The prototype coils are not parallel to the geomagnetic field, while the new coils are set approximately parallel to the geomagnetic field. The EW coils are installed for the fine adjustment of the magnetic field.

Figure 3.21: Photographs of (a) (b) manufacturing the new correction coils and the partial structures of the downside (c) and the topside (d) corners of the new correction coils.

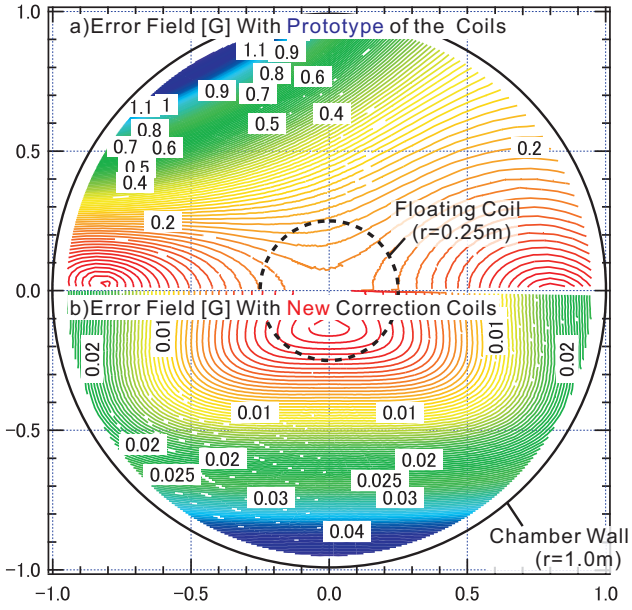

Figure 3.22: Calculation results of the strength of the error field caused by the multipole component of (a) the prototype (upper figure) and (b) the new correction coils (lower figure). The distribution of the field is shown on the mid-plane (z = 0). Field strength is given in gauss.

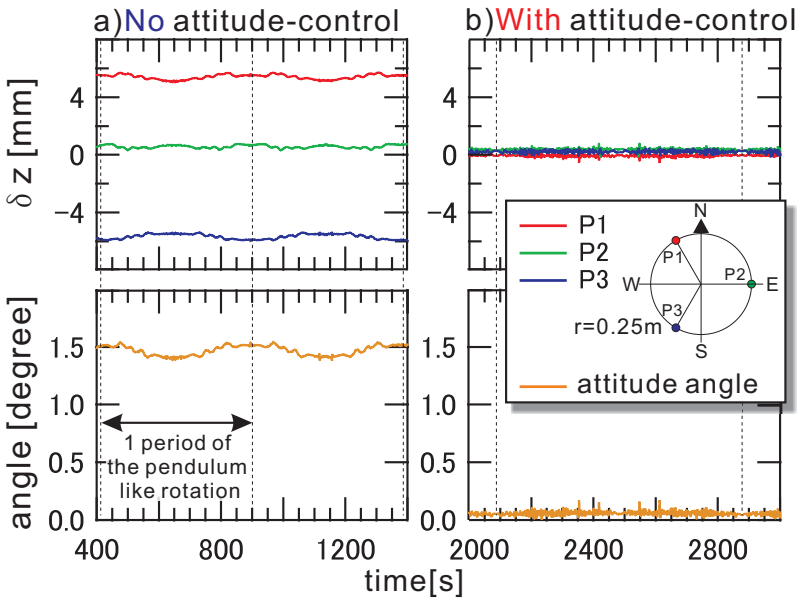

Figure 3.23: Demonstration of attitude control. The vertical position of the floating magnet is measured at three points (P1, P2, P3) on the upper surface of the coil casing (shown in upper figures). The tilt angle is estimated by the differences among these three positions (shown in lower figures). In these plots, the signals have been averaged over 30 seconds to reduce high-frequency fluctuations caused by micro-scratches on the magnet's surface. (a) Left: Without the correction field, the magnet is tilted about 1.4 degrees. (b) Right: With the optimum correction field, the tilt angle is decreased to 0.05 degrees.

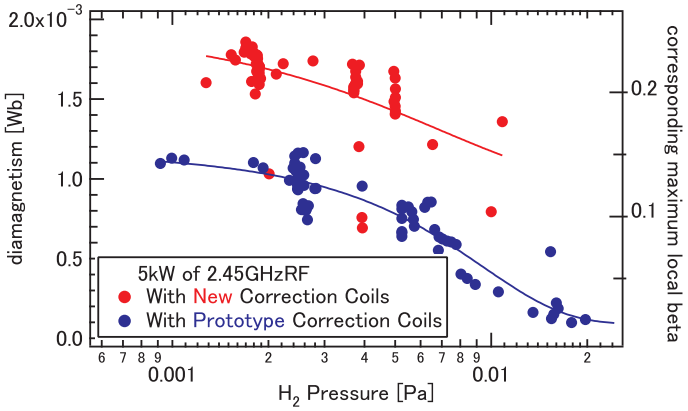

Figure 3.24: Comparison of the diamagnetic signals for plasmas with the prototype and new correction coils. The diamagnetic signal of 1 mWb corresponds to more than 0.13 of the local beta [4]. The diamagnetic signal in RT-1 depends mainly on the filling gas pressure and the heating power, and it has a large variation when we take the pressure on the horizontal axis. The lower diamagnetic signals with the new correction coils in this graph are measured at the beginning of the experiment, when outgassing from the chamber wall is thought to be large.

Chapter 4

Hot Electron Plasma in RT-1

4.1 Experimental Setup

4.1.1 Plasma Production

In the RT-1 device, plasmas are produced by Electron Cyclotron Heating (ECH) with two microwave sources. One is 2.45 GHz magnetron whose maximum power is 20 kW and its oscillation duration is 1 second in this research (up to 2 seconds). The other is 8.2 GHz klystron whose maximum power is 25 kW (up to 100 kW in future plan) and its duration is 1 second. The schematic illustration of the RT-1 chamber, magnetic field lines, electron cyclotron resonance layers, 2.45 GHz magnetron, and a waveguide. is shown in Fig. 4.1. This 2.45 GHz microwave system (Micro Denshi Co., Ltd. type MMG-2200V) was formerly used in the Proto-RT device and moved to Kashiwa in 2007. Microwave is transmitted via an waveguide with TE10 mode, including a directional coupler, an insulating waveguide tube, and a matching tube. It is injected into the chamber through a west port at z = 0 m with O-mode and microwave is adjusted by using an external circuit. Electron's gyro motion resonates with 2.45 GHz electric field when magnetic field strength is 875 gauss. The cutoff density of ordinary mode for 2.45 GHz injection is 7.4×10^{16} m^{-3}. In the case of 8.2 GHz frequency, electron's gyro motion resonates when magnetic field strength is 2929 gauss. The cutoff density of ordinary mode for 8.2 GHz injection is 7.4×10^{16} m^{-3}.

Hydrogen gas is used for a fueling neutral gas in usual ECH plasma experiment. In the experiment of ion temperature measurement by spectroscopy, helium gas is used instead. The plasma parameters for both of the fueling gas, hydrogen and helium, are almost the same. Typical pressure of filling gas is 10^{-4} - 5×10^{-2} Pa and n_n 2.5×10^{17} m^{-3} when $P_{H2} = 1 \times 10^{-3}$ Pa.

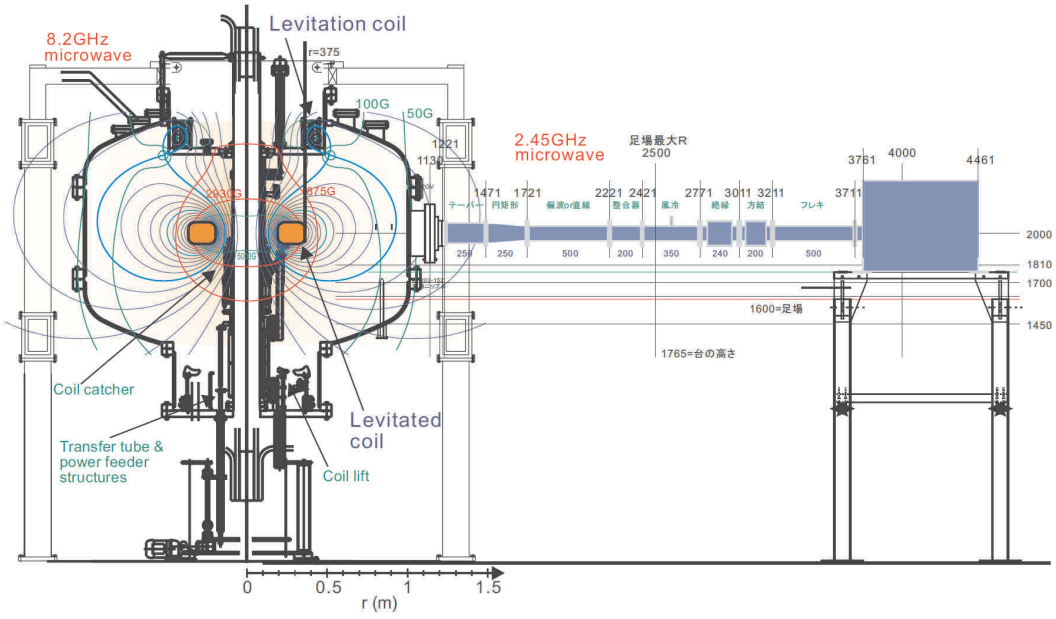

Figure 4.1: Schematic drawing of the cross section of the RT-1 device, 2.45 GHz magnetron, and waveguide.

4.1.2 Major Diagnostics

In this research the magnetic structure of plasma diamagnetism is focused. The most reliable magnetic measurement system is a flux loop system. The flux loop is a simple coil which senses the change of the magnetic flux which is surrounded by the loop. Because this measurement uses a law of electromagnetic induction, the vacuum field (which is produced by external coils, the F-coil and the L-coil) cannot be measured. Four magnetic loops are wound outside of the vacuum chamber at r = 1.01 m. Vertical position of the each loop is z = ± 0.20 m and z = ± 0.36 m,

respectively. The diamagnetic signal is recorded to a PC through an amplifier and Yokogawa WE7000 Data Acquisition System with other measurement signals. The signal is numerically integrated and the offset is corrected in order to estimate flux variations by a plasma, or the plasma diamagnetism.

As major diagnostics for observation of the plasma confinement, the one cord of interferometer is installed in RT-1. A 75 GHz (wave length $\lambda = 4$ mm) heterodyne interferometer is used to measure electron line integrated density n_l. Phase shift of 2 π rad gives $n_l = 5.57 \times 10^{17}$ m^{-2}. The transmitter and receiver of the interferometer were placed at the north and south tangential ports with quartz viewports, and the length between the each port is 1.78 m. When the plasma is distributed inside the separatrix of the vacuum magnetic field, path length of the 75 GHz microwave inside the plasma is 1.6 m.

Figure 4.2 is the top view of the RT-1 chamber and diagnostics. And the magnetic surfaces and the vertical position of the flux loops are shown in Fig. 4.3. Each flux loops are numbered beginning at the top as "loop1", "loop2", "loop3" and "loop4". The vertical position of loop1, loop2, loop3 and loop4 are z = 0.36 m, 0.20 m, -0.20 m and -0.36 m, respectively. The loops are wounded around the vacuum chamber , and their radial positions are r = 1.01 m. The averaged signal of loop1, loop2, loop3 and loop4 is taken as "a plasma diamagnetic signal".

4.2 Typical Discharges

In RT-1, main controllable parameters are ECH powers (2.45 GHz or/and 8.2 GHz) and the fueling neutral gas pressure. It is found that the plasma diamagnetic signals increases higher in a lower fueling gas pressure in special. The waveforms of the typical discharges are shown in Fig. 4.4. Five kilowatt of 2.45 GHz ECH power is the same for both discharges but filling gas pressure is very different. In a lower pressure discharges, the waveforms are stabilized and 1 mWb of diamagnetic signal is observed. The plasma densities of two discharges are almost the same, so it seems that the temperature of runaway electrons increased very much in lower gas pressure. To estimate the hot electron temperature, we developed the soft X-rays (SX)

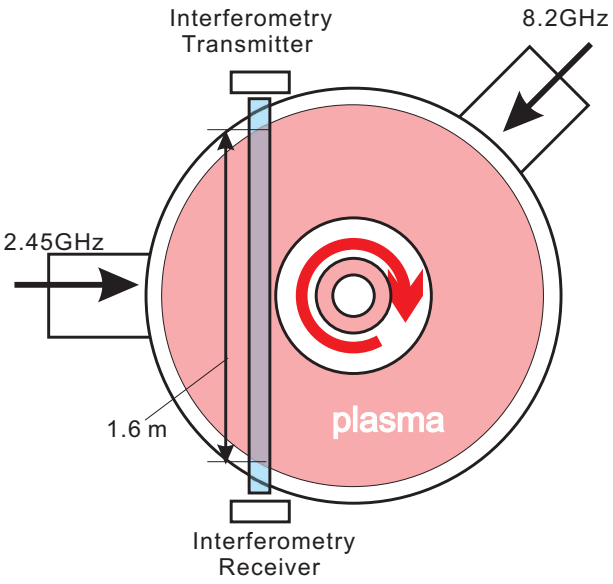

Figure 4.2: Top view of the microwaves and interferometry system. The waveguide of the 2.45 GHz microwave is seeing the F-coil from midplane and the waveguide of the 8.2 GHz microwave is seeing it obliquely from above.

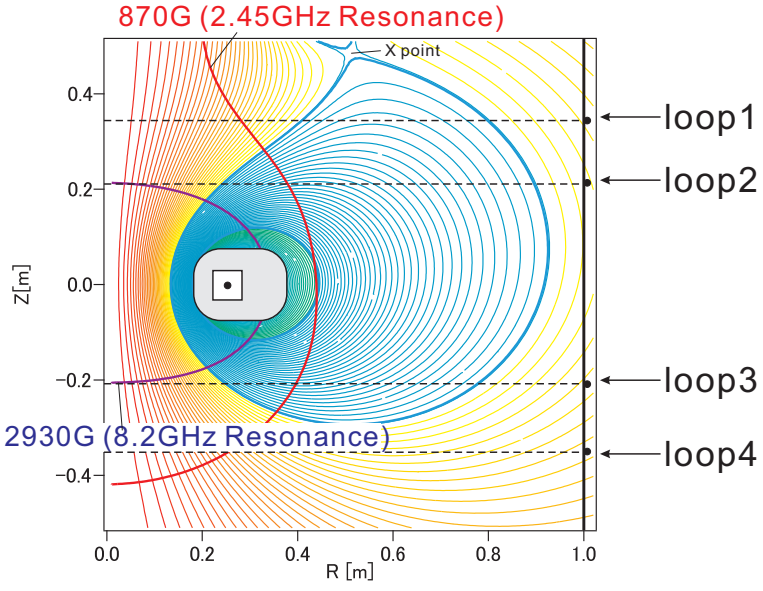

Figure 4.3: Drawing of the magnetic surfaces and the vertical position of the flux loops.

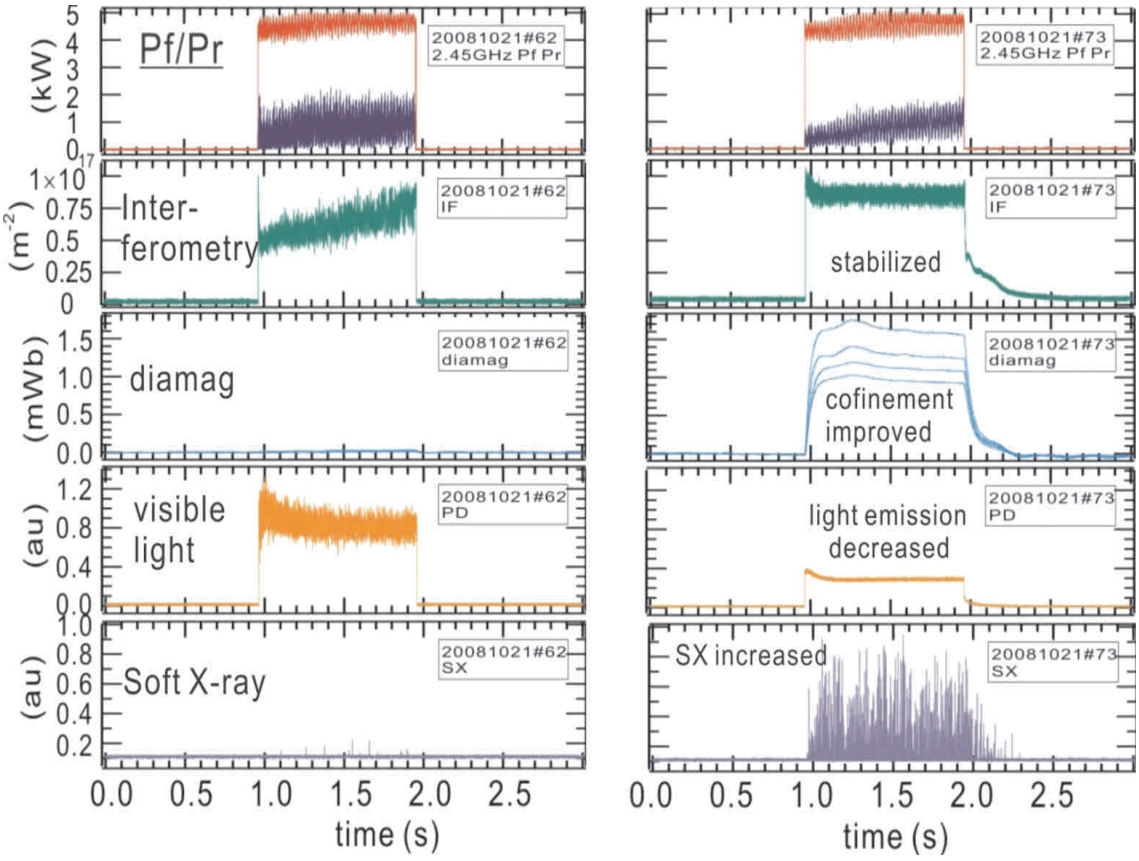

Figure 4.4: Waveforms of the typical discharges for different fueling gas pressure. (Left) P_{H2} = 45 mPa, (Right) P_{H2} = 1.3 mPa.

measurement system. The hot electron temperature can be measured by analysis of the SX spectrum and the density of the hot electrons are roughly estimated by counting the photon number. Typical SX measurement result is shown in Fig. 4.5.

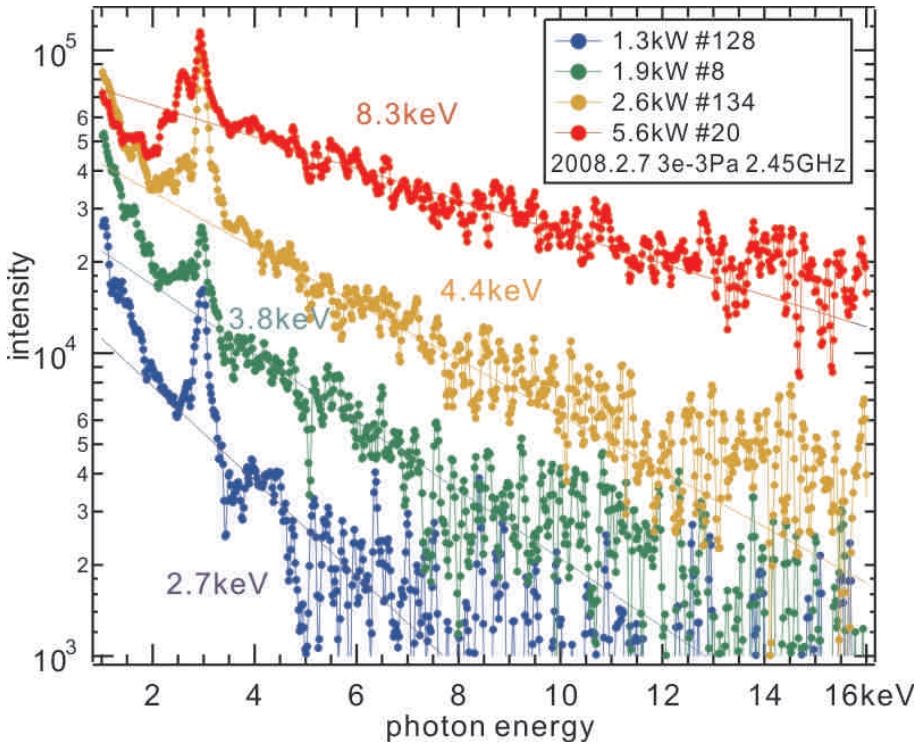

Figure 4.5: Typical soft X-rays spectrum observed in RT-1. The temperature of the hot electron is about 10 keV in high power discharges and the density of the hot electron is order of 10^{16} m^{-3}. These spectrum are measured by Saitoh [after Yoshida (2008) [61]].

4.3 Optimization of Plasma Diamagnetic Signal

To optimize the plasma diamagnetism, which is equal to achieve high beta plasma confinement, the dependence of diamagnetic signals and electron line density on the discharge conditions are tested. The results are shown in Fig. 4.6 and Fig. 4.7. In those experiments we changed the discharge conditions of 2.45 GHz ECH power and a fueling H_2 pressure. ECH power was changed between 500 W and 5 kW. H_2 pressure was changed between 2 mPa and 8 mPa. The plasma diamagnetic signal strongly depends on both conditions and the maximum diamagnetic signal which exceeded 1.6 mWb , was obtained with a 5 kW of ECH and a 2 mPa of H_2 pressure. Electron line density seems to depend on the ECH power and its about 1×10^{17} m^{-3} when the power was 5 kW.

Figure 4.8 and 4.9 show another dependencies of the diamagnetic signal. In Fig. 4.8, the gas pressure dependence is clearly shown. The ECH power dependence is shown in Fig. 4.9. Generally speaking, the plasma with 2.45 GHz ECH is likely to show the larger diamagnetism in comparison to the plasma with the same power of 8.2 GHz ECH.

From these experiments, the diamagnetic signal is likely to increase in lower fueling gas pressure and high ECH power condition. Then we tried to discharge with the optimized conditions to get the higher diamagnetic signal. We used the 15 kW of 2.45 GHz ECH in addition to 20 kW of 8.2 GHz ECH, almost maximum power of ECH was used. The fueling gas pressure was optimized to approximately 1 mPa, if we decrease the gas pressure lower than 1 mPa the plasma discharges often be unstable. The waveforms of the optimized plasma discharge is shown in Fig. 4.10. The vertical magnetic field measured at (R,Z)=(1.05 m, 0.0 m), the diamagnetic signals and the line integrated electron density are shown. The averaged diamagnetic signal was 3.4 mWb and at the same time the magnetic field near the plasma increased about 20% of the vacuum field, from 53 G up to 63 G. The line integrated electron density reached 1.3 $\times 10^{17}$ m^{-2}.

The highest diamagnetic signal was obtained with a 0.5 mPa of H_2 pressure and with highest ECH power. The ECH power of 2.45 GHz was 19.5 kW (20 kW

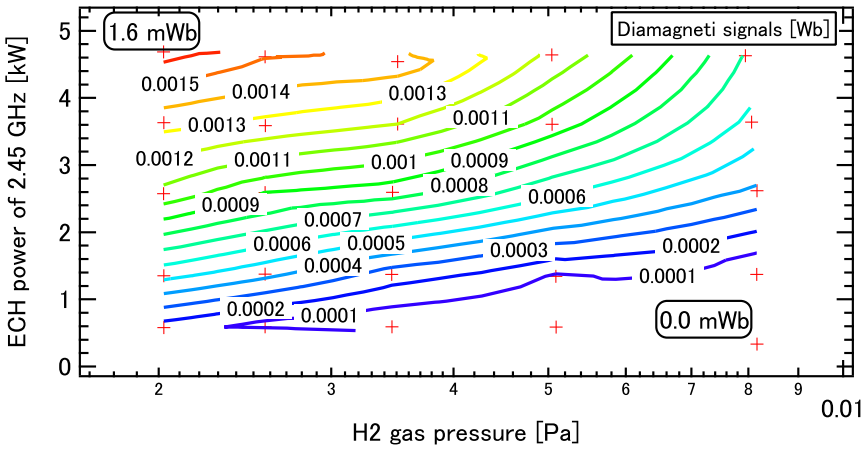

Figure 4.6: The contour map of the diamagnetic signals for various plasma discharges.

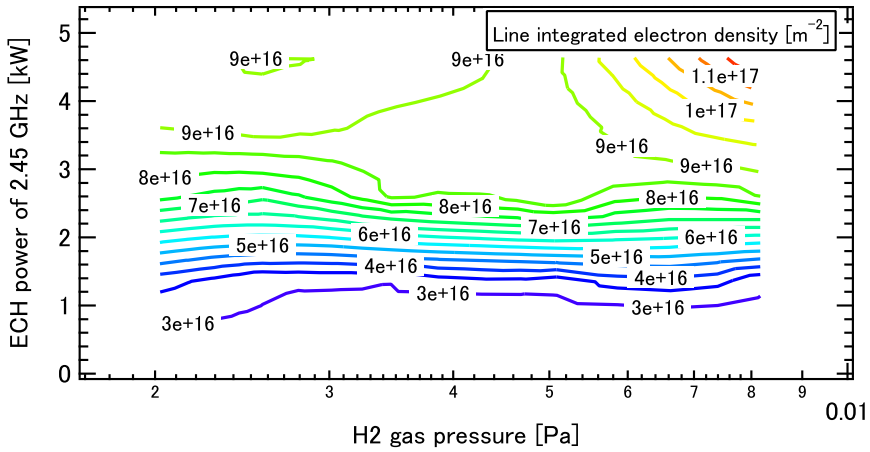

Figure 4.7: The contour map of the electron line density for various plasma discharges.

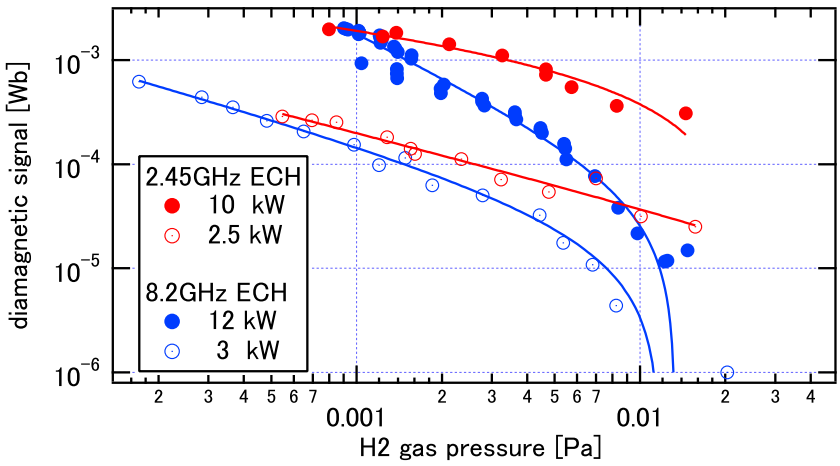

Figure 4.8: Filling gas pressure dependence of the plasma diamagnetism.

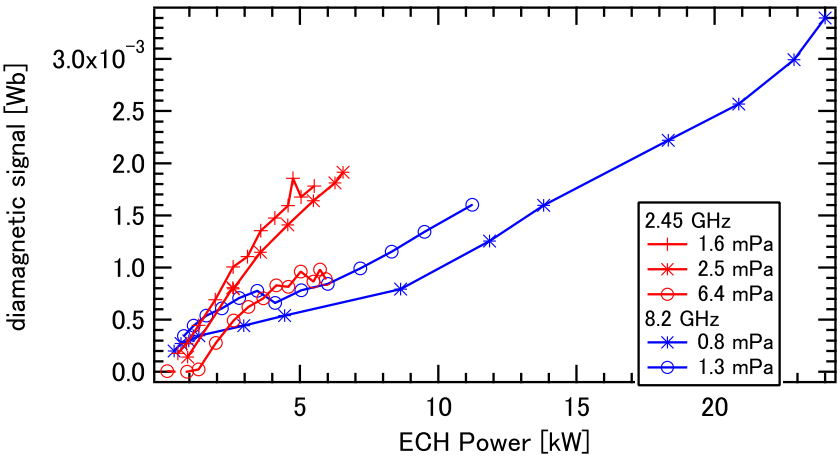

Figure 4.9: ECH power dependence of the plasma diamagnetism.

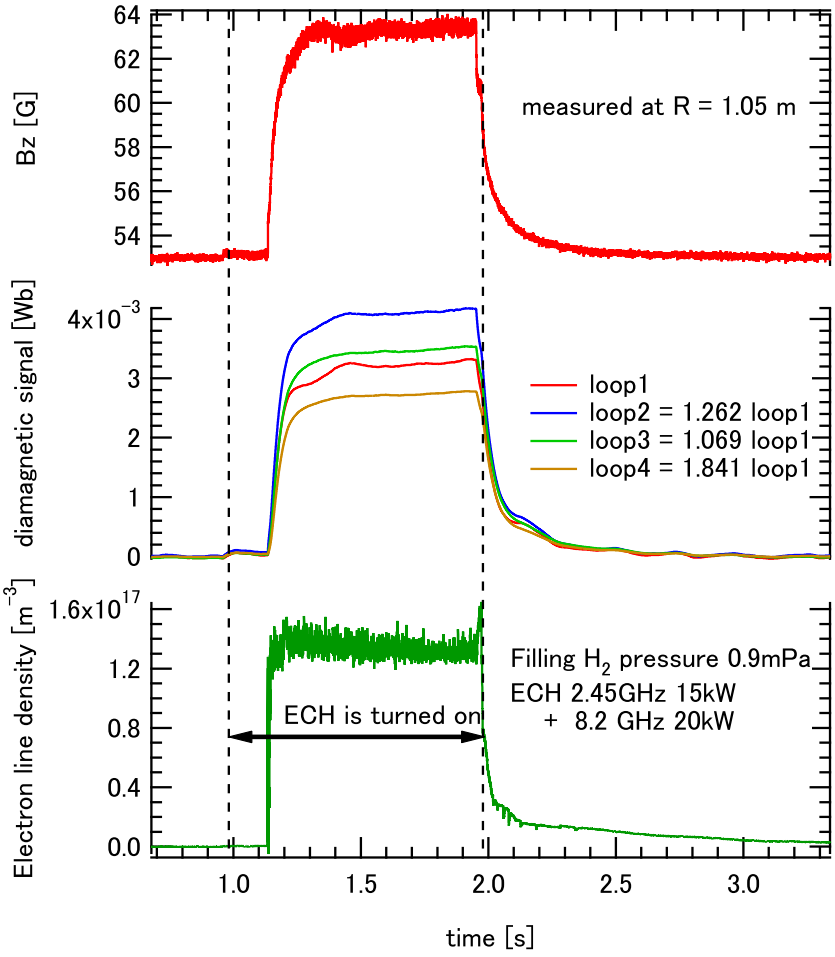

Figure 4.10: ECH power of 2.45 GHz was 15 kW and that of 8.2 GHz was 20 kW. The H_2 pressure is about 1 mPa. The vertical magnetic field measured at (R,Z)=(1.05 m, 0.0 m) is shown in the upper window. In the middle, there're the diamagnetic signals. Averaged signal was about 3.4 mWb. The line integrated electron density was about 1.3 $\times 10^{17}$ m^{-2} which is shown in the lower window.

maximum) and the ECH power of 8.2 GHz was 25 kW (25 kW maximum). The highest diamagnetic signal is shown in Fig. 4.11, whose diamagnetic signal reached 4.0 mWb. The fueling gas pressure was so lower than the shot shown in Fig. 4.10 that the time which was spend for the diamagnetism to rise up was longer (about 0.4 second). In this discharge the interferometry system was out of condition so that the electron line density is not known. The more detailed magnetic measurements for this special shot is mentioned later in Fig. 6.28 .

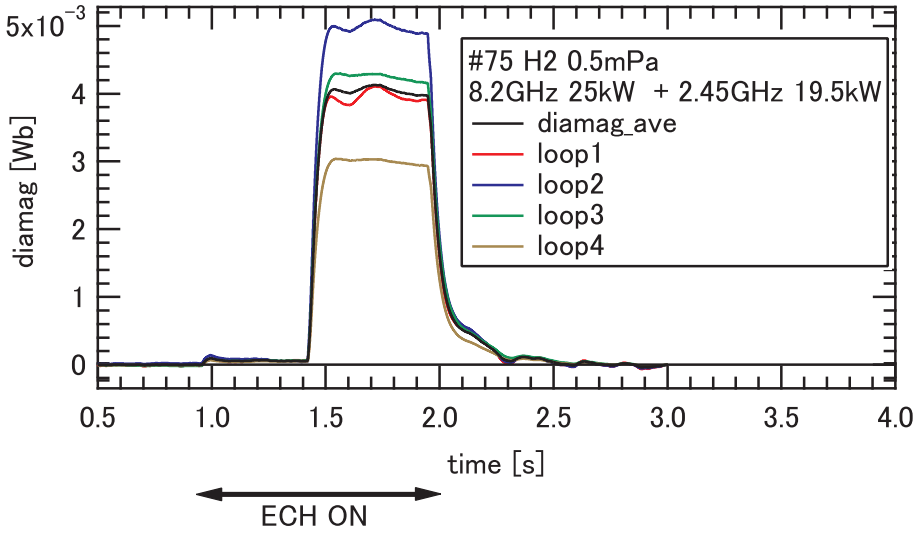

Figure 4.11: The highest diamagnetic signal which was observed in RT-1. The averaged diamagnetic signal reached 4.0 mWb.

Chapter 5

Estimate of Beta Value

5.1 Equilibrium Calculation

After an optimization of the discharge conditions, the anomalously high diamagnetism, up to 4.0 mWb, was observed in previous chapter. In the next, how to estimate the beta value of the high diamagnetic plasma is important issue. In order to analyse the plasma equilibrium, the equilibrium calculation code for RT-1 magnetic configuration was programmed mainly by Furukawa associate professor. The name of the code is RTEQ. In this chapter, the equilibrium calculation of the RT-1 plasma will be mentioned. The reference [50] [51] [52] are recommended as references.

5.1.1 Grad-Shafranov Equation

Here we consider the axisymmetric configurations and assume that the plasma pressure is isotropic. In the sylindrical coordinates (R, ϕ, Z), the magnetic field is expressed as

$$B = I\nabla\phi + \nabla\psi \times \nabla\phi, \tag{5.1}$$

using the Amperè law the current density is given by

$$\mu_0 J = -(\Delta^*\psi) + \nabla I(\psi) \times \nabla\phi. \tag{5.2}$$

Then the Grad-Shafranov equation, which describes the MHD equilibrium, is written by

$$(\Delta^*\psi) = -\mu_0 R J_t \tag{5.3}$$

$$= -\mu_0 R^2 \frac{\mathrm{d}p}{\mathrm{d}\psi} - I\frac{\mathrm{d}I}{\mathrm{d}\psi}, \tag{5.4}$$

where $J_t := J \cdot (R\nabla\phi)$, μ_0, p, $I := RB_t$ denotes the toroidal current density, space permeability, the plasma pressure and the poloidal current density, respectively. In the RT-1 configuration, the poloidal current is always zero and the Grad-Shafranov equation becomes

$$\Delta^* = R^2\nabla\cdot(\frac{1}{R^2}\nabla) \tag{5.5}$$

$$= \frac{\partial^2}{\partial R^2} - \frac{1}{R}\frac{\partial}{\partial R} + \frac{\partial^2}{\partial Z^2}. \tag{5.6}$$

The boundary condition is free boundary condition, in other words $\psi = 0$ at infinity.

5.1.2 Flowchart of the Code

The drawing of the calculation flow is shown in Fig. 5.1.

At first, equilibrium code starts the calculation with the vacuum flux function ψ_0. Then the plasma pressure is distributed for arbitrary plasma pressure function $p(\psi)$. Next the diamagnetic current is distributed in response to the plasma pressure distribution. If the given plasma pressure is relatively high in comparison to the magnetic pressure, the flux function ψ will change from the vacuum flux function ψ_0 because of a lot of diamagnetic current. Then the plasma pressure is re-distributed to the "new" flux function obtained in the previous cycle of calculations. After the iterations, the equilibrium calculation will converge to some equilibrium. At last the various equilibrium values, such as profiles of beta value, pressure and magnetic field and so on, will be output.

5.1.3 Profile Model Function

To calculate the plasma equilibrium by RTEQ, we must input some pressure profile which is a function of ψ. In this research the plasma is modeled by the pressure

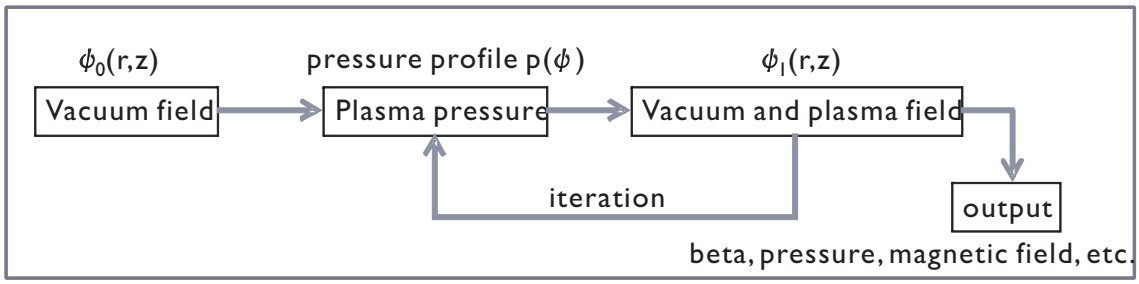

Figure 5.1: Flowchart of the equilibrium calculation code.

function which is expressed by

$$p(\psi) \propto -(\psi_1 - \psi)^P(\psi_2 - \psi)^Q, \tag{5.7}$$

where the flux function of the plasma edge is denoted by ψ_1 and ψ_2 for plasma pressure to be eliminated at the plasma bounary. In the RT-1 configuration, the innermost magnetic field is limited by the inside of the coilcase of the F-coil touching at the R = 0.18 m. On the other hand the outermost flux surface is limited by the X-point (see Fig. 2.10) or limitted by the chamber wall when the beta value is so high that the outermost surface is expanded by the diamagnetism to touch the chamber.

In this expression, the pressure profile is characterized by two numerical values, the ratio P/Q and the sum $P + Q$. The ratio P/Q defines the radial peak position of the pressure profile, while the sum $P+Q$ defines the peaking factor of the profile. The several different plasma pressure profiles are shown in Fig. 5.2. The plasma pressures on the midplane (z = 0) are shown in Fig. 5.2. The profile drawn by red line has inner steep peak, and the profile with green line has outer broad pressure peak and blue line the midium. In these equilibria in Fig. 5.2, the diamagnetic signals to be observed by the flux loops are fixed to the same value.

5.1.4 Typical Calculation Result

Here the typical results of the RTEQ code are introduced. The plasma equilibria for various profile functions were calculated for low beta plasmas. In calculation,

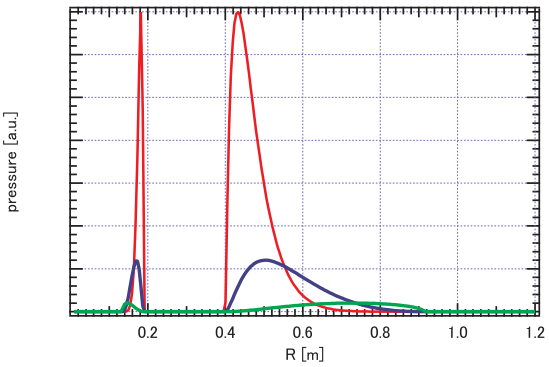

Figure 5.2: The examples of the several types of pressure profile as a function of radius. The pressure profiles on the midplane are shown.

the plasma diamagnetic signals were adusted to about 0.1 mWb.

In the case if the pressure peak radius is changed

When we changed the pressure peak radius, the ratio P/Q , is changed, the plasma equilibria are shown in Fig. 5.3. The calculation results of 3 typical peak radii, R = 0.45 m, 0.55 m and 0.70 m, are shown in Fig. 5.3. The profiles on the midplane are also shown in Fig. 5.4 and Fig. 5.5. Because the inner magnetic field strength is much larger than the outer one, if we assume that the pressure has very inner peak the plasma pressure has very steep profiles. In Fig. 5.5 the plasma beta has outer profile than the pressure, this is also because the magnetic field steeply decreases with radius.

In the case if the pressure peaking factor is changed

When we changed the pressure peaking factor, the sum $P + Q$, is changed, the plasma equilibria are shown in Fig. 5.6. The calculation results of 3 typical peaking factor, P+Q = 2, 7 and 10, are shown in Fig. 5.6. The profiles on the midplane are also shown in Fig. 5.7 and Fig. 5.8. In Fig. 5.8 the plasma beta has outer profile than the pressure profile. This shift width is more likely to be large when the peaking factor is small.

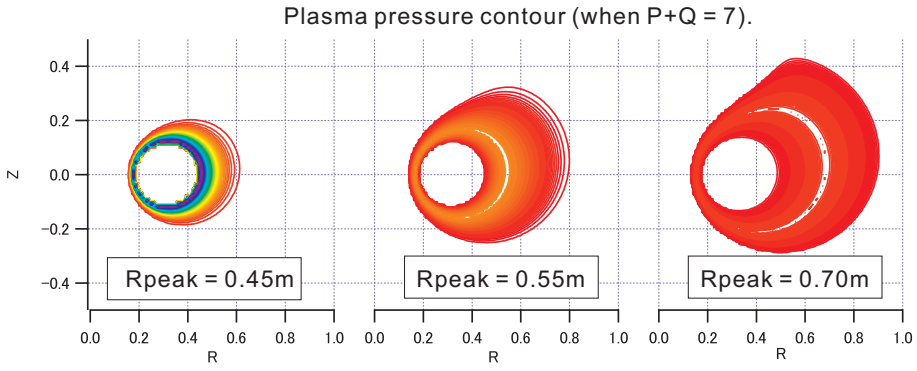

Figure 5.3: The typical equilibria which were calculated by RTEQ code for various pressure profiles. In this figure, the plasma pressure contours are shown. In the calculation, the peaking factor P+Q and diamagnetic signal are fixed to 7 and about 0.1 mWb, respectively.

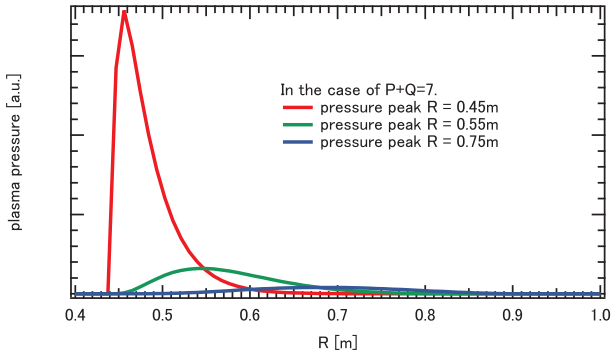

Figure 5.4: The pressure profiles of Fig. 5.3 on the midplane.

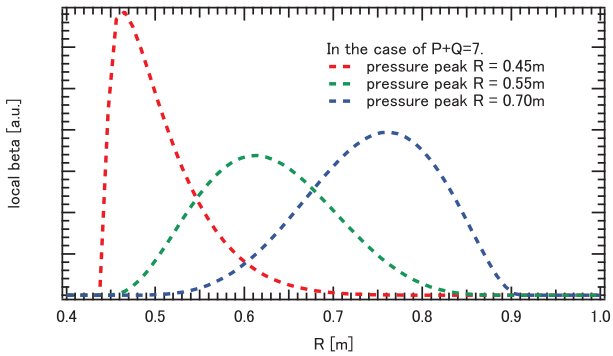

Figure 5.5: The local beta profiles of Fig. 5.3 on the midplane.

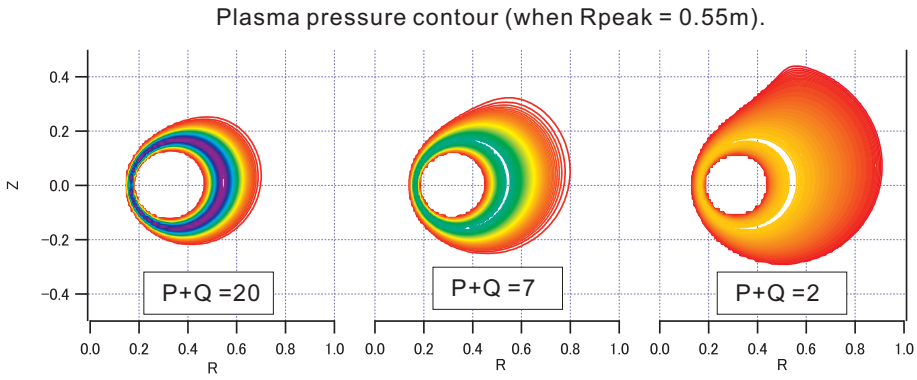

Figure 5.6: The typical equilibria which were calculated by RTEQ code for various pressure profiles. In this figure, the plasma pressure contours are shown. In the calculation, the pressure peak radius and diamagnetic signal are fixed to 0.55m and about 0.1 mWb, respectively.

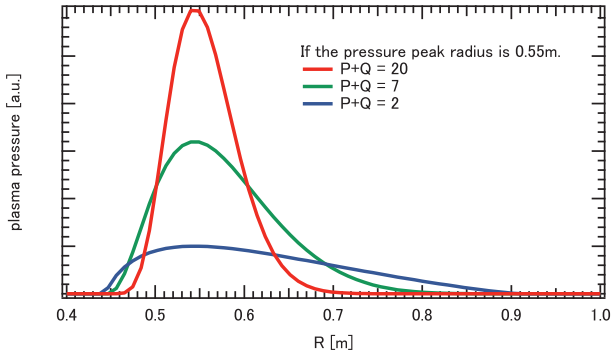

Figure 5.7: The pressure profiles of Fig. 5.6 on the midplane.

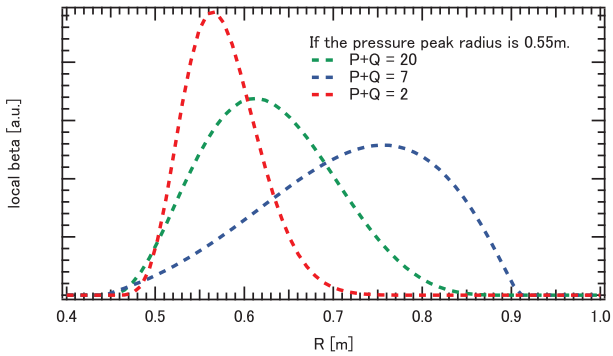

Figure 5.8: The local beta profiles of Fig. 5.6 on the midplane.

5.1.5 Conversion Coefficient of Beta Value

In the RTEQ code,if we input some pressure profile function we can obtain the local beta value profile as a result at the same time obtaining the diamagnetic signal which is expected to be measured by the loops. Then the conversion coefficient from the diamagnetic signal to the beta value can be calculated. Figure 5.9 shows a calculation results of conversion coefficients from the diamagnetic signal to the maximum local beta for various pressure profiles. When the sum P+Q is lower than 6, the coefficients don't depend on the peaking factor and clearly depend on the pressure peak radius. But when the sum P+Q becomes larger than 7, which corresponds to very steep profile, the coefficient grows up. This bifurcation, around P+Q = 7, is because pressure gradient becomes larger than that of magnetic field strength gradient. The values of coefficients vary widely depending on the pressure profiles, such as a peaking factor and a pressure peak radius. And from Fig. 5.9 we can say that the minimum coefficient is about 120 [1/Wb] and the maximum coefficient is more than 1000 [1/Wb]. Then we can conclude that the largest diamagnetic signal observed in RT-1, 4.0 mWb, corresponds to more than 50 % the local beta value.

How about the volume-averaged beta value? The calculation results of conversion coefficients from the diamagnetic signal to the volume-averaged beta for various pressure profiles is shown in Figure 5.10. Vertical axis means the beta value of the plasma which is averaged over the plasma volume where R $>$ 0.4 m, where the main confinement region of the RT-1 plasma. The values of the coefficients also vary widely depending on the pressure profile. In contradiction to the case of the local beta value, the coefficient becomes large when the peaking factor becomes large. The coefficient becomes larger when the pressure profile moves outward. These tendencies can be explained by that the RT-1 plasma confinement volume is larger in outer region of the plasma. The maximum coefficient for the averaged beta reaches 70 [1/Wb] and the minimum is less than 10 [1/Wb].

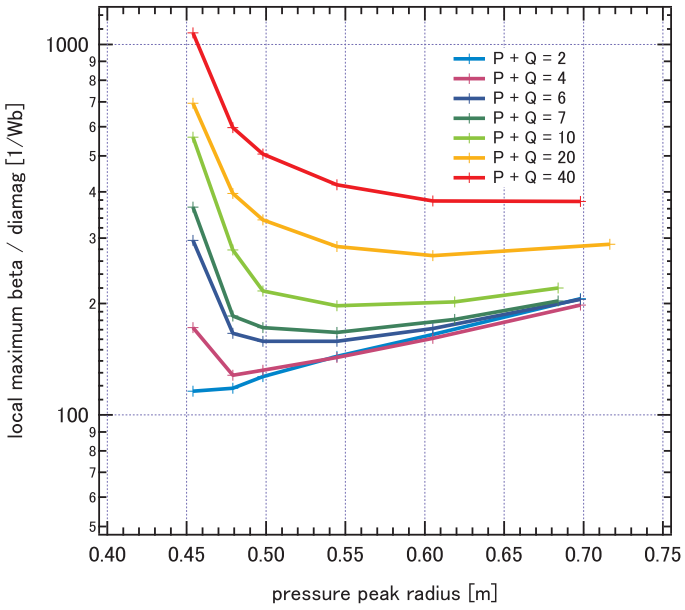

Figure 5.9: The conversion coefficient map of the local maximum beta value for various pressure profiles. The bottom axis means the radial position of the peak in the pressure profile. The sum P+Q indicates the peaking factor.

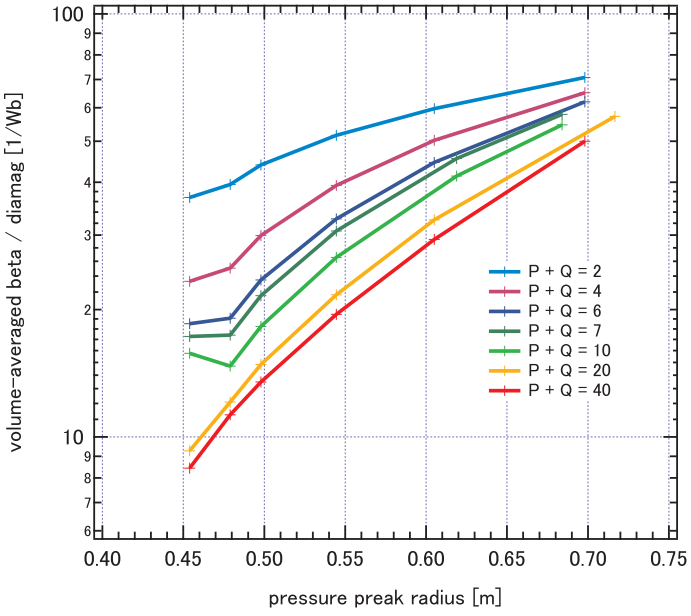

Figure 5.10: The conversion coefficient map of the volume-averaged beta value for various pressure profiles. The bottom axis means the radial position of the peak in the pressure profile. The sum P+Q indicates the peaking factor.

5.2 Consideration of Estimate Error

In the previous section, the equilibria of simple plasma pressure profile are mentioned where we analyzed the conversion coefficient of the beta value from the diamagnetic signal. The plasma pressure was assumed to be isothermal and plasma diamagnetism was limited to be low for simplicity. In the latter half on this thesis, the plasma pressure profile is going to be analyzed by using the simplest pressure model such as introduced in the previous section. However, in the actual RT-1 configuration, the plasma pressure is not necessarily isothermal. Of course, the pressure profile can not always be expressed by the function $p(\psi) \propto -(\psi_1 - \psi)^P(\psi_2 - \psi)^Q$. Additionally, there're several diamagnetic phenomena which changes the magnetic field and lead to an estimate error. In this section, we consider possible estimate errors.

5.2.1 Anisotropic Effect

In the plasma confined in the magnetic field, such as RT-1, plasma pressure can have two pressure components which are parallel and perpendicular to the magnetic field. Especially for the RT-1 device, the heating power is mainly pooled to the perpendicular pressure component because the plasma is heated by ECRH which energize the plasma particle to the direction of gyro motion (perpendicular to the magnetic field). In addition to it, the magnetic field has steep gradient to both of the perpendicular and the parallel to the field in the RT-1 configuration. Therefore the RT-1 equilibrium is likely to be affected by the pressure anisotropy like a mirror plasma confinement device.

The Grad-Shafranov equation was also derived by Furukawa associate professor and the equilibrium code was also programmed for the anisotropic pressure version. Simply speaking, if the plasma pressure is anisotropy (pressure components are $p_\parallel$ and $p_\perp$), two force balance equations are given. One is to perpendicular direction and the other is to parallel direction. The perpendicular balance equation is almost the same with the isotropic version. That is because the perpendicular pressure gradient is supported by diamagnetic current. On the other hand, the parallel

balance equation is given by

$$\frac{\partial p_{\parallel}}{\partial \theta} + \frac{p_{\perp} - p_{\parallel}}{B}\frac{\partial B}{\partial \theta} = 0, \tag{5.8}$$

where θ means the coordinate along the magnetic field and B is the magnetic field strength. If $p_{\perp} - p_{\parallel} = 0$, the pressure gradient along the magnetic field becomes zero and the plasma pressure becomes constant on the same magnetic surface, which is the same result which has been obtained by the isotropic pressure version. In an actual experimental plasma, the degree of anisotropy is not constant in all confinement region, which is to say a plasma isotropy should have spatial variance as well as a pressure has some profile in plasmas. But to measure experimentally the local anisotropy is difficult in RT-1, therefore here we consider the constant anisotropy. Here we introduce a degree of anisotropy λ. The relation of the perpendicular and parallel component of plasma pressure is expressed by

$$p_{\perp} = \lambda p_{\parallel}. \tag{5.9}$$

Therefore the isotropic plasma pressure can be simulated by choosing $\lambda = 1$. Typical plasma pressures profile when we consider the plasma anisotropy are shown in Fig. 5.11. In these calculations, the pressure profiles of perpendicular component are fixed to (P, Q) = (1, 6) on the midplane, see Fig. 5.12. Generally speaking, if the degree of anisotropy, λ, becomes large, the plasma pressure is likely to be focused in the weak field region such as outer region of the midplane. How about the convergence coefficient of beta value which was previously discussed in the isotropic case ($\lambda = 1$)? From Fig. 5.12, the local beta values should be almost the same among 3 pressure profiles. However, the plasma diamagnetic current will decrease if λ becomes larger. Therefore the coefficient will be larger when we assume the anisotropic plasma pressure. The coefficients of beta value as a function of anisotropy is shown in table 5.1.

5.2.2 Linear Effect of the Plasma Diamagnetism

This effect treats the estimate error which linearly depends on the diamagnetic signal. The linear effect is equal to the change of the magnetic field caused by

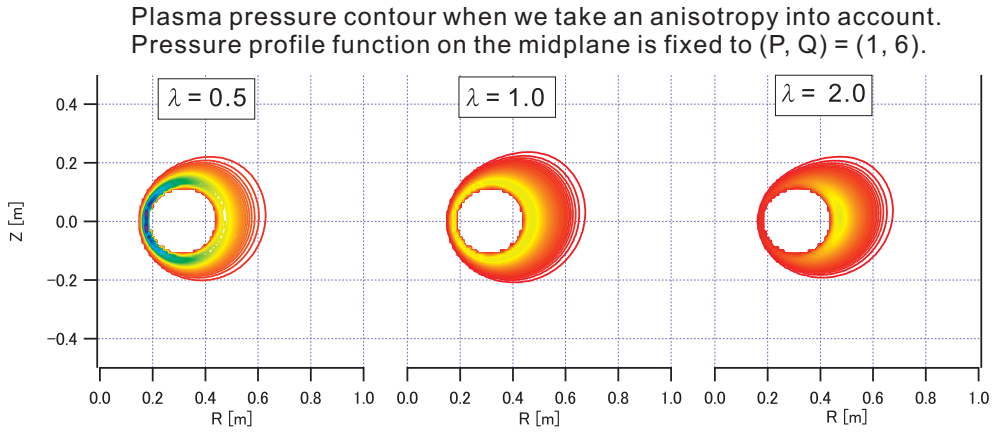

Figure 5.11: Typical plasma pressure contours when we consider the plasma anisotropy. In these calculations, we fixed the perpendicular plasma pressure profiles on the midplane to (P, Q) = (1, 6).

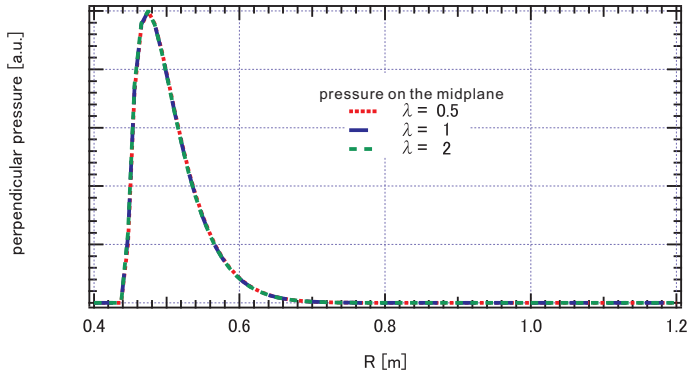

Figure 5.12: The perpendicular pressure profile of Fig. 5.11 on the midplane.

Table 5.1: The coefficient of beta value as a function of plasma anisotropy λ. The pressure function on the midplane is fixed to (P, Q) = (1, 6).

λ	local beta/diamag [1/ Wb]	averaged beta/diamag [1/Wb]
0.5	124.6	23.16
1.0	191.9	16.28
2.0	278.0	10.26
5.0	428.8	4.904

the interaction between the plasma and the levitation system. The interaction phenomenon is roughly modeled and anlysed in Section 2.1 in Chapter 3. From Fig. 3.15 and Fig. 3.16, the change of the magnetic field is cleary linear relation with the plasma diamagnetism. This phenomenon should have an affect on the magnetic measurement. Here we simply discuss how the magnetic measurement will be affected by the interaction.

When the plasma whose diamagnetic signal is 1 mWb is discharged, the F-coil position will be moved about 0.44762 mm and the L-coil current will decrease about 7.2614 A. While the magnetic flux of the F-coil will increase at the flux loop1 and loop2, on the other hand the magnetic flux of the F-coil will decrease in at the flux loop3 and loop4. It is easy to calculate how much the magnetic flux will change at arbitrary location when the L-coil current decreases or when the F-coil is displaced. The simple estimate of the error which is caused by the interaction between the plasma and the levitation system is shown in table 5.2. In the table, how much the magnetic flux is decreased by the change of the levitation system is explained. From the estimate, the plasma diamagnetic signal which is measured by the flux loops is thought to be decreased by about 10 %.

Table 5.2: Simple estimate of the error which affects the diamagnetic loop measurement by the interaction phenomenon.

	F-coil		L-coil		
	interaction coefficient		interaction coefficient		
flux loop	+0.448	mm/mWb	-7.26	A/mWb	error
loop1	0.00407	mWb/mm	0.0200	mWb/A	-0.1430
loop2	0.00285	mWb/mm	0.0169	mWb/A	-0.1210
loop3	− 0.00285	mWb/mm	0.00956	mWb/A	-0.0707
loop4	− 0.00407	mWb/mm	0.00752	mWb/A	-0.0564

5.2.3 Nonlinear Effect of the Plasma Diamagnetism

In this subsection nonlinear effect of the plasma diamagnetism is introduced. An example of the nonlinear effect of the plasma diamagnetism is shown in Fig. 5.13. In Fig. 5.13, we calculated the plasma equilibria when we fix the pressure profile and we change the plasma pressure. If the plasma diamagnetism is lower than 0.1 mWb, the beta value varies linearly with the diamagnetic signal. Therefore we focused on the coefficient between the diamagnetic signal and the beta value, which correponds to a slope of the line in Fig. 5.13. But if the diamagnetism becomes larger than 0.1 mWb, the linearity between the diamagnetism and the beta value becomes gradually invalid. This nolinearity is expalined by two reasons. One is the volume expansion of the plasma and the other is the decrease of the magnetic field in the vicinity of the plasma core. Fig. 5.14 shows the example of the plasma volume expansion and Fig. 5.17 shows the example of the decrease of the magnetic field in the vicinity of the core.

In Fig. 5.14, the outermost magnetic surface, which is drawn by a black line, is getting closer to the vacuum chamber wall when we increase the plasma pressure. The pressure contour is shown in Fig. 5.15 and the pressure (perpendicular) profile on the midplane is shown in Fig. 5.16. In Fig. 5.15, the same colour lines do not mean the same value of plasma pressure among 3 contour maps, you have to see Fig. 5.16 in order to see the precise relation of the pressure profiles on midplane. It is clear that not only the plasma volume but also the plasma pressure profile is extended outward.

While the pressure profile is deformed by the plasma diamagnetism the magnetic field strength is largely changed by plasma. The change of the magnetic field strength directly affects the estimate of the beta value because the beta value is calculated by dividing the plasma pressure by the magnetic field strength. In an usual plasma pressure profile, the magnetic field decreases in the vicinity of the plasma core and increases in the plasma edge, which is because the magnetic flux in the vicinity of the core is pushed away toward the plasma edge. An example of the change of the magnetic field sterength on the midplane is shown in Fig. 5.17 and the magnetic

field strength profile of each component (B_z and B_r) on the midplane is shown in Fig. 5.18 and Fig, 5.19. When the plasma diamagnetism is relatively high, B_z component decrease (Fig. 5.18) and on the other hand B_r component increases (Fig. 5.19). But as a total the magnetic field surely decreases in the vicinity of the core, which is expected from the physical intuition. When the diamagnetic signal is 3.83 mWb, the magnetic field sterength decreases about up to 30 % and this effect plays a large role in the nonlinear effect of the plasma diamagnetism.

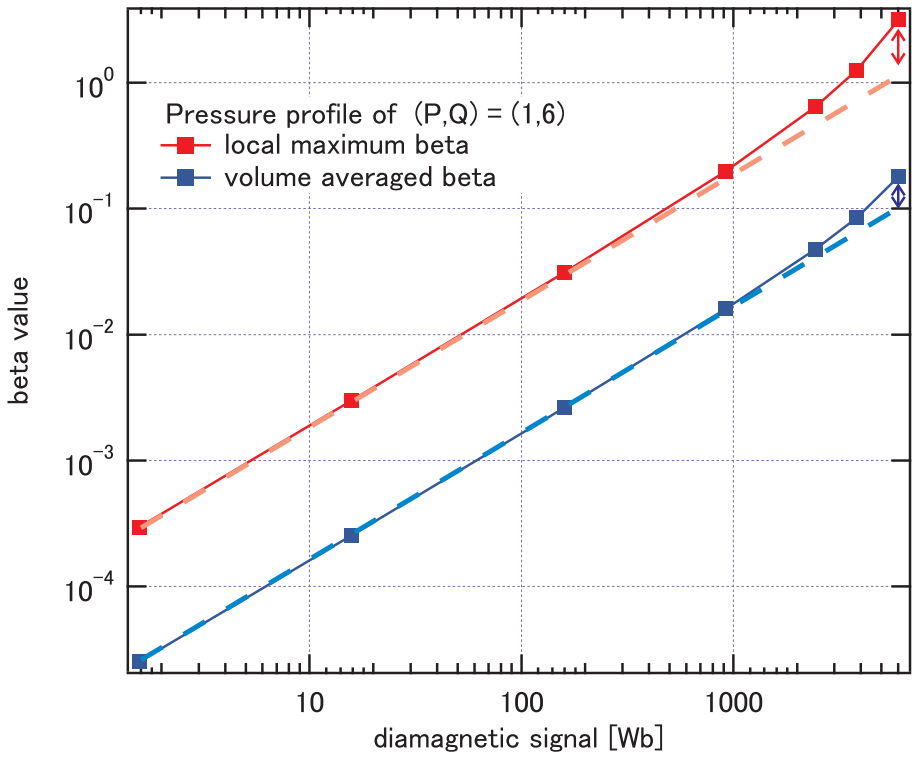

Figure 5.13: An example of the plasma diamagnetism. In this case we assumed that the pressure profile function is given by (P, Q)=(1, 6). In the high beta or high diamagnetic region, the linearity between the beta value and the diamagnetism gradually becomes incorrect.

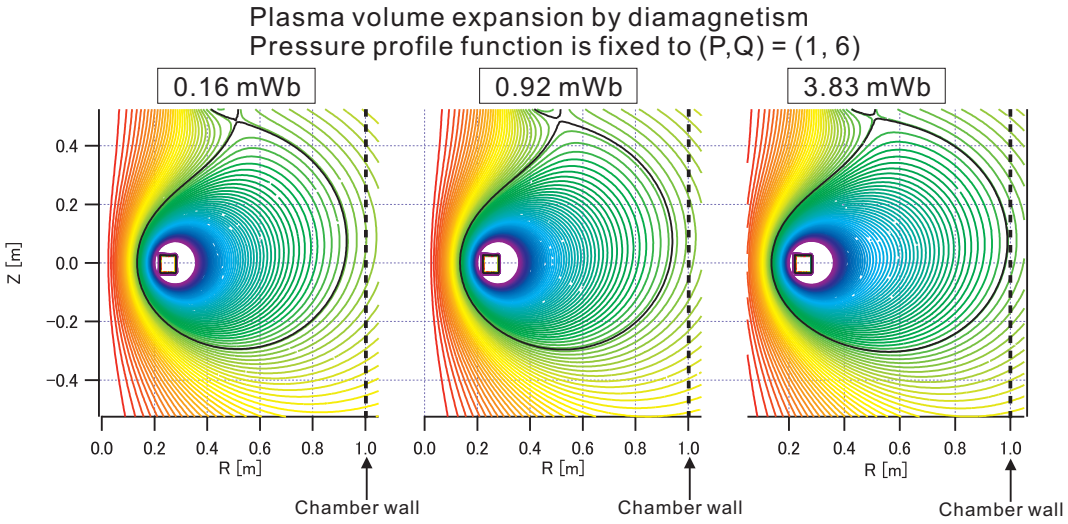

Figure 5.14: An example of the plasma volume expansion. The outermost magnetic surface, black line, is expanded in high diamagnetic plasmas. In this case we assumed that the pressure profile function is given by (P, Q)=(1, 6).

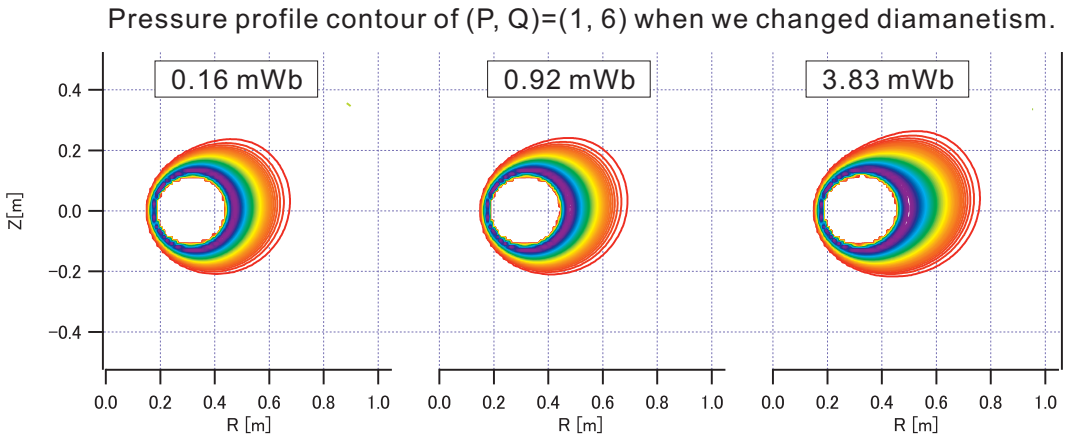

Figure 5.15: An example of the plasma pressure expansion. The plasma pressure profile is surely changed by the diamagnetic current of the high beta plasma. Be careful not to confuse that the same colour lines mean the same value of pressure among three contour maps. The precise relations of the pressure profile among them are shown in Fig. 5.16..

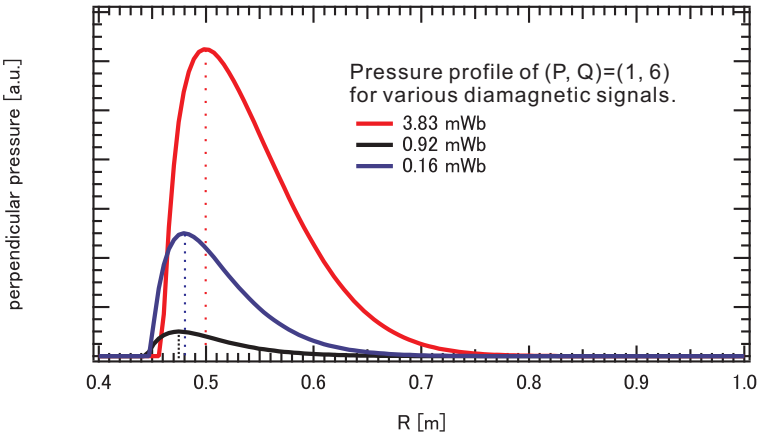

Figure 5.16: The pressure profile on the midplane for the plasma shown in Fig. 5.15. The pressure peak radius is obviously moved outward by plasma diamagnetism.

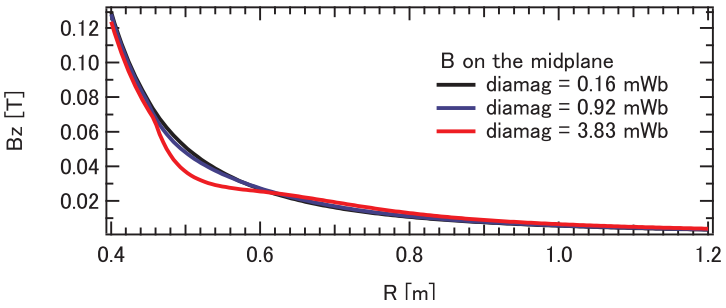

Figure 5.17: An example of the decrease of the magnetic field strength B. The magnetic field in the vicinity of the plasma core (R $\sim$ 0.50 m) is largely decreased by plasma diamagnetism in high diamagnetic plasmas. In this case we assumed that the pressure profile function is given by (P, Q)=(1, 6).

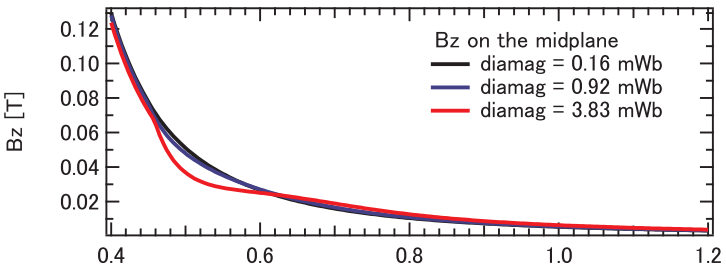

Figure 5.18: An example of the decrease of the magnetic field strength B_z. The magnetic field in the vicinity of the plasma core (R $\sim$ 0.50 m) is largely decreased by plasma diamagnetism in high diamagnetic plasmas.

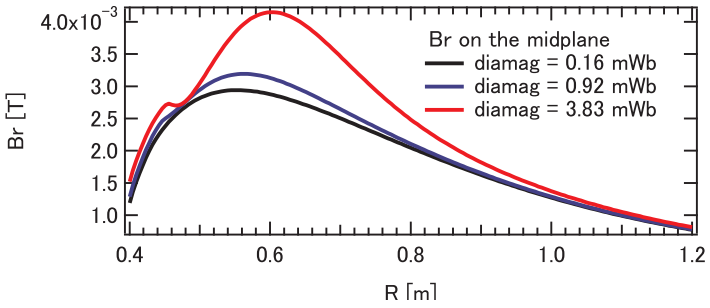

Figure 5.19: An example of the decrease of the magnetic field strength B_r. B_r is slightly increased in just outside of the plsma core (R $\sim$ 0.60 m) unlike B and B_z.

5.2.4 Consideration

In this section, we discussed the possible error on the estimate of the beta value. First of all, we have large estimate error in assuming the plasma pressure function, such as $p(\psi) \propto -(\psi_1 - \psi)^P(\psi_2 - \psi)^Q$. In the simplest equilibrium model, we can estimate the beta value of the plasma by comparing the diamagnetic signals if the pressure function is known. But when we consider other effects, we have to modify the equilibrium and the estimate of the beta value should change. From the discussion of this section, it can be said that if we consider other effects the estimate value becomes larger than the simplest model. In the actual experimental plasma, the anisotropy and even the plasma pressure function is not known at all. Therefore

how to determine the plasma pressure function is focused from here for simplicity. In the other words, the other effect well be neglected and the simplest equilibrium model is focused in order to understand how the plasma pressure profile is like. Then if we couled determine the plasma pressure function and couled estimate the beta value of the plasma, it is possible to discuss that the actual beta value is at least more than the beta value which is estimated from the simplest model.

Chapter 6

Experimental Analysis of Magnetic Field Structure

6.1 Purposes of Measurement of the Plasma Diamagnetism

The rough estimate of the plasma local beta in magnetospheric plasma is mentioned in previous chapter. The measurement of plasma diamagnetism with the flux loop is surely one of the reliable measurement system to observe a change of magnetic field structure near the plasma, but the flux loop measurement has several problems. One is that the loops are located at outside of the vacuum chamber and it is very difficult to estimate the detailed pressure profile of the plasma. The other is that the loops are wound around a thick metal-made chamber wall and then the eddy current on the chamber prevent us from measure the relatively fast magnetic events, such as the decay of the plasma energy after ECH is turned off or sudden collapse resulted from the instability. To overcome these issues two magnetic probe systems which use a hall sensor are developed for the higher resolution measurements in space and time.

6.2 Diamagnetic Field inside the Plasma

6.2.1 Magnetic Probe System on the Midplane

The developed hall magnetic probe system on the mid-plane is shown in Fig. 6.1 and Fig. 6.2, this probe system is inserted to the RT-1 plasma and is able to measure the magnetic field on the mid-plane. The model number of the sensor which we adopt is SS495A1 or SS496A fabricated by Honeywell. The measurement range of the sensor is ± 670 G or 840 G, which corresponds to the vertical magnetic field at R = 0.468 m or 0.443 m on the RT-1 midplane. The profile of the vertical magnetic field on the RT-1 midplane is shown in Fig. 6.3. Because the innermost magnetic surface is crossing at R = 0.44 m, almost all of the midplane can be probed. The power source of the sensor is DC ± 2.5 V constant-voltage source and the output gain of the sensor is about 3.12 mV/G or 2.5 mV/G. The gain of each sensors are calibrated individually by the magnetic coil which is made for calibration of sensors. The photograph of the calibration coil which was newly developed in this research is shown in Fig. 6.4. The calibration coil is composed of a Hlemholtz coil, or a pair of coils which are facing coaxially, and it has two holes in order to calibrate the magnetic probe by two directions, such as a parallel and a perpendicular to a probe axis. The frequency response of the sensor is tested by the calibration coil is shown in Fig. 6.5, the signal of the hall sensor is recorded to a PC through a 1.5 kHz LPF which is inserted in order to reduce a noise.

The typical waveforms of the hall probe is shown in Fig. 6.6. The hall sensor was at R = 0.60 m in this plasma shot. Because the hall sensor can detect the vacuum field unlike the other magnetic measurement which uses the law of electromagnetic induction, 274 G of vacuum field is detected in Fig. 6.6.

Improvement of the Probe

The structure of the probe was upgraded by 3 steps. First we tested whether the plasma local diamagnetism can be measured by the hall probe whose length was short, which can measure only at R > 0.6 m: which is named ”old probe” in the

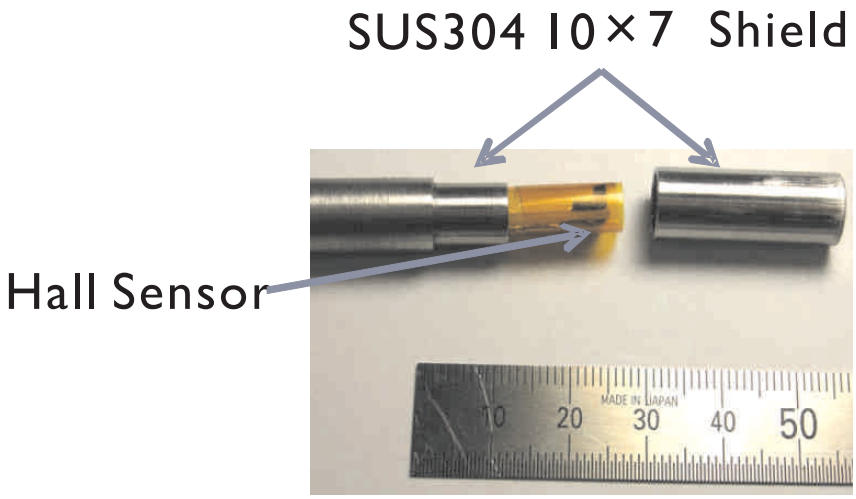

Figure 6.1: Photographic view of the head of the hall sensor mount structure. The sensor is mounted on plastic plate and the mount is shielded by stainless steel tube for electrostatic shielding. The unit of the scale is given in mm.

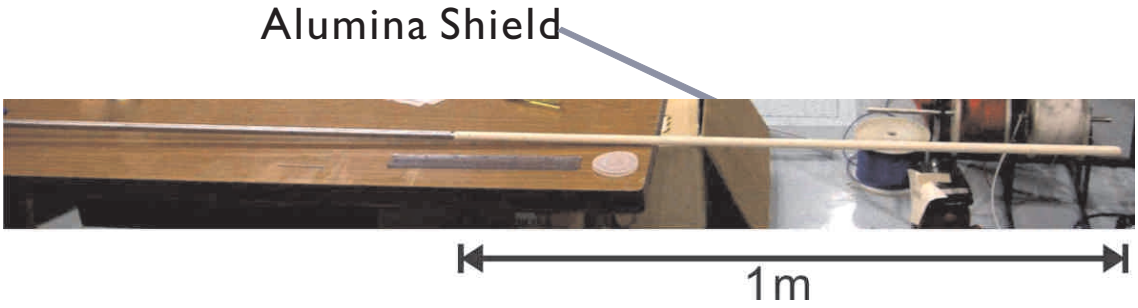

Figure 6.2: Photographic view of the probe. The head of the stainless steel is shilded by alumina tube.

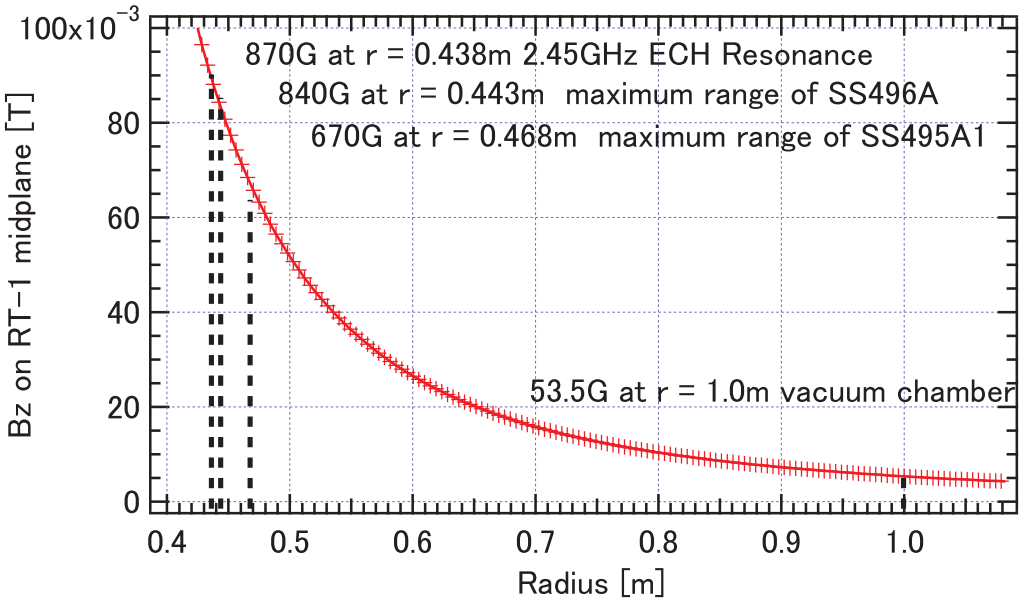

Figure 6.3: The vacuum magnetic field to the vertical direction on the RT-1 midplane, which is calculation result.

experimental result. After we succeeded the test, we lengthened the probe structure in order to conduct a magnetic measurement for almost all of the plasma confinement region. The second probe system could measure at R $>$ 0.465 m, which is restricted by the magnetic range of the hall element SS495A1: which is named "new probe" or "1 point probe" in the experimental result. Finally we upgraded it to multi channnel probe to measure the magnetic field at the different position at the same time. Figure 6.7 is a photograph of multi-channel probe which has 9 channels in 0.5 m: which is named "multipoint probe".

In the actual experiment, the probe is inserted into the plasma whose diamagnetic signal is less than about 100 μWb in order to protect the probe from damages from the hot plasma.

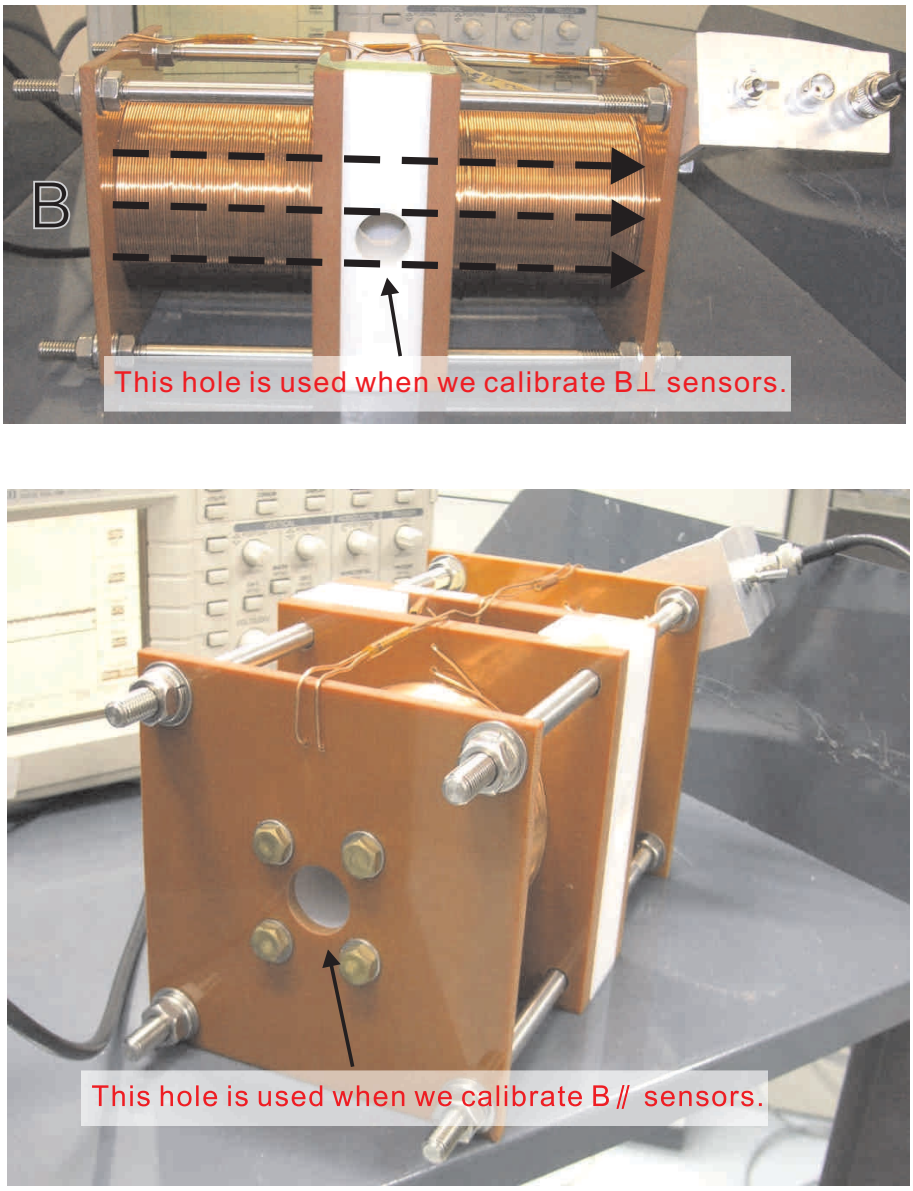

Figure 6.4: The photographs of the calibration coil. The coil is composed of a Helmholtz coil and is able to calibrate sensors in two directions, pararell and perpendicular to a probe axis.

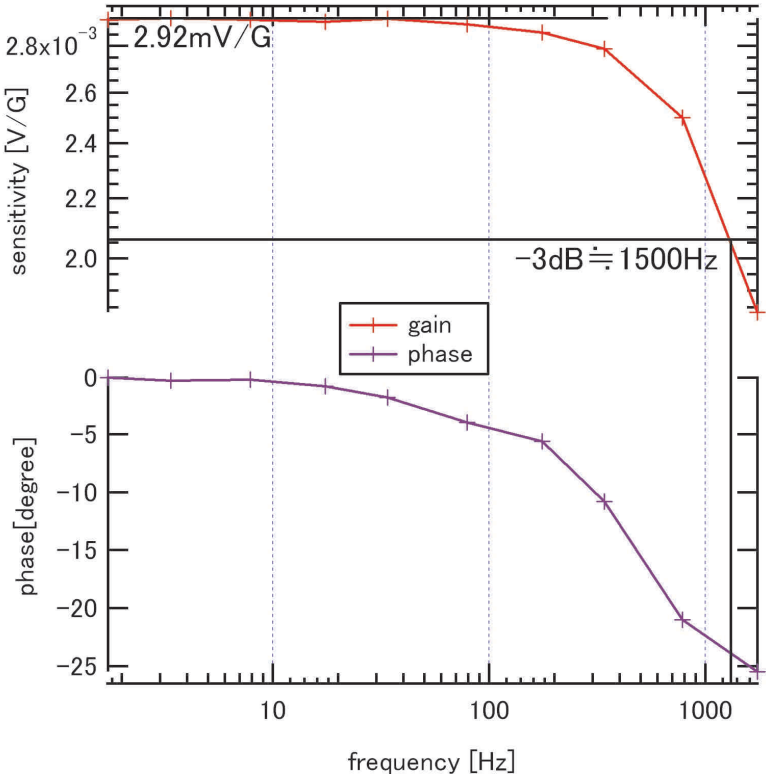

Figure 6.5: The frequency response of the hall probe. The reponse speed is governed by the LPF.

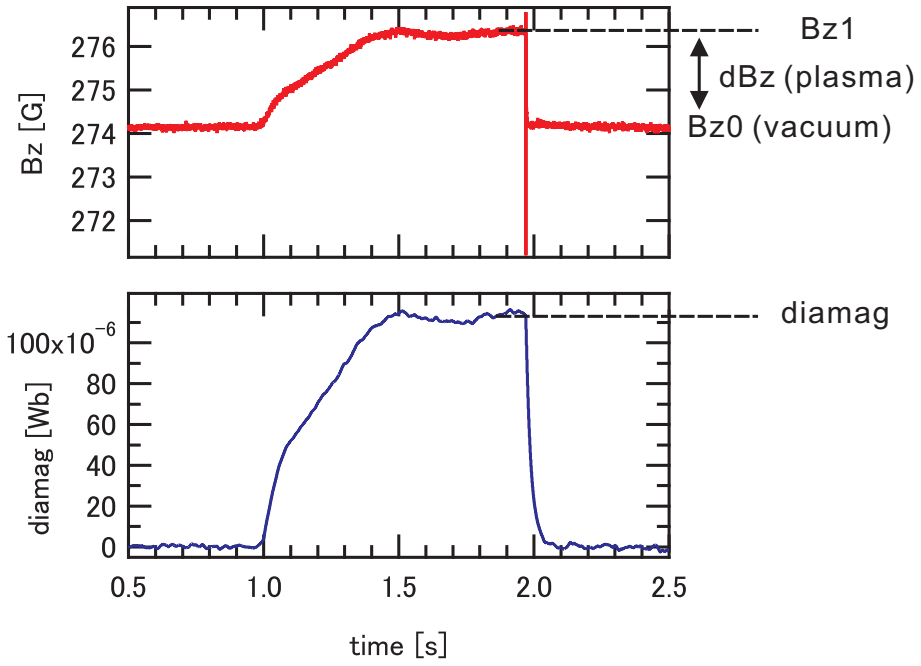

Figure 6.6: Typical waveforms of the hall probe. The output of the hall sensor is shown in the upper window and corresponding diamagnetic signal is shown in the lower window.

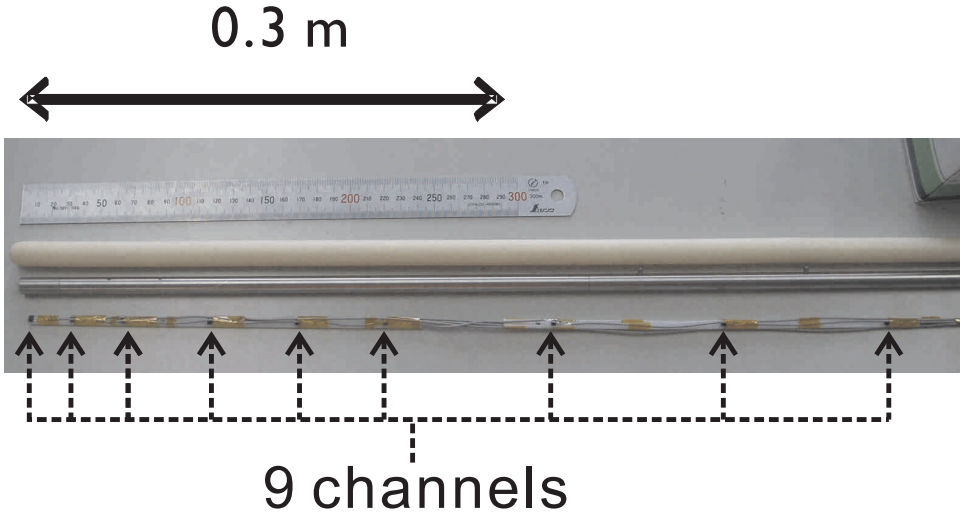

Figure 6.7: The photograph of the multi-channel probe.

6.2.2 Numerical Estimate of Magnetic Field inside the Plasma

Before we proceed to the actual plasma experiment, we calculated the expected change of the magnetic field inside of the plasma by the RTEQ code. The calculation results for a variety of pressure profile are shown in Fig. 6.8 and Fig. 6.9. Figures 6.8 and 6.9 show a magnetic field structure which is produced by the plasma diamagnetism in the upper window and corresponding pressure profile function in the lower window. The change of the magnetic field structure is normalized by the diamagnetic signal of the flux loop, therefore the unit is given by [G/Wb]. In Fig. 6.8, the peaking factor $P + Q$ is fixed and the pressure peak radius P/Q is varied. On the other hand, the peaking factor $P + Q$ is varied and the pressure peak radius P/Q is fixed in Fig. 6.9. From these numerical estimate, we can say that the vertical magnetic field B_z in outer region of the plasma is increased by the plasma diamagnetism which pushes outward the magnetic field lines from the pressure peak region. And because the plasma diamagnetic structure shows a characteristic changes near the pressure peak region, we confirmed that the direct measurement of the plasma diamagnetic field structure enables us to know the plasma pressure profile in detail.

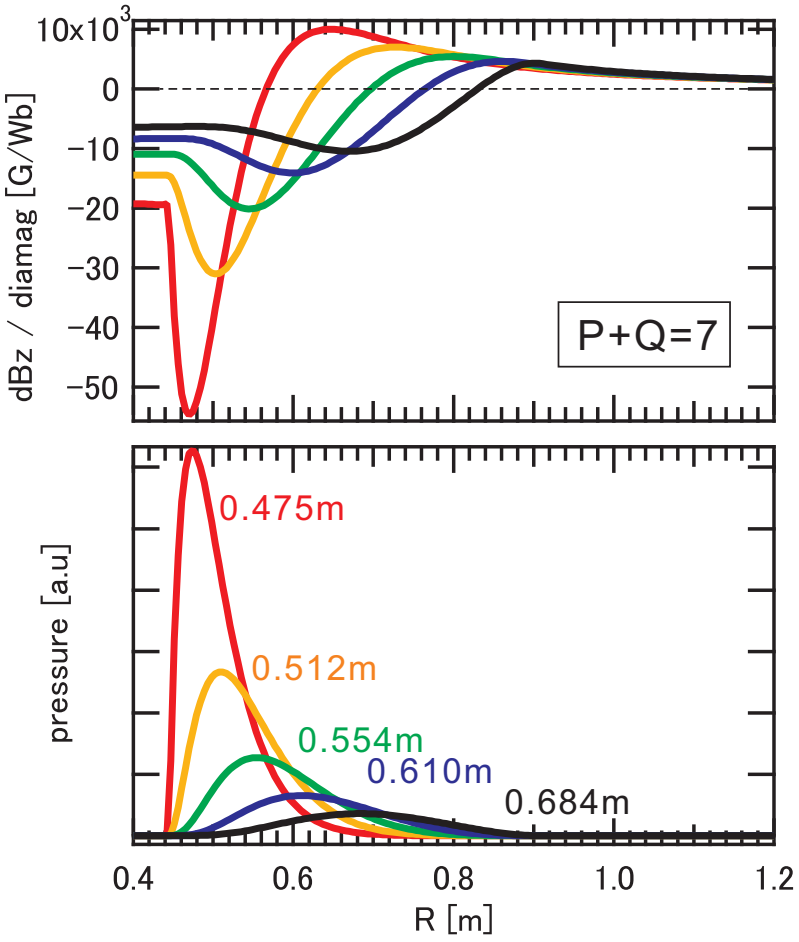

Figure 6.8: Calculation result of the magnetic field inside of the plasma. The peaking factor $P + Q$ is fixed and the pressure peak radius P/Q is varied.

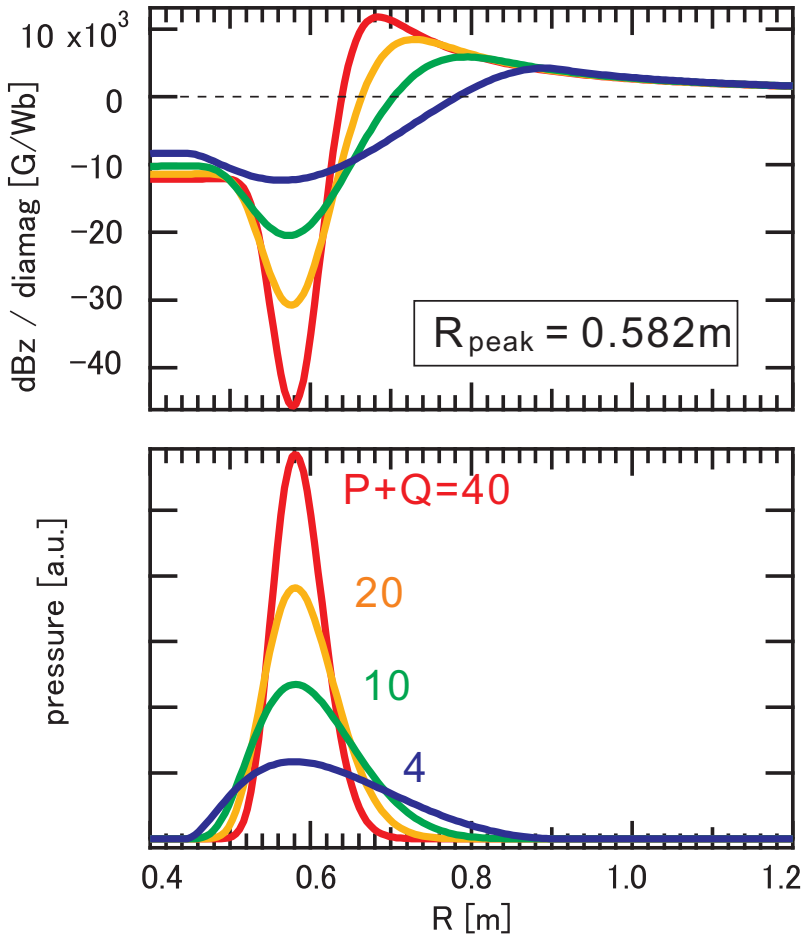

Figure 6.9: Calculation result of the magnetic field inside of the plasma. The peaking factor $P + Q$ is varied and the pressure peak radius P/Q is fixed.

6.2.3 Experimental Result

We experimented the measurement of the magnetic field structure of the magnetospheric plasma. The plasma diamagnetism is suppressed to about 100 μWb by adjusting ECH power sufficiently low in order to protect the hall probe from the thermal shock of the plasma. The measurement of the magnetic field inside the plasma was conducted on the plasmas which were heated by different frequencies of ECH, such as 2.45 GHz and 8.2 GHz. Because the location of the electron cyclotron resonance layer is different, we expect that the plasma pressure profiles are also different. The filling gas pressure was about 3 mPa in these experiments.

In the case of Plasma with 2.45 GHz ECH

The experimental result is shown in Fig. 6.10. Markers denote the actual experimental results and thd dotted line denotes the best-fit calculation result. By lengthening the probe, decrease of the magnetic field due to the plasma diamagnetism was observed. The best-fit pressure profile has a peak at R = 0.47 m and whose peaking factor is $P + Q = 7$. In this experiment, "old probe" (shorter) and "new probe" (longer) are used.

In the case of Plasma with 8.2 GHz ECH

The experimental result is shown in Fig. 6.11. The change of the magnetic field is positive in all of the measurement region and the best-fit pressure profile has a peak at R = 0.45 m and whose peaking factor is $P + Q = 40$. This pressure profile means that the plasma pressure is localized at just nearby the floating coil and the pressure gradient of it is very large. In this experiment, "1 point probe" and "multi point probe" are used.

6.2.4 Considerations

The measured pressure profile of the magnetospheric plasma has a steep peak ($P + Q > 6$) nearby the F-coil (R < 0.48 m). Although the experimental conditions were very different from the high beta plasma experiment, if we assume the high

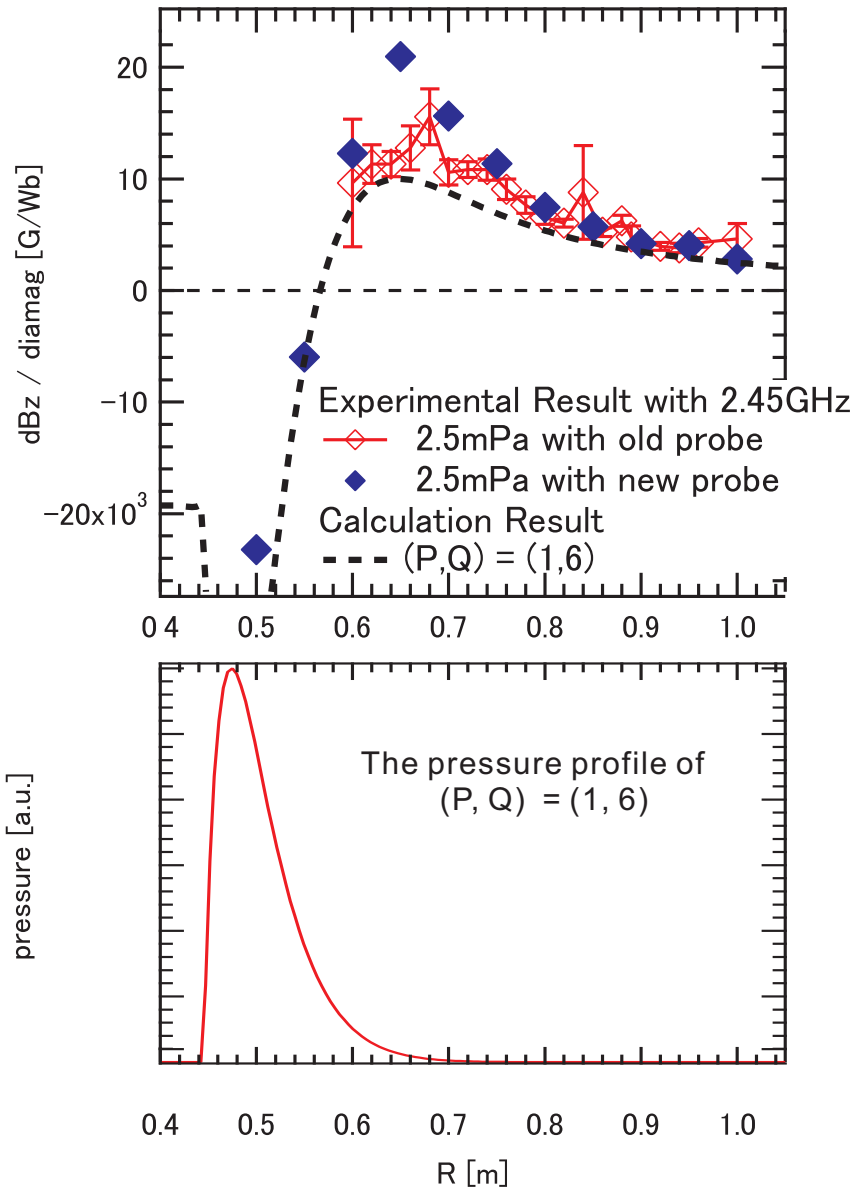

Figure 6.10: Experimental results of the plasma diamagnetic field structures heated when we heated the plasma by 2.45 GHz ECH.

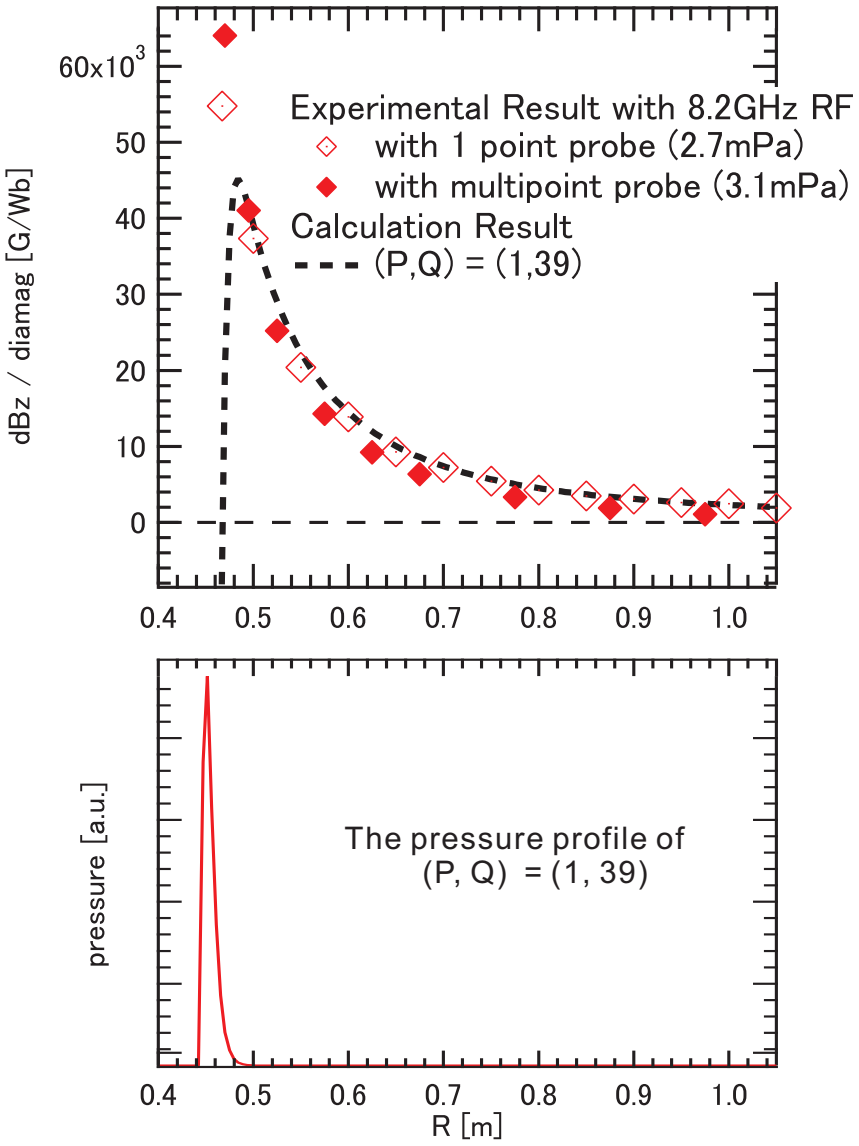

Figure 6.11: Experimental results of the plasma diamagnetic field structures when we heated the plasma by 8.2 GHz ECH.

beta plasma in RT-1 , which has 4 mWb of diamagnetic signal at most, has the same profile the estimate of the local beta value becomes order of unity. But in this measurement, the probe itself has a possibility to influence the pressure profile. Because the head of the probe shines during the discharge and we found that the probe was damaged after the experiment. The photograph of the probe whose head was black-burned is shown in Fig. 6.12

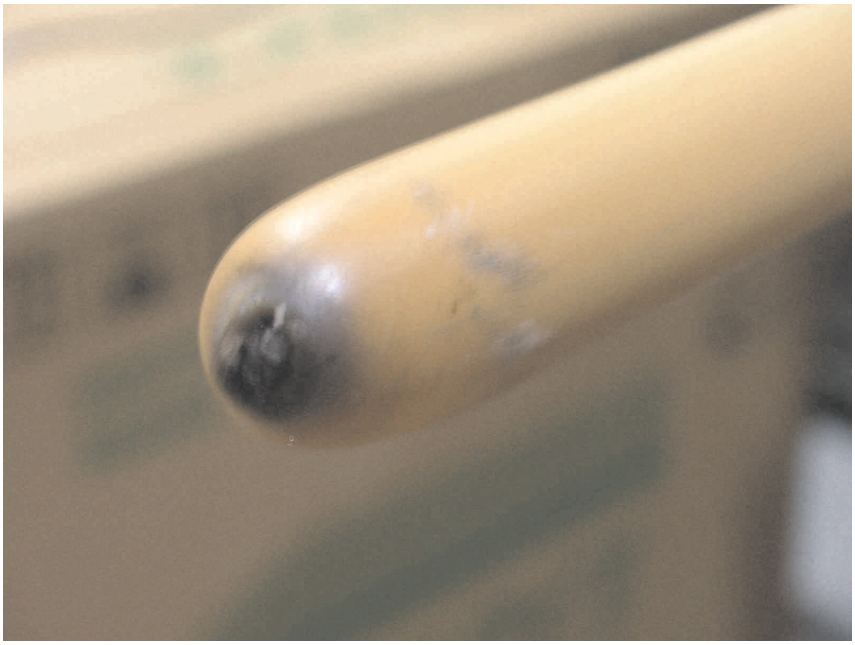

Figure 6.12: Photograph of the head of the probe after the severe plasma experiment.

6.3 Evaluation of the Energy Confinement Time

Energy confinement time of the plasma can be evaluated by focusing on the plasma decay phase just after the ECH is stopped. Typical decay phase of the RT-1 plasma is shown in Fig. 6.13. Two decay times are found in magnetic signals, fast decay time and slow one. The H_2 pressure dependency of those decay time is shown in Fig. 6.15. The fast and slow decay times clearly depends on the filling neutral gas pressure. The slow decay time, about 200 ms, is considered as the energy confinement time of the hot electrons. At the present we have not revealed what the fast decay time is. One might think that the fast decay time represents a component of a cold bulk electron, but the decay time of the bulk electron thought to be much faster than 10 ms from the decay time analysis of the interferometer measurement, which is shown in 6.14.

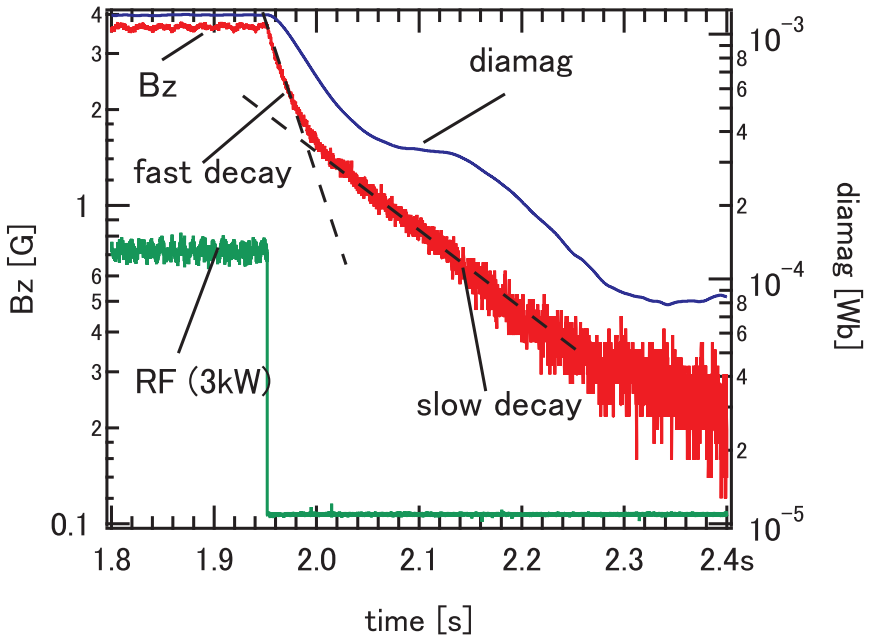

Figure 6.13: Typical waveforms of the energy decay phase just after the ECH is turned off. B_z was measured by the hall probe located at (R, Z) = (1.05 m, 0.0 m).

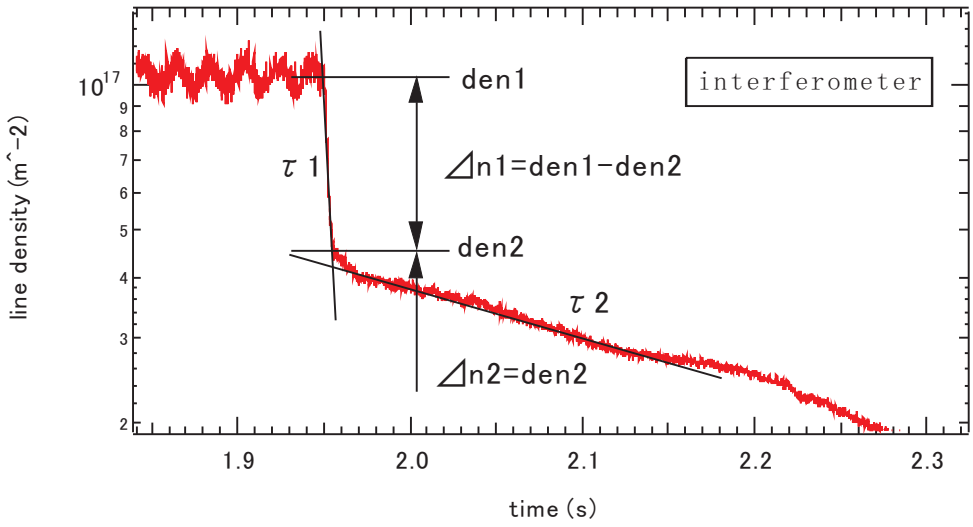

Figure 6.14: Typical waveforms of the electron density decay phase just after the ECH is turned off. Vertical axis means a line-integrated electron density. More than half of the electron decreases within 5 ms ($\tau 1$) after the ECH is turned off.

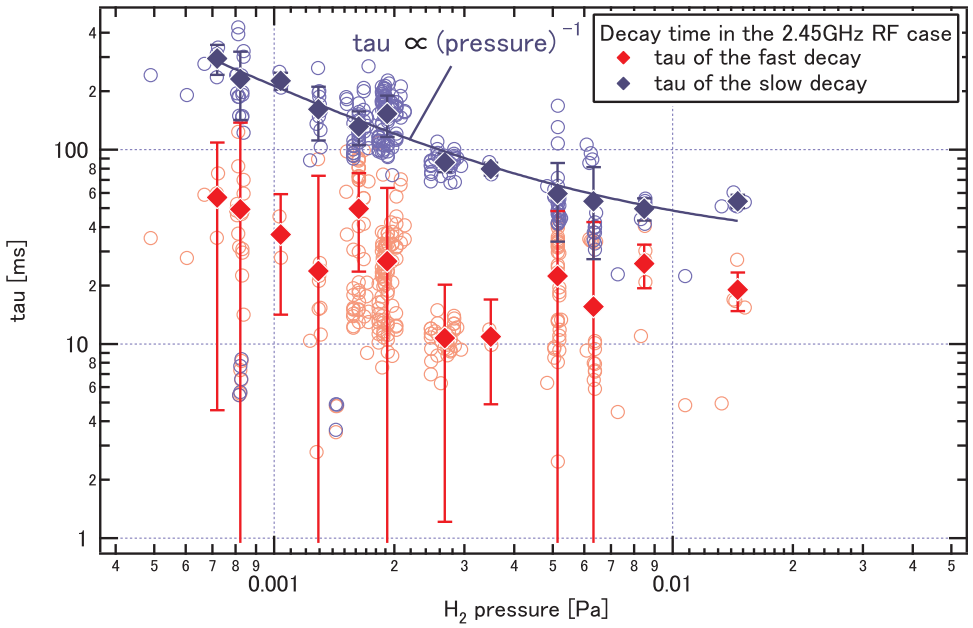

Figure 6.15: H_2 gas pressure dependency of the two decay times of the energy confinement of the RT-1 plasma.

6.3.1 Discharge Condition Dependence of Energy Confinement Time

Discharge condition dependency of the slow decay time is investigated. The slow decay time for different frequencies of ECH is compared in Fig. 6.16. And whether levitated or supported is compared in Fig. 6.17. As a result, the slow decay time of the plasma diamagnetic signal does not depend on the condition of the ECH frequency and it also does not depend on whether the F-coil is levitated or not. This indicates that the slow decay time is related to the confinement time of the hot elecrons which are bounced by a magnetic mirror. In other words, when we do'nt levitate the F-coil the plasma which is not bounced by the strong magnetic field will be completely lost through the support structure.

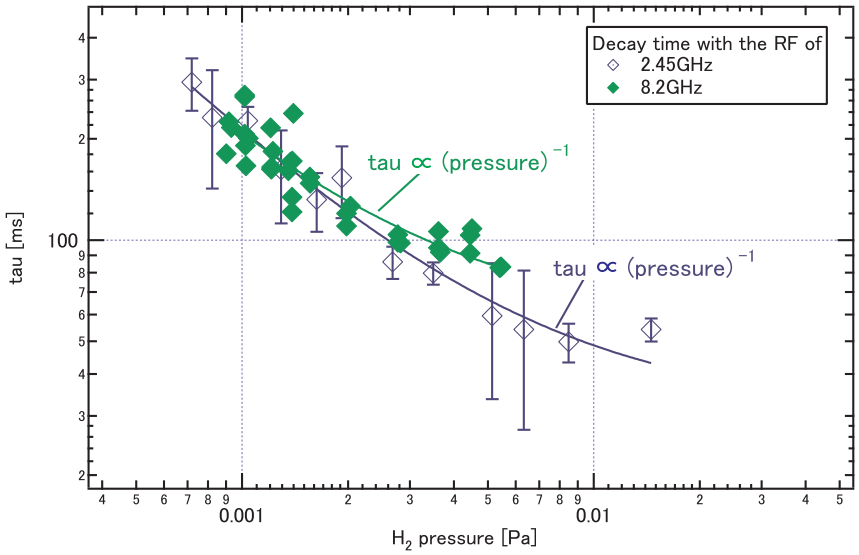

Figure 6.16: The slow decay times of the plasma energy which were heated by different frequencies of ECH are compared. The slow decay time doesn't depend on the ECH frequency.

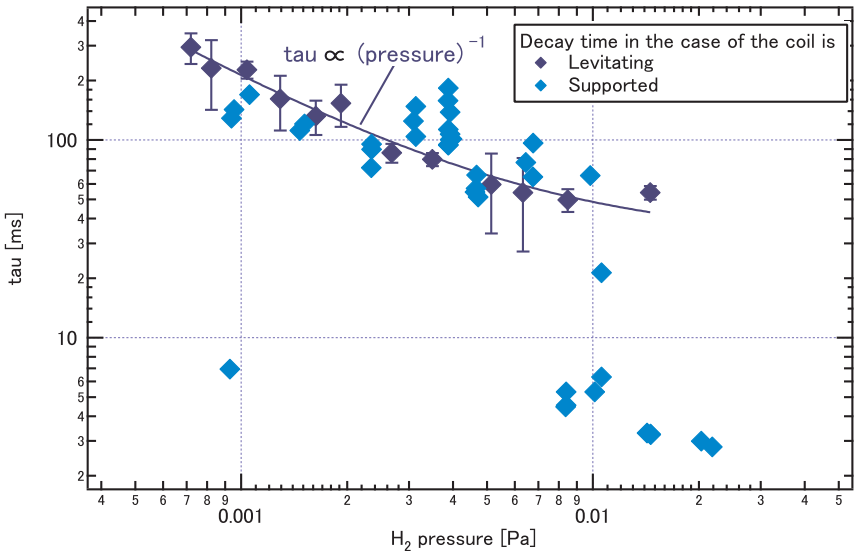

Figure 6.17: The slow decay time of the plasma energy. Whether the F-coil is levitated or supported is compared.

6.4 Diamagnetic Field below the Plasma

6.4.1 Development of the Hall Probe under the Plasma

The direct measurement of the diamagnetic field is mentioned in the previous section. The direct measurement of the diamagnetic field is very useful to obtain the detailed pressure profile but the measurement cannot be conducted for the high beta plasma in which we are most interested, because we want prevent the probe to be broken by a thermal shock of the high beta plasma. To overcome the problem, another Hall probe measurement system was developed. Because the diamagnetic field outside of the plasma on the midplane (R > 1.0 m) doesn't depend on the pressure profile (see Fig. 6.8 and Fig. 6.9), new Hall probe measurement system is installed just under the plasma. The probe is separated from the outermost magnetic surfaces.

The arrangement of the probe and the plasma is shown in Fig. 6.18. The probe is removed from the outermost magnetic surface about 10 cm. The probe system has 14 Hall elements, they can measure the radial, B_r, and vertical, B_z, magnetic fields at 7 positions. The positions of the Hall elements are (R, Z) = (0.405 m, -0.40 m), (0.430 m, -0.40 m), (0.455 m, -0.40 m), (0.480 m, -0.40 m), (0.505 m, -0.40 m), (0.530 m, -0.40 m) and (0.555 m, -0.40 m). The photographs of the interior and the exterior of the probe are shown in Fig. 6.19 and Fig. 6.20. The photograph of the probes installed in the vacuum chamber is shown in Fig. 6.21.

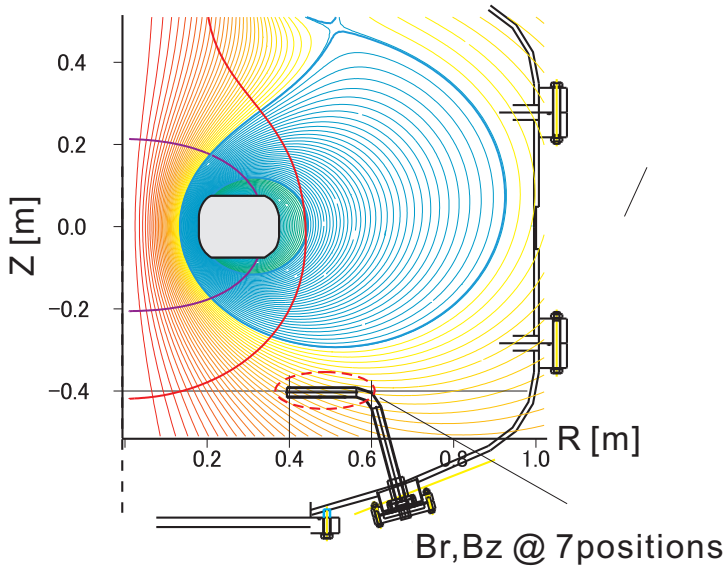

Figure 6.18: The arrangement of the new Hall probe system and the magnetic surfaces.

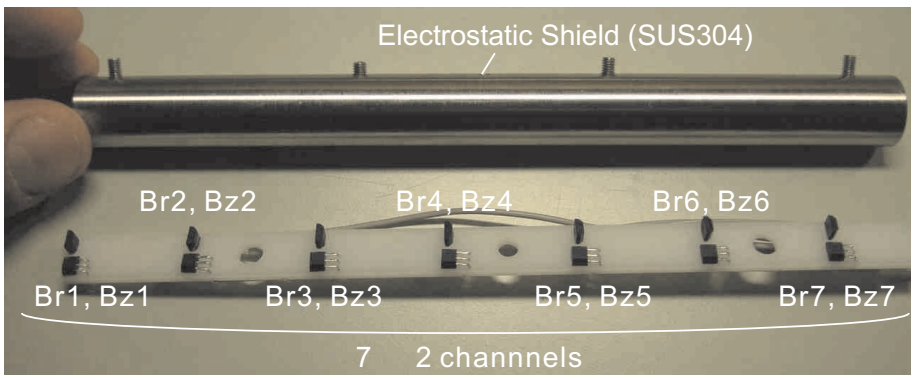

Figure 6.19: The photograph of the interior of the probe. Fourteen Hall elements are mounted. Hall elements are electrically shielded by stainless steel (SUS304).

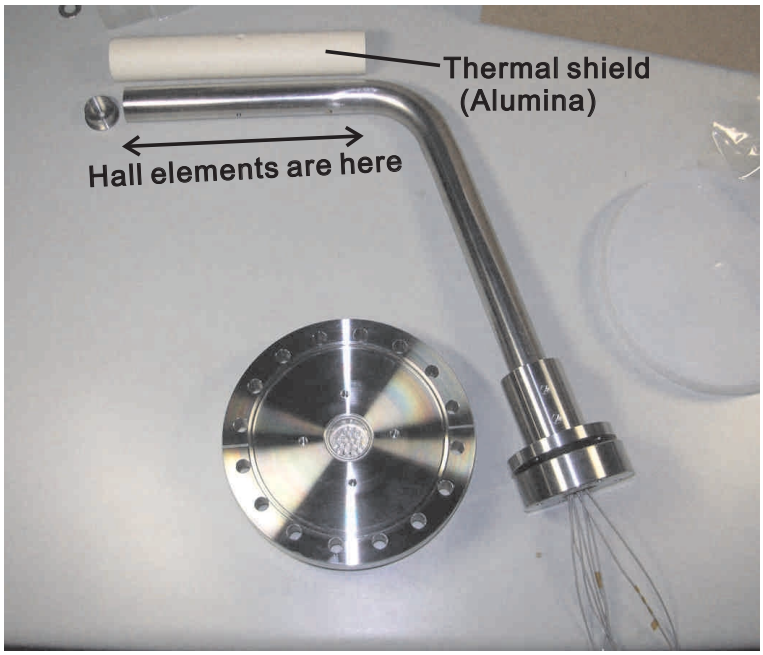

Figure 6.20: The photograph of the exterior of the probe. The probe is thermally protected by a ceramic pipe.

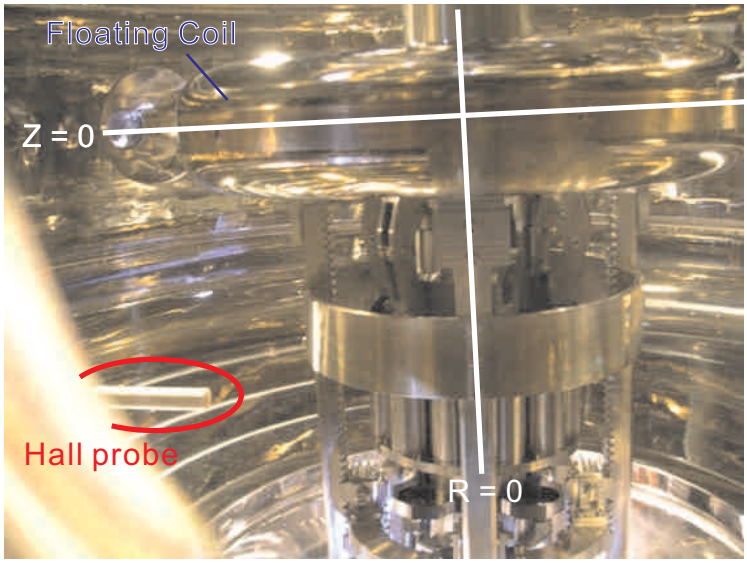

Figure 6.21: The photograph of the Hall probe which is installed in the vacuum chamber.

6.4.2 Numerical Estimate of Magnetic Field below the Plasma

Before we proceed to the experimental result of the measurement of the magnetic field below the plasma, calculation results of the diamagnetic field which is expected to be measured by the hall probe which was installed below the plasma is mentioned. In the calculation we can simulate the diamagnetic field of the plasma who has arbitray pressure profile. Here we show the example of the calculation results in Fig. 6.22 and Fig. 6.23. Figure 6.22 shows the case if we changed the pressure peak radius while the pressure peaking factor P+Q is fixed to 7. On the other hand, the case if we changed the peaking factor while the peak radius is fixed to 0.60 m is shown in Fig. 6.23.

From Fig. 6.22 and Fig. 6.23, we can say that diamagnetic field below the plasma depends on the plasma pressure function and it especially depends on the location of the pressure peak. If the pressure peak radius is changed ouward the normalized diamagnetic field under the plasma will decrease in almost all locations of the hall sensors.

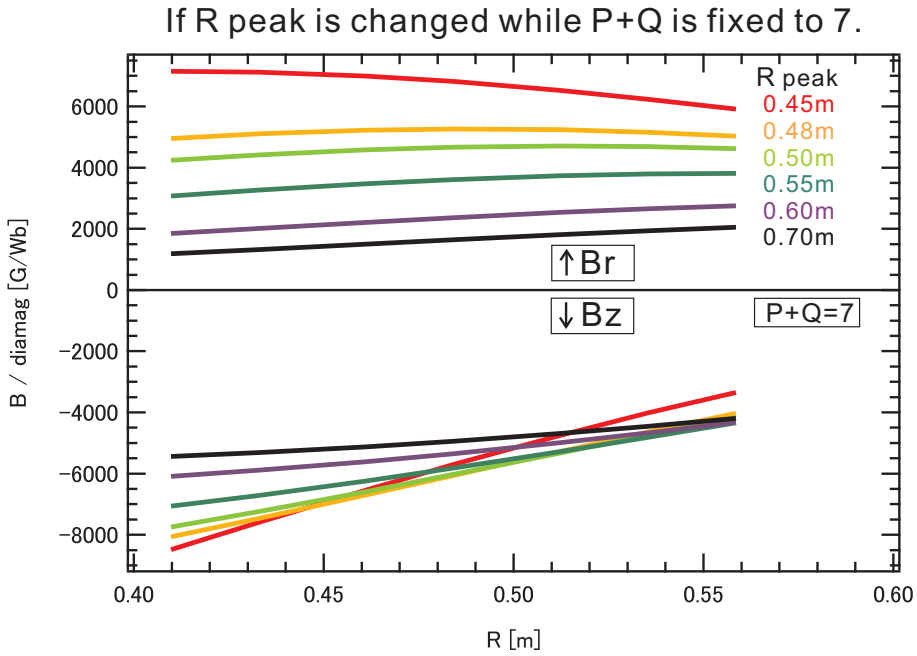

Figure 6.22: Calculation results of the diamagnetic field which will be measured by the hall probe under the plasma. In this case the plasma peaking factor is fixed and the location of the pressure peak is changed. The vertical axis means the change of the magnetic field which is normalized by the diamagnetic signal measured by the flux loops.

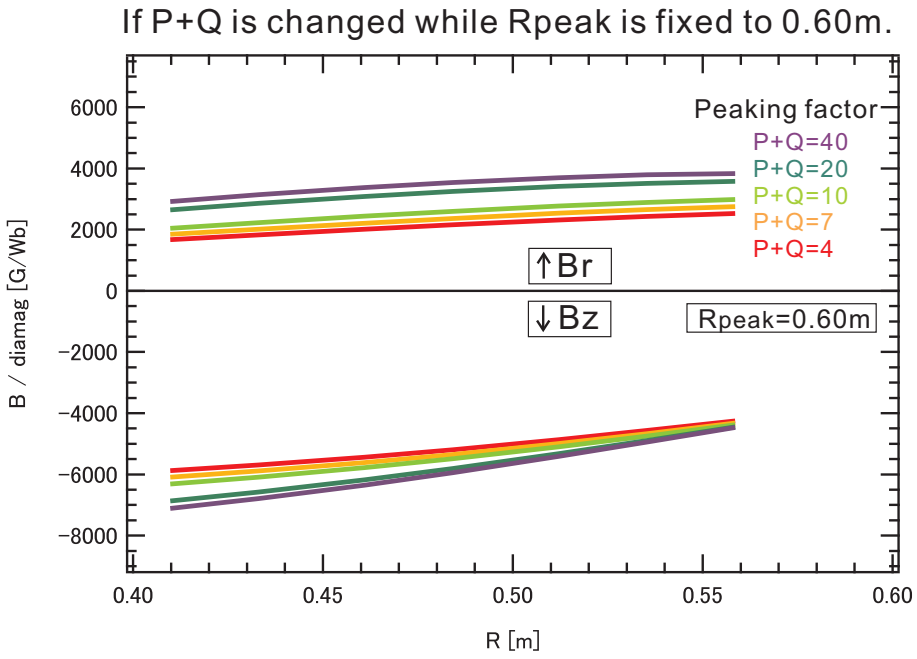

Figure 6.23: Calculation results of the diamagnetic field which will be measured by the hall probe under the plasma. In this case the pressure peak radius is fixed and the peaking factor is changed. The vertical axis means the change of the magnetic field which is normalized by the diamagnetic signal measured by the flux loops.

6.4.3 Typical Waveforms of the Magnetic Field below the Plasma

As previously mentioned, the Hall elements can measure a DC component of the magnetic field. The accuracy of the measurement system can be ascertained by comparing the measured and calculatied vacuum field. The experimental results are shown in Fig. 6.24. Figure 6.24 shows that the measurement accuracy of the Hall probe system is about 1 %.

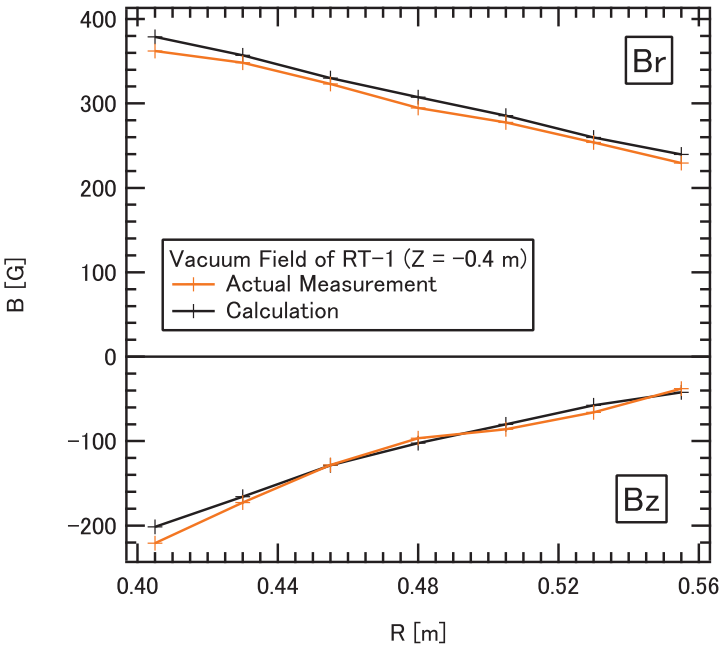

Figure 6.24: Experimental result and calculation result of the vacuum magnetic field at the Hall probe.

Typical waveforms of the magnetic field under the plasma is shown in Fig. 6.25 and Fig. 6.26. Figures 6.25 and 6.26 shows a plasma discharge with 8.2 GHz and 2.45 GHz microwave, respectively. The diamagnetic signals are shown in upper window and the magnetic field measured by the Hall probe system are shown in lower window. The plasma is discharged for 1 second from t = 1.0 s. Vertical axis means a magnetic field of the plasma, which is calculated by reducing the vacuum field from the measured magnetic field.

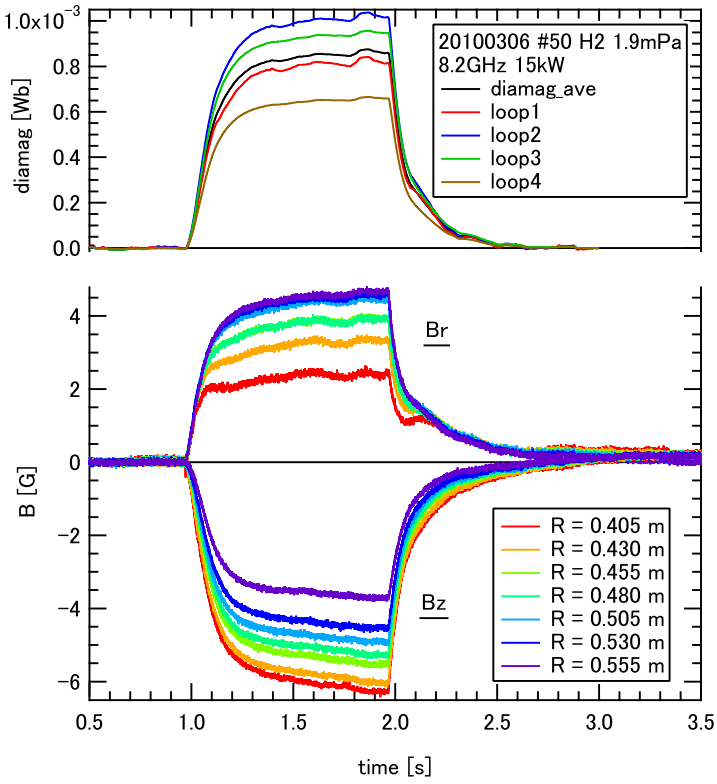

Figure 6.25: Typical waveforms of the magnetic field measurement for the plasma heated by 8.2 GHz microwave. The filling H_2 pressure is 1.9 mPa.

In order to obtain the pressure profile of the plasma, we analyze the magnetic signals at different positions. At first we calculate the plasma magnetic field at each position and then divide them by the diamagnetic signal. The results after those treatments are shown in Fig. 6.27. The left axis means the magnetic field normalized by the plasma diamagnetism, which has a dimension of "L^{-2}". In general, this

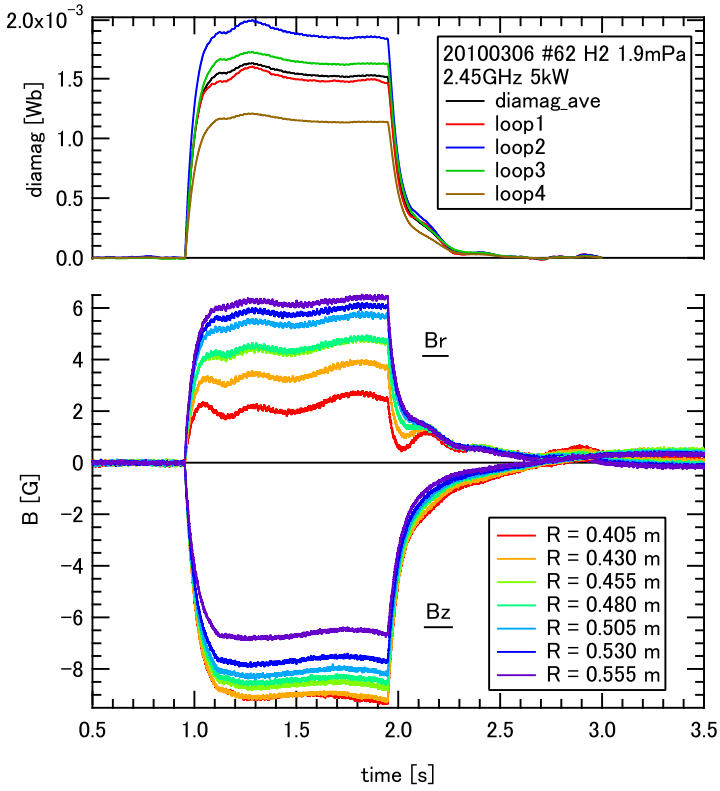

Figure 6.26: Typical waveforms of the magnetic field measurement for the plasma heated by 2.45 GHz microwave. The filling H_2 pressure is 1.9 mPa.

normalized magnetic field decrease if the plasma pressure profile moves outward. The diamagnetic structure below the plasma with 2.45 GHz microwave is clearly different from one with 8.2 GHz, These result shows us that the plasma pressure profiles are different for different microwave frequencies, which is the same conclusion as obtained by the direct measurement of the plasma magnetic field inside the low-beta plasma. This difference of the pressure profile can be explained by the position of the resonance surfaces of the heating maicrowave. The results also show that the plasma pressure profile is almost the same in 1.9 mPa and 4.0 mPa of the filling gas pressure.

The pressure profile of the plasma discharged by the 2.45GHz, which is shown in Fig. 6.26, is expressed by (P,Q) = (4, 3) or (6, 4) if we choose the approximate pressure function from the calculation result of RTEQ code. The pressure peak radii

are R = 0.610 m and 0.624 m, respectively. The maximum local beta conversion coefficients are 180 [1/Wb] and 204 [1/Wb], respectively.

And then the pressure profile of the plasma discharged by the 8.2 GHz, which is shown in Fig. 6.25, is approximately expressed by (P,Q) = (1, 4) or (2, 5) or (3, 7) from the RTEQ code. The pressure peak radii are R = 0.488 m, 0.507 m and 0.512 m, respectively. The maximum local beta conversion coefficients are 143 [1/Wb], 168 [1/Wb], 206 [1/Wb] respectively.

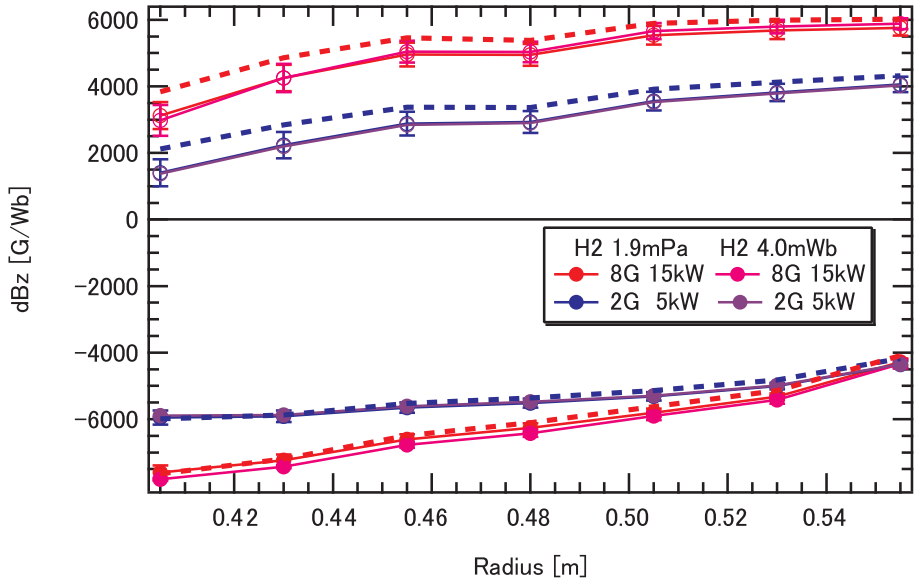

Figure 6.27: The analysed magnetic field of the plasma. The left axis means the magnetic field normalized by the plasma diamagnetism, which has a dimension of "L^{-2}". Dotted lines indicate the normalized magnetic field without the effect of the displacement of the F-coil position.

6.4.4 The Highest Diamagnetism Ever Measured in RT-1

At last, the highest diamagnetic signals of the RT-1 plasma which has ever measured in RT-1 is mentioned. The diamagnetic signals of the RT-1 plasma tend to be higher with higher ECH power and lower filling gas pressure conditions as mentioned in Chapter 4. The highest diamagnetic signals were obtained with the maximum power of both frequencies of ECH and with as low gas pressure as possible. The magnetic waveforms of the highest diamagnetic signals in RT-1 is shown in Fig. 6.28. This optimized plasma shot was introduced at the last of Chapter 4. The filling H_2 pressure is 0.5 mPa. We put both of the 8.2 GHz microwave and the 2.45 GHz microwave. The power of the 8.2 GHz and the 2.45 GHz microwave are 25 kW and 19.5 kW, respectively.

In Fig. 6.28, the averaged diamagnetic signal reached 4.0 mWb and the diamagnetic signal of loop2 reached 5.0 mWb. At the begining of the ECH heating, the plasma confinement is unstable and then at the middle of the ECH heating the plasma pressure rose up rapidly and after the heating very long decay time of the plasma energy (about 500 ms) was observed. Result of the analysis of the magnetic field structure of the plasma is shown in Fig. 6.29. The pressure profile of the plasma shown in Fig. 6.28 is approximately represented by the pressure profiles of (P, Q) = (3, 2), (4, 3), (6, 4). In these pressure profiles, the pressure peak adii are about 0.62 m and the estimated local beta is about 70%.

In the analysis, the measured magnetic field and numerical field don't fit exactly each other. This is because there're estimate errors which were mentioned in Chapter 5. This is because that the most easiest model was used for simplicity and the pressure profile of the RT-1 plasma is not necessarily expressed by the function $p(\psi) \propto -(\psi_1 - \psi)^P(\psi_2 - \psi)^Q$. Therefore in order to enhance the accuracy of the estimate, we have to improve the pressure model function which is suitable to describe the RT-1 plasma. Additionally in this analysis, because we ignored both of the the plasma anisotropy and the high-beta effect, which usually increase the conversion coefficient of the beta value, there're large possibility that the RT-1 plasma has already higher beta value than unity. The identification of the ultra-high beta

(such as β 1) plasma should be carried over to further researches.

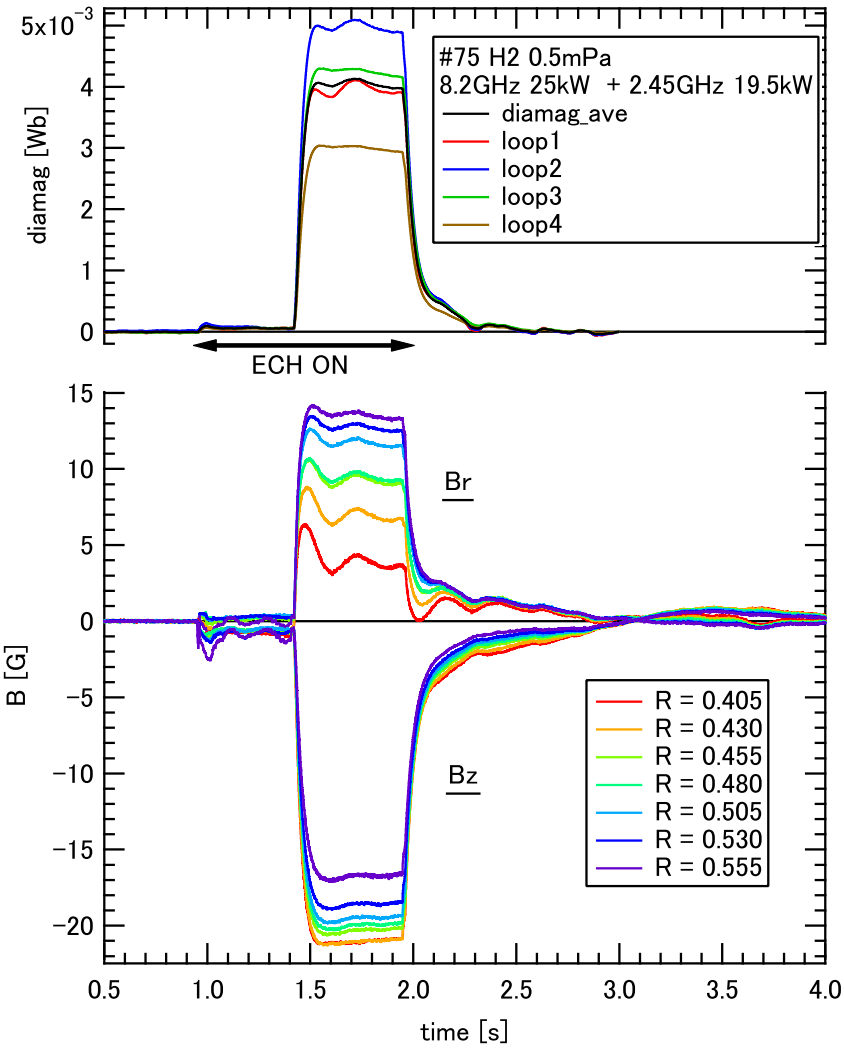

Figure 6.28: The highest diamagnetic signal which has ever observed in RT-1.

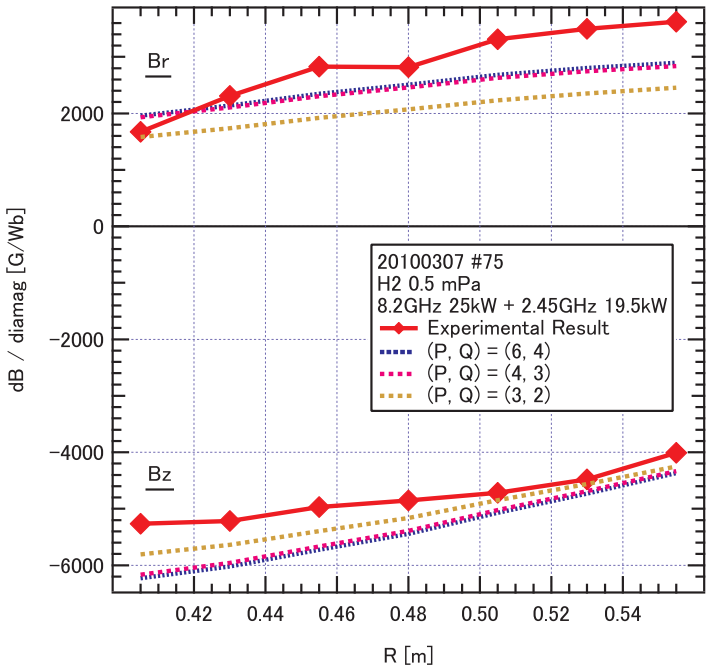

Figure 6.29: The magnetic field structure of Fig. 6.28. Dotted lines shows the calculation results of several pressure profiles.

Chapter 7

Discussion

In this research, we succeeded to confine the high beta plasmas whose local beta exceeds 70% in the magnetospherical plasma device, RT-1. The estimate of the beta value and the evaluation of the energy confinement time was done with several magnetic measurement system which were newly developed in this research.

As a conclusion, this experimental research is briefly summarized first. Secondly, what this research will contribute to a plasma fusion research is given. Finally, the future vision or what is remained as an issue of this research is mentioned.

7.1 Summary of Results

Optimization of the Levitation System

To obtain a high beta plasma in the magnetosphere shaped magnetic configuration, the levitation technique is necessary. In the levitation system like RT-1, the floating coil is easily tilted by the error field and the mass imbalance. Additionally, the tilt secondly causes the rotation motion of the F-coil. Firstly we succeeded to make flatten the floating coil with the correction coil system, which ensure the axially symmetricity of the configuration. Secondly we constructed the larger and further correction coil system to reduce the error field which is secondarily generated by the correction coils. Then we confirmed that the plasma confinement is improved by a factor of few dozens of percent with new correction coils.

High Beta Plasma in RT-1

RT-1's high beta plasma is composed of the hot electrons whose T_e is about 10 keV and density is about order of 10^{16} m^{-3}. Hot electron plasma is likely to be generated in the lower gas fueling conditions, about 1 mPa. When we optimized the discharge conditions in order to obtain the highest diamagnetic signal, the 4.0 mWb of diamagnetic signal was observed and the magnetic field strength measured near the plasma increased significantly. To estimate the local beta of such a large diamagnetic plasma we developed the equilibrium calculation code which is named RTEQ. After the calculations of a variety of pressure profile functions, the minimum conversion coefficient, from the diamagnetic signal to the maximum local beta, is about 120 [1/Wb]. We can therefore say that the maximum local beta value in RT-1 is more than 50%.

Magnetic Field Structure of the RT-1 Plasma

To investigate the structure of the diamagnetic field of RT-1 plasma, we developed the magnetic probe systems which can measure the interior and exterior field of the RT-1 plasma. When we used the probe system to measure the diamagnetic field structure inside of low beta plasma whose diamagnetic signals are about 100 μWb, we found that the pressure profile peaks steeply near the ECH resonance layers.

Next we measured the magnetic field just under the high beta plasma. We found that the plasma pressure profiles are certainly changed depending on the discharge conditions, especially on ECH frequencies. In the case of the plasma whose diamagnetic signal is 4.0 mWb, the pressure peak radius is about 0.62 m and the maximum local beta is estimated more than 70 %.

Evaluation of the Energy Confinement Time

With the magnetic probe system, we succeeded to measure a change of the magnetic field as fast as 1 ms. Focusing on the plasma decay event just after the ECH power is turned off we evaluated the plasma energy confinement time. The longest time of the energy confinement time is more than 200 ms up to 500 ms, which mainly

depends on the filling gas pressure. This long confinement component is thought to be consist of hot electrons confined in the outer region of the floating coil.

7.2 Impacts on Space Physics and Fusion Research

The research which is mentioned in this thesis is conducted on the Ring Trap project. And this research made a contribution to the RT project by optimizing the levitation condition and by analysing the high beta plasma in the RT-1 experiment. As a result, we succeeded to produce and observe the high beta plasma whose beta value is more than 70% in RT-1 as mentioned above. The measured 70% of beta value is much larger than the local beta in tokamaks or stellarators (< 10 %) so that this research has two large significances in the plasma fusion research. One is that we demonstrated to realize the high beta plasma in the laboratory, which was actually observed in Jovian magnetosphere (~ 1). The other is that we proved that an applicability of the magnetospheric plasma to a fusion core, which is proposed by Akira Hasegawa.

It's notoworth that we developed the techniques to realize the magnetosphere in a laboratory on the earth. We do not need to launch a exploration satellite into space. If we want to send a satellite to a planet it takes very long time from launch, for example it takes about 2 years to reach Jupiter. Additionally, the required cost of the satellite obseravation should be incomparably higher than the laborarory experiment on the earth. Thus our development research on RT project offers another choice and another oppotunity to study the physics of magnetosphere. Now in the plasma experiment in RT-1, we forcus on mainly a high beta plasma confinement and a long confinement of a non-neutral plasma. The other scientifical experimental researches will be possible in RT-1. For example, a particle acceleration in magnetosphere (like aurora) or other plasma physiscs in magnetosphere (transport, instabilities, rotating plasma flow, etc.) are attractive physical issues.

Although the magnetospheric plasma has very strong point in confinement of very high beta plasmas, this type of plasma confinment has some difficulties as a reactor. In order to confine a high beta plasma, the magnetic levitation is almost

necessary in this system. Therefore a dipole magnet should be completely removed off from the power source and the refregerator. Additionally the dipole magnet must be shielded from neutrons or heat flux of fusion-burning plasma for a sufficiently long time. These difficulties have prevented the magnetospheric plasma from a fusion plant or reactor design research so far and few people believe that the dipole plasma is suitable for a fusion core at present. In order to realize a dipole fusion reactor in future we, the RT-1 project, have a reponsibility to pursue a research on the magnetospheric plasmas.

We have to specify the beta value of RT-1 with more accuracy first. In this research, the plasma pressure profile and the local beta value in RT-1 are roughly estimated and we confirmed that the beta value is more than 70%. But there may be large estimate error and there's a large possibility that the RT-1 plasma already confines a plasma whose beta value exceeds unity. In order to identify the plasma pressure profile in detail, the pressure profile model function should be improved and anisotropy of the plasma pressure should be investigated. Not only measuring the specific beta value but also achieveing higher beta plasmas will be desired. In this research we have experimented with optimized conditions (with maximum power and lowest neutral gas pressure) and obtained the maximum diamagnetic signal. Therefore we need to develop something new techniques to acheive higher beta plasma such as installing a new heating method (other ECRH, ICRH, NBI, etc.) or driving a fast flow in plasma, which is proposed by Yoshida and Mahajan. Ultimately the critical beta value of the magnetospherical plasma is expected to be revealed. This way, a potential of the dipole fusion will be broadly understood and the design research of the dipole fusion plant will progress gradually. There are many steps to realize a dipole fusion reactor. However, I believe in the distant future that the dipole fusion reactor will be realized by using this research as a stepping toehold.

Acknowledgments

First of all, I must express all of my gratitude to Prof. Zensho Yoshida, the leader of the RT-1 experiment. He was the most indispensable person to finish this research. His continuous suggestions and advices enabeled me to achieve the research, so I express my grateful acknowledgment to Prof. Yoshida. His attitude for scientific researches was very serious and I learned a lot of things from him as a scientist.

I also thank Mr. Junji Morikawa, he has developed the levitation system in RT-1. His advices were very helpful to this research. I enjoyed talking with Mr. Morikawa not only in scientific issues but also in daily conversations. I also appreciate for Dr. Haruhiko Saitoh. Dr. Saitoh worked very hard for the RT-1 experiment and his soft X-ray measurement was very useful in my research. I also thank the member of experimental group in RT-1, Mr. Tatsunori Mizushima, Mr. Masaya Kobayashi and Mr. German Vogel. We spent much time not only in working hard experiments but also in daily living, without their supports the research never be completed.

I also acknowledge Prof. Yuichi Ogawa for his pointed indications. Unfortunately I could not have a frequent conversation with him but his shrewd advice was always helpful.

I also appreciate for the member of theoretical group of the laboratory, Associate Prof. Masaru Furukawa, Mr. Yohei Kawazura, Mr. Kei Tadachi, Mr. Kenji Harima, Shingo Emoto and Tomoaki Sugiura. Prof. Furukawa has developed the equilibrium calculation code for the RT-1 configuration. The code played very large role in my research so his contribution was nessesary to pursue this experimental research. And I also appreciate for the member of the Ogawa laboratory, Mr. Naoki Shinji, Mr. Eiichi Yatsuka. Every time in a banquet party in our laboratory, chatting time with

them has been a very relaxation time for me. Mr. Daisuke Sakata and Mr. Hajime Kato were mey peers from my garaduate students days. Although they graduated after finishing the master course, we enjoyed a lot of joking and studying together when I was a master cource student.

It' also important to remenber to express my thanks to former menbers of the laboratory. I spent much time and shared the difficulties in RT-1 experiment with experimental group members, Mr. Sho Watanabe, Ms. Junko Suzuki and Mr. Hiroyuki Hayashi. I also learned a basic of a thoretical research from Dr. Makoto Hirota, Dr. Dan Hori, Dr. Junya Shiraishi, Mr. Shuhei Numazawa and Ms. Tomoyo Nakatsu.

And I give thanks to our laboratory office administrators Ms. Nami Sugimura and Ms. Takako Kitayama. Their heartily supports in daily life were greate. I also enjoyed talking with Ms. Sugimura about a soccer topic.

I have been financialy supported by the GCOE Office on Nuclear Education and Research Initiative. They gave me the chance to visit the MIT in Cambridge and the American Phisical Society meeting in Atlanta. Therefore I demonstrate my gratitude to GoNERI here.

Finally, I would like to thank my family and friends for their concerns and supports. Especially there're no words to describe my grateful thanks to my parents. My father did his work and financial support for me without any questions and my mother frequentry did cheer me up over the telephone. Their generous affections and disciplined educations in my boyhood were essential component for my research. I can never thank you enough.

Yoshihisa Yano

Bibliography

[1] Z. Yoshida and S. M. Mahajan, "Variational principles and self-organization in two-fluid plasmas", Phys. Rev. Lett. **88**, 095001 (2002).

[2] S. M. Mahajan and Z. Yoshida, "Double curl Beltrami flow: diamagnetic structures", Phys. Rev. Lett. **81**, 4863 (1998).

[3] S. M. Krimigis *et al.*, "Hot plasma environment at Jupiter: Voyager 2 results", Science **206**, 977 (1979).

[4] F. F. Chen, in *Plasma Diagnostic Techniques*, edited by R. H. Huddlestone and S. L. Leonard (Academic, New York, 1956).

[5] Z. Yoshida *et al.*, "First plasma in the RT-1 device", Plasma Fusion Research **1**, 008 (2006).

[6] J. Morikawa *et al.*, "Levitation Experiment Using a High-Temperature Superconductor Coil for a Plasma Confinement Device", J.Appl.Phys. **40**, L1029 (2001).

[7] A. Hajime *et al.*, *Practice of control engineering* in Japanese , (Kyoritsu Syuppan, 1981).

[8] T. Kida *et al.*, *Basic of feedback control* in Japanese, (Baifukan, 2003).

[9] A. Hasegawa *et al.*"A D-^{3} He Fusion Reactor Based on a Dipole Magnetic Field", Nucl. Fus. **30**, 2405 (1990).

[10] J. Kesner *et al.* "Helium Catalyzed D-D Fusion in a Levitated Dipole", Nucl. Fus. **44**, 193 (2004).

[11] J. D. Lawson, "Some Criteria for a Power Producing Thermonuclear Reactor", Proc. Phys. Soc. (London) **B70**, 6 (1957).

[12] J. Morikawa *et al.*, "Plasma Production and Levitation Experiments of a High-temperature Superconductor Coil in a Mini-RT Internal Coil Device", J. Cryo. Soc. Jpn. **39**, 209 (2004).

[13] Y. Ogawa *et al.*, "Construction and Operation of an Internal Coil Device with a High Temperature Superconductor", J. Plasma Fusion Res. **79**, 643 (2003).

[14] H. Saitoh et al., "Confinement of Pure-Electron Plasmas in a Toroidal Magnetic-Surface Configuration ", Phys. Rev. Lett. **92**, 255005 (2004).

[15] J. B. Taylor *et al.*, " Relaxation of Toroidal Plasma and Generation of Reverse Magnetic Fields", Phys. Rev. Lett. **33**, 1139 (1974).

[16] R. J. Goldston and P. H. Rutherford in *Introduction to Plasma Physics*, (Institute of Physics Publishing, London, 1995).

[17] John H. Wolfe *et al.*, "Preliminary Pioneer 10 Encounter Results from the Ames Research Center Plasma Analyzer Experiment ", Science **183**, 303 (1974).

[18] "ITER Physics Basis", Nucl. Fus. **39**, 2137 (1999).

[19] "Progress in the ITER Physics Basis", Nucl. Fus. **47**, S1 (2007).

[20] S. Yoshikawa, "Experiments on plasma confinement in internal-ring devices", Nucl. Fus. **13**, no. 3, pp. 433-449 (1973).

[21] H. S. Bridge *et al.*, "Plasma Observations Near Jupiter: Initial Results from Voyager 1 ", Science **204**, 987 (1979).

[22] J. Shiraishi *et al.*, "Relaxation of a quasisymmetric rotating plasma: A model of Jupiter's magnetosphere", Phys. Plasmas **12**, 092901 (2005).

[23] D.T. Garnier *et al.*, "Design and initial operation of the LDX facility", Fusion Engineering and Design **81**, 2371 (2006).

[24] D.T. Garnier *et al.*, "Confinement improvement with magnetic levitation of a superconducting dipole", Nucl. Fusion **49** 055023 (2009).

[25] I. Karim *et al.*, "Equilibrium Reconstruction of Anisotropic Pressure Profile in the Levitated Dipole Experiment ", J. Fusion Energy **26**, 99 (2007).

[26] John H. Wolfe *et al.*, "Energetic Electrons in the Magnetosphere of Jupiter ", Science **183**, 309 (1974).

[27] Norman F. Ness *et al.*, "Magnetic Field Studies at Jupiter by Voyager 1: Preliminary Results", Science **206**, 982 (1979).

[28] R. E. Vogt *et al.*, "Voyager 2: Energetic Ions and Electrons in the Jovian Magnetosphere", Science **206**, 984 (1979).

[29] A. C. Boxer *et al.*, "Turbulent inward pinch of plasma confined by a levitated dipole magnet", Nature Physics **6**, 207 (2010).

[30] T. Mito *et al.*, "Engineering Design of the Mini-RT Device", IEEE Trans. Appl. Supercond. **13**, 1500 (2003).

[31] N. Yanagi *et al.*, "Experiments of the HTS Floating Coil System in the Mini-RT Project", IEEE Trans. Appl. Supercond. **14**, 1539 (2004).

[32] N. Yanagi *et al.*, "Engineering Research and Developement of Magnetically Levitated High-Temprature Superconducting Coil System for Mini-RT Project", IEEE Trans. Appl. Supercond. **12**, 948 (2002).

[33] N. Yanagi *et al.*, "Excitation Test Results of the HTS Floating Coil for the Mini-RT Project", IEEE Trans. Appl. Supercond. **13**, 1504 (2003).

[34] E. E. Ortiz *et al.*, "Effects of the Hot Electron Interchange Instability on Plasma Confined in a Dipolar Magnetic Field", J. Fusion Energy **26**, 139 (2007).

[35] E. J. Smith *et al.*, "Ulysses at Jupiter: An Overview of the Encounter", Science **257**, 1503 (1992).

[36] A. Balogh *et al.*, "Magnetic Field Observations During the Ulysses Flyby of Jupiter", Science **257**, 1515 (1992).

[37] L. J. Lanzerotti *et al.*, "The Hot Plasma Environment at Jupiter: Ulysses Results", Science **257**, 1518 (1992).

[38] Samuel J. Bame *et al.*, "Jupiter's Magnetosphere: Plasma Description from the Ulysses Flyby", Science **257**, 1539 (1992).

[39] T. Gold, "Motions in the Magnetosphere of the Earth", J. Geophys. Res. **64**, 1219 (1959).

[40] Stirling A. Colgate and Harold P. Furth, "Stabilization of Pinch Discharge", Phys. Fluids **3**, 982 (1960).

[41] M. N.Rosenbluth and C. L. Longmire, "Stability of Plasmas Confined by magnetic Field", Annals of Physics **1**, 120 (1957).

[42] T. Ohkawa and D. W. Kerst, "Sable Plasma Confinement By Multipole Fields", Phys. Letters **7**, 41 (1961).

[43] S. Yoshikawa and U. R. Christensen, "Axisymmetric Minimum Average B Configuration of a Triply Connected System", Phys. Fluids **9**, 2295 (1966).

[44] J. File *et al.*, "Princeton Floating Multipole-Superconducting Ring Progress", J.Appl.Phys. **40**, 2106 (1969).

[45] V. Kelvin Neil and R. K. Cooper, "Stability of a Current Ring Supported in a Magnetic Field", Rev. Sci. Instrum. **41**, 295 (1969).

[46] C. H. Woods *et al.*, "Stability Analysis of a Levitated Superconducting Current Ring Stabilized by Feedback and Eddy Currents", J. Appl. Phys. **40**, 3295 (1970).

[47] J. File *et al.*, "Operation of a Levitated Superconducting Ring in a Plasma Physics Experimental Device", J. Appl. Phys. **42**, 6 (1971).

[48] V. P. Pastukhov and N. V. Chudin, "Plasma Convection near the Threshold for MHD Instability in Nonparaxial Magnetic Confinement Systems", Plasma Physics Reports **27**, 907 (2001).

[49] H. Saitoh *et al.*, "Potential structure of a plasma in an internal conductor device under the influence of a biased electrode", Phys. Plasmas **11**, 3331 (2004).

[50] K. Lackner, "Computation of Ideal MHD Equilibria", Comput. Phys. Comm. **12**, 33 (1976).

[51] H. Grad, "Toroidal Containment of a Plasma", Phys. Fluids **10**, 137 (1967).

[52] G. O. Spies and D. B. Nelson, "Properties of magnetically confined plasma equilibria", Phys. Fluids **17**, 1879 (1974).

[53] D.T. Garnier *et al.*, "Stabilization of a low-frequency instability in a dipole plasma", J. Plasma Phys. **74**, 733 (2008).

[54] D.T. Garnier *et al.*, "Magnetohydrodynamic stability in a levitated dipole", Phys. Plasmas **6**, 3431 (1999).

[55] J. Sinnis *et al.*, "Particle Loss in the Levitated Spherator FM-1", Phys. Rev. Lett. **29**, 1214 (1972).

[56] R. Freeman *et al.*, "Confinement Properties of the Levitated Spherator", Phys. Rev. Lett. **26**, 356 (1971).

[57] D.T. Garnier *et al.*, "Production and study of high-beta plasma confined by a superconducting dipole magnet", Phys. Plasmas **13**, 056111 (2006).

[58] J. Kesner, "Convective cell formation in a Z-pinch", Phys. Plasmas **10**, 908 (2003).

[59] J. Kesner and D.T. Garnier, "Convective cell formation in a levitated dipole", Phys. Plasmas **7**, 2733 (2000).

[60] Z. Yoshida *et al.*, "Beltrami fields in plasmas: High-confinement mode boundary layers and high beta equilibria", Phys. Plasmas **8**, 2125 (2001).

[61] Z. Yoshida *et al.*, "High-β (Hot Electron) Plasma in Ring Trap 1 (RT-1)", In *22nd IAEA Fusion Energy Conference*, EX/P5-28 (2008).

[62] I. H. Hutchinson, *Plasma Diagnostic Techniques*, (Campridge University Press, 1987).

[63] E. Yatsuka *et al.*, "Radio-frequency electromagnetic field measurements for direct detection of electron Bernstein waves in a torus plasma", Rev. Sci. Instrum. **80**, 023505 (2009).

[64] E. Yatsuka *et al.*, "Direct Measurement of a Mode-Converted Electron Bernstein Wave in the Internal Coil Device Mini-RT", Plasma Fus. Res. **3**, 013 (2008).

[65] E. Yatsuka *et al.*, "Electron Bernstein Wave Heating on the Internal Coil Device Mini-RT ", Fus. Sci. Tech. **51**, 310 (2007).

[66] H. Saitoh *et al.*, "Long-Lived Pure Electron Plasma in Ring Trap-1", Plasma Fus. Res. **2**, 045 (2007).

[67] Y. Ogawa *et al.*, "Construction and Operation of an Internal Coil Device, RT-1, with a High-Temperature Superconductor ", Plasma Fus. Res. **4**, 020 (2009).

[68] Y. Yano *et al.*, "Improvement of Field Accuracy and Plasma Performance in the RT-1 Device", Plasma Fus. Res. **4**, 039 (2009).

[69] H. Saitoh *et al.*, "Initial Results of X-ray Imaging and Energy Spectrum Measurements of Hot Electron Plasmas in RT-1", Plasma Fus. Res. **4**, 050 (2009).

[70] H. Saitoh *et al.*, "Measurement of the Density Profile of a Toroidal Non-neutral Plasma with a Wall-Probe Array", Plasma Fus. Res. **4**, 054 (2009).

[71] Y. Ogawa *et al.*, "Application of high-temperature superconducting coil for internal ring devices", Fus. Eng. Design **81**, 2361 (2006).

[72] J. Morikawa *et al.*, "Development of a super-conducting levitated coil system in the RT-1 magnetospheric confinement device", Fus. Eng. Design **82**, 1437 (2007).

[73] Y. Yano *et al.*, "Feedback control of the position of the levitated superconducting magnet in the RT-1 device " will be published in Fus. Eng. Design **85**, (2010) doi:10.1016/j.fusengdes.2010.02.029.

[74] T. Taizo *et al.*, "Development of Persistent-Current Mode HTS Coil for the RT-1 Plasma Device", IEEE Trans. Appl. Supercond. **16**, 910 (2006).

[75] S. Mizumaki *et al.*, "Development of the Magnetically Floating Superconducting Dipole in the RT-1 Plasma Device", IEEE Trans. Appl. Supercond. **16**, 918 (2006).

[76] T. Taizo *et al.*, "First Experiment on Levitation and Plasma With HTS Magnet in the RT-1 Plasma Device", IEEE Trans. Appl. Supercond. **17**, 1402 (2007).

Publication

Refereed Articles

Improvement of Field Accuracy and Plasma Performance in the RT-1 Device.,
Yoshihisa YANO, Zensho YOSHIDA, Junji MORIKAWA, Haruhiko SAITOH, Hiroyuki HAYASHI and Tatsunori MIZUSHIMA, Plasma Fus. Res. **4**, 039 (2009).

Feedback control of the position of the levitated superconducting magnet in the RT-1 device.,
Yoshihisa YANO, Zensho YOSHIDA, Yuichi OGAWA, Junji MORIKAWA and Haruhiko SAITOH, will be published in Fus. Eng. Design **85**, (2010) doi:10.1016/j.fusengdes.2010.02.029.

Presentation at American Physics Society [International]

Direct measurements of the magnetic field inside the magnetospheric plasma RT-1.
YOSHIHISA YANO, ZENSHO YOSHIDA, JUNJI MORIKAWA, HARUHIKO SAITOH, TATSUNORI MIZUSHIMA,
American Physical Society, 51st Annual Meeting of the APS Division of Plasma Physics, November 2-6, 2009, abstract XP8.047, at Atlanta, Georgia

Presentations at JPS [Domestic]

- **RT- 1 超伝導コイルの浮上制御**
  矢野善久，渡邉 将, 吉田 善章, 森川 淳二
  2006 年年次大会（愛媛大/松山大） 29pUD- 6.
  Magnetic Levitation Conrol of RT-1 Super-conducting Coil
  Y. Yano, S. Watanabe, Z. Yoshida, J. Morikawa
  2006 Annual meeting in Ehime/Matsuyama Univ. 29pUD- 6.

- **RT- 1 実験装置における磁気浮上システムの現状**
  矢野善久，渡邉将，吉田善章，森川惇二，齋藤晴彦，鈴木順子
  2006 年秋季大会（千葉大） 24pQA- 3.
  Present State of Magnetic Levitation Systems of RT-1 device
  Y. Yano, S. Watanabe, Z. Yoshida, J. Morikawa, H. Saito, J. Suzuki
  2006 Autumn meeting in Chiba univ. 24pQA- 3.

- **RT-1 超伝導浮上コイルにおける磁気浮上制御とバランス補正**
  矢野善久，渡邉将，吉田善章，森川惇二，齋藤晴彦，鈴木順子
  2007 年春季大会（鹿児島大） 19aQA-7.
  Magnetic levitation control and balance correction of RT-1 HTS-coil
  Y. Yano, S. Watanabe, Z. Yoshida, J. Morikawa, H. Saito, J. Suzuki
  2007 Apring meeting in Kagoshima Univ. 19aQA-7.

- **RT-1 プラズマの高性能化にともなう反磁性計測と新たな平衡計算モデルについて**
  矢野善久，渡邉将，吉田善章，森川惇二，齋藤晴彦，鈴木順子
  2008 年年次大会（近大） 26aQF-5.
  Diamagnetic Measurement and New Equilibrium Model with an Improvement of RT-1 plasma
  Y. Yano, S. Watanabe, Z. Yoshida, J. Morikawa, H. Saito, J. Suzuki
  2008 Annual meeting in Kinki Univ. 26aQF-5.

- **RT-1 磁気圏型プラズマの磁気計測と MHD 平衡の実験的解析**
  矢野善久，渡邉将，林裕之, 吉田善章, 森川惇二, 齋藤晴彦, 水島龍徳
  2008 年秋季大会（岩手大） 21pZH-11.
  Magnetic measurements and experimental analysis of MHD equilibrium in the RT-1 device
  Y. Yano, S. Watanabe, H. Hayashi, Z. Yoshida, J. Morikawa, H. Saito, T. Mizushima
  2008 Autumn meeting in Iwate Univ. 21pZH-11.

- **磁気圏型プラズマ装置 RT-1 における高 β 平衡の磁気計測**
  矢野善久，渡邉将, 林裕之, 吉田善章, 森川惇二, 齋藤晴彦, 水島龍徳
  2009 年年次大会（立教大） 28aXE-2.
  Magnetic measurements of high-β equilibrium in the RT-1 magnetosphere shaped plasma device
  Y. Yano, S. Watanabe, H. Hayashi, Z. Yoshida, J. Morikawa, H. Saito, T. Mizushima
  2009 Annual meeting in Rikkyo Univ. 28aXE-2.

- **磁気計測を中心とした磁気圏型プラズマ RT-1 の閉じ込め特性解析**
  矢野善久，吉田善章, 森川惇二, 齋藤晴彦, 水島龍徳, 小林真也
  2009 年秋季大会（熊本大） 26aYP-6 .
  Analysis of confinement characteristics of the magnetospheric plasma device RT-1 with magnetic measurements
  Y. Yano, Z. Yoshida, J. Morikawa, H. Saito, T. Mizushima, M. Kobayashi
  2009 Winter meeting in Kumamoto Univ. 26aYP-6 .

- **磁気圏型プラズマにおける加熱停止後に見られる崩壊現象**
  矢野善久，吉田善章，森川惇二，齋藤晴彦，水島龍徳，小林真也
  2010 年年次大会（岡山大） 21aTE-3 .
  Collapse phenomenon after the ECRH is stopped in a magnetospheric plasma
  Y. Yano, Z. Yoshida, J. Morikawa, H. Saitoh, T. Mizushima, M. Kobayashi

2010 Annual meeting in Okayama Univ. 21aTE-3 .

Presentation at JSPF [Domestic]

RT-1 超伝導コイル浮上制御システムの安定性解析および最適化

矢野善久, 渡邉将, 吉田善章, 森川惇二, 齋藤晴彦, 鈴木順子

2007 年会 29pA01P.

Stability analysis and optimization of levitation control system of superconducting coil in RT-1

Y. Yano, S. Watanabe, Z. Yoshida, J. Morikawa, H. Saito, J. Suzuki

2007 Annual meeting 29pA01P.